

HIGH PRESSURE AND HIGH STRAIN RATE BEHAVIOR OF  
CEMENTITIOUS MATERIALS: EXPERIMENTS AND  
ELASTIC/VISCOPLASTIC MODELING

By

MARTIN J. SCHMIDT

A DISSERTATION PRESENTED TO THE GRADUATE SCHOOL  
OF THE UNIVERSITY OF FLORIDA IN PARTIAL FULFILLMENT  
OF THE REQUIREMENTS FOR THE DEGREE OF  
DOCTOR OF PHILOSOPHY

UNIVERSITY OF FLORIDA

2003

Copyright 2003

by

Martin J. Schmidt

I would like to dedicate this work to my parents, who never lost faith in me throughout what turned out to be a much longer process than anyone ever imagined.

## ACKNOWLEDGMENTS

The author thanks each member of His supervisory committee for their suggestions and support. Special appreciation is extended to Dr. Cristescu and Dr. Cazacu for their enthusiasm and support throughout the course of this study. Dr. C. A. Ross served as the author's original advisor and was invaluable in the dynamic experimental portion of this program. The author also wishes to thank Mr. Mark Green, formerly of the U.S. Army Corps of Engineer Waterways Experiment station for his efforts in the quasi-static experiments.

The author sincerely appreciates the support provided by the management of the Air Force Research Laboratory Munitions Directorate for providing the opportunity to pursue this study and the necessary time for completing this effort.

Finally, the author also wishes to thank his many friends and colleagues who offered encouragement over the several years this effort has taken.



## TABLE OF CONTENTS

	<u>page</u>
ACKNOWLEDGMENTS . . . . .	iv
LIST OF TABLES . . . . .	vii
LIST OF FIGURES . . . . .	viii
ABSTRACT . . . . .	xv
 CHAPTER	
1 INTRODUCTION . . . . .	1
2 EXPERIMENTAL INVESTIGATION OF THE QUASI-STATIC BE- HAVIOR . . . . .	4
2.1 Background and Overview of Testing Devices and Quasi-Static Experimental Techniques . . . . .	4
2.2 Material Description . . . . .	7
2.2.1 Historical Note . . . . .	7
2.2.2 Material Studied, WES5000 . . . . .	9
2.3 Experimental Design . . . . .	10
2.4 Unconfined Compression . . . . .	17
2.5 300 MPa Experiment . . . . .	21
2.6 450 MPa Experiment . . . . .	26
2.7 150 MPa Experiment . . . . .	30
2.8 500 MPa Hydrostatic Compression Experiment . . . . .	34
2.9 50 MPa Experiment . . . . .	37
2.10 200 MPa Experiment . . . . .	41
2.11 300 MPa Experiment (Second) . . . . .	45
2.12 100 MPa Experiment . . . . .	49
2.13 375 MPa Experiment . . . . .	52
2.14 Elastic Parameter Evaluation . . . . .	56
2.15 General Comments . . . . .	57
3 DYNAMIC MATERIAL CHARACTERIZATION . . . . .	61
3.1 Dynamic Characterization Techniques . . . . .	61
3.1.1 The Hopkinson Bar . . . . .	61
3.1.2 Compressive Split Hopkinson Pressure Bar Testing . . . . .	62
3.1.3 Dynamic Tensile Testing . . . . .	69

3.1.4	Confined Dynamic Testing . . . . .	72
3.1.5	Plate Impact Experiments . . . . .	73
3.2	Dynamic Experimental Program . . . . .	74
3.3	Experimental Setup . . . . .	75
3.3.1	SHPB . . . . .	75
3.3.2	Quasi-Static Setup . . . . .	81
3.3.3	Specimen Design/Preparation . . . . .	81
3.3.4	Experimental Protocol . . . . .	84
3.4	Experimental Results . . . . .	89
3.4.1	Quasi-Static Baseline . . . . .	89
3.4.2	SHPB Results . . . . .	101
4	CONSTITUTIVE MODELING . . . . .	127
4.1	Introduction . . . . .	127
4.2	Concrete Constitutive Modeling Review . . . . .	127
4.2.1	Introductory Note . . . . .	127
4.2.2	Micromechanical Modeling . . . . .	128
4.2.3	Macromechanical Models . . . . .	130
4.3	Elastic-Viscoplastic Model Development . . . . .	140
4.4	Elastic Parameter Evaluation . . . . .	142
4.5	Yield Function Evaluation . . . . .	145
4.6	Strain Rate Orientation Tensor . . . . .	153
4.7	Comparison of Theoretical to Experimental Results . . . . .	178
5	CONCLUSIONS . . . . .	185
	REFERENCES . . . . .	188
	BIOGRAPHICAL SKETCH . . . . .	196

# LIST OF TABLES

<u>Table</u>	<u>page</u>
1-1 Strain rate response as a function of impact velocity . . . . .	2
2-1 Ingredients and mixture proportions for WES5000 concrete. . . . .	9
2-2 Properties at 28 days for WES5000 concrete. . . . .	10
2-3 Waterways Experiment Station experimental matrix . . . . .	15
3-1 Dynamic Kármán test matrix . . . . .	75
3-2 Ingredients and mixture proportions for mortar . . . . .	83
3-3 Quasi-static mortar results . . . . .	91
3-4 Average peak principal stress difference at failure for mortar. . . . .	94
3-5 Quasi-static WES5000 results . . . . .	96
3-6 Average peak principal stress difference at failure for WES5000 . . . . .	97
3-7 Mortar SHPB test conditions . . . . .	102
3-8 Mortar SHPB results . . . . .	104
3-9 Test conditions for WES5000 SHPB experiments . . . . .	116
3-10 Results for WES5000 SHPB experiments . . . . .	117
4-1 Parameter values for $H_D$ . . . . .	152

## LIST OF FIGURES

<u>Figure</u>	<u>page</u>
2-1 Dynamic aspects of mechanical testing . . . . .	6
2-2 Section through triaxial Kármán device . . . . .	7
2-3 Stress-strain curve for concrete uniaxial compression test . . . . .	11
2-4 Monotonic hydrostatic compression test exhibiting hysteretic behavior	13
2-5 Schematic of hydrostatic creep experiment . . . . .	14
2-6 Schematic of deviatoric shear creep experiment . . . . .	16
2-7 Sample prepared for testing . . . . .	18
2-8 Waterways Experiment Station Secodyne 500K pound load frame . .	19
2-9 Unconfined compression test . . . . .	20
2-10 Hydrostatic compression phase, 300 MPa Kármán experiment . . . .	23
2-11 Hydrostatic compression phase (low pressure range), 300 MPa Kármán experiment . . . . .	23
2-12 Deviatoric phase of 300 MPa Kármán experiment, axial strain . . . .	24
2-13 Deviatoric phase of 300 MPa Kármán experiment, radial strain . . . .	24
2-14 Deviatoric phase of 300 MPa Kármán experiment, radial strain (low PSD range) . . . . .	25
2-15 Deviatoric phase of 300 MPa Kármán experiment, all strains . . . . .	25
2-16 Hydrostatic compression phase, 450 MPa Kármán experiment . . . .	27
2-17 Hydrostatic compression phase (low pressure range), 450 MPa Kármán experiment . . . . .	27
2-18 Deviatoric phase of 450 MPa Kármán experiment, axial strain . . . .	28
2-19 Deviatoric phase of 450 MPa Kármán experiment, radial strain . . . .	28
2-20 Deviatoric phase of 450 MPa Kármán experiment, radial strain (low PSD range) . . . . .	29

2-21 Deviatoric phase of 450 MPa Kármán experiment, all strains . . . . .	29
2-22 Hydrostatic compression phase, 150 MPa Kármán experiment . . . . .	31
2-23 Hydrostatic compression phase, 150 MPa Kármán experiment, first 2 cycles . . . . .	31
2-24 Deviatoric phase of 150 MPa Kármán experiment, axial strain . . . . .	32
2-25 Deviatoric phase of 150 MPa Kármán experiment, radial strain . . . . .	32
2-26 Deviatoric phase of 150 MPa Kármán experiment, radial strain (low PSD range) . . . . .	33
2-27 Deviatoric phase of 150 MPa Kármán experiment, all strains . . . . .	33
2-28 Hydrostatic compression Kármán experiment to 500 MPa . . . . .	35
2-29 Hydrostatic compression Kármán experiment to 500 MPa, first 2 cycles	36
2-30 Volume strain rate vs. time for 500 MPa hydrostatic compression ex- periment . . . . .	36
2-31 Hydrostatic compression phase, 50 MPa Kármán experiment . . . . .	38
2-32 Deviatoric phase of 50 MPa Kármán experiment, axial strain . . . . .	39
2-33 Deviatoric phase of 50 MPa Kármán experiment, radial strain . . . . .	39
2-34 Deviatoric phase of 50 MPa Kármán experiment, radial strain first 2 cycles . . . . .	40
2-35 Deviatoric phase of 50 MPa Kármán experiment, all strains . . . . .	40
2-36 Hydrostatic compression phase, 200 MPa Kármán experiment . . . . .	42
2-37 Deviatoric phase of 200 MPa Kármán experiment, axial strain . . . . .	43
2-38 Deviatoric phase of 200 MPa Kármán experiment, radial strain . . . . .	43
2-39 Deviatoric phase of 200 MPa Kármán experiment, radial strain first 2 cycles . . . . .	44
2-40 Deviatoric phase of 200 MPa Kármán experiment, all strains . . . . .	44
2-41 Hydrostatic compression phase, 300 MPa Kármán experiment . . . . .	46
2-42 Deviatoric phase of 300 MPa Kármán experiment, axial strain . . . . .	47
2-43 Deviatoric phase of 300 MPa Kármán experiment, radial strain . . . . .	47

2-44 Deviatoric phase of 300 MPa Kármán experiment, radial strain first 2 cycles . . . . .	48
2-45 Deviatoric phase of 300 MPa Kármán experiment, all strains . . . . .	48
2-46 Hydrostatic compression phase, 100 MPa Kármán experiment . . . . .	50
2-47 Deviatoric phase of 100 MPa Kármán experiment, axial strain . . . . .	50
2-48 Deviatoric phase of 100 MPa Kármán experiment, radial strain . . . . .	51
2-49 Deviatoric phase of 100 MPa Kármán experiment, radial strain first 2 cycles . . . . .	51
2-50 Deviatoric phase of 100 MPa Kármán experiment, all strains . . . . .	52
2-51 Hydrostatic compression phase, 375 MPa Kármán experiment . . . . .	53
2-52 Deviatoric phase of 375 MPa Kármán experiment, axial strain . . . . .	54
2-53 Deviatoric phase of 375 MPa Kármán experiment, radial strain . . . . .	54
2-54 Deviatoric phase of 375 MPa Kármán experiment, radial strain first 2 cycles . . . . .	55
2-55 Deviatoric phase of 375 MPa Kármán experiment, all strains . . . . .	55
2-56 Least squares analysis for determination of Young's modulus . . . . .	57
2-57 Young's modulus (E) as a function of mean normal stress, experi- mental data . . . . .	58
2-58 Bulk modulus (K) as a function of mean normal stress, experimental data . . . . .	59
2-59 Peak principal stress difference as a function of radial confinement . . . . .	60
3-1 Split Hopkinson pressure bar . . . . .	63
3-2 Elastic impact of two circular bars . . . . .	64
3-3 Split Hopkinson pressure bar expanded view . . . . .	66
3-4 Brazilian test . . . . .	71
3-5 Stresses and stress distribution for the Brazilian test . . . . .	71
3-6 Hydrostatic confinement cell . . . . .	73
3-7 University of Florida GERC SHPB . . . . .	76
3-8 Cut away view of GERC confinement cell (all dimensions in inches) . . . . .	77

3-9 Hydraulic load cell for SHPB . . . . .	78
3-10 End restraint for SHPB . . . . .	78
3-11 Bar stop for SHPB . . . . .	79
3-12 End restraint with stop in place for SHPB . . . . .	80
3-13 Load frame modified for confined test . . . . .	82
3-14 Strain gauges applied to WES5000 SHPB specimen . . . . .	84
3-15 Mortar SHPB specimen with strain gauges applied . . . . .	85
3-16 Setup: cell in place on SHPB . . . . .	86
3-17 Setup: specimen in place and secured . . . . .	87
3-18 Setup: electrical leads connected . . . . .	88
3-19 Setup: latex membrane in place and secured . . . . .	89
3-20 Setup: confinement cell in position over specimen . . . . .	90
3-21 Setup: accumulator and end caps connected . . . . .	90
3-22 Quasi-static mortar unconfined compression experiment - QSMU01 . . . . .	92
3-23 Quasi-static mortar confined (QSMC05) - 1.72 MPa confinement . . . . .	93
3-24 Quasi-static mortar confined (QSMC04) - 3.45 MPa confinement . . . . .	93
3-25 Quasi-static mortar confined (QSMC07) - 6.89 MPa confinement . . . . .	94
3-26 Confinement effect on quasi-static mortar behavior . . . . .	94
3-27 Peak principal stress difference at failure as a function of confinement for mortar . . . . .	95
3-28 Quasi-static concrete unconfined (QSCU01) . . . . .	98
3-29 Quasi-static concrete confined (QSCC11) - 1.72 MPa confinement . . . . .	98
3-30 Quasi-static concrete confined (QSCC04) - 3.45 MPa confinement . . . . .	99
3-31 Quasi-static concrete confined (QSCC06) - 6.89 MPa confinement . . . . .	99
3-32 Confinement effect on quasi-static WES5000 behavior . . . . .	100
3-33 Peak principal stress difference at failure as a function of confinement for WES5000 . . . . .	100
3-34 Damage state A - DCMC14 . . . . .	105

3-35 Damage state B - DCMC27 . . . . .	105
3-36 Damage state D - DCMU07 . . . . .	107
3-37 Direct compression mortar unconfined (DCMU04) - $L_v$ condition . . .	107
3-38 Unconfined mortar response at three different strain rates . . . . .	109
3-39 Direct compression mortar confined (DCMC36) - $L_v$ , $L_p$ condition . .	109
3-40 Direct compression mortar confined (DCMC32) - $M_v$ , $L_p$ condition . .	110
3-41 Direct compression mortar confined (DCMC28) - $H_v$ , $L_p$ condition . .	110
3-42 Direct compression mortar confined (DCMC15) - $L_v$ , $M_p$ condition . .	111
3-43 Direct compression mortar confined (DCMC20) - $M_v$ , $M_p$ condition . .	111
3-44 Direct compression mortar confined (DCMC18) - $H_v$ , $M_p$ condition . .	112
3-45 Direct compression mortar confined (DCMC29) - $L_v$ , $H_p$ condition . .	113
3-46 Direct compression mortar confined (DCMC35) - $M_v$ , $H_p$ condition . .	113
3-47 Direct compression mortar confined (DCMC26) - $H_v$ , $H_p$ condition . .	114
3-48 Effect of confinement on mortar DIF . . . . .	114
3-49 Damage state A - WES5000 . . . . .	118
3-50 Damage state B - WES5000 . . . . .	118
3-51 Damage state C - WES5000 . . . . .	119
3-52 Damage state D - WES5000 . . . . .	119
3-53 Direct compression concrete unconfined (DCCU03) - $L_v$ condition . .	121
3-54 Direct compression concrete confined (DCCC11) - $L_v$ , $L_p$ condition . .	121
3-55 Direct compression concrete confined (DCCC13) - $M_v$ , $L_p$ condition . .	122
3-56 Direct compression concrete confined (DCCC10) - $H_v$ , $L_p$ condition . .	122
3-57 Direct compression concrete confined (DCCC02) - $L_v$ , $M_p$ condition . .	123
3-58 Direct compression concrete confined (DCCC04) - $M_v$ , $M_p$ condition . .	123
3-59 Direct compression concrete confined (DCCC15) - $H_v$ , $M_p$ condition . .	124
3-60 Direct compression concrete confined (DCCC18) - $L_v$ , $H_p$ condition . .	125
3-61 Direct compression concrete confined (DCCC21) - $M_v$ , $H_p$ condition . .	125



3-62 Direct compression concrete confined (DCCC17) - $H_v$ , $H_p$ condition . . . . .	126
3-63 Effect of confinement on WES5000 DIF . . . . .	126
4-1 Mohr-Coulomb yield criterion . . . . .	134
4-2 Dilatancy associated with yield surface open in positive direction . . . . .	135
4-3 Modified Drucker/Prager cap model . . . . .	136
4-4 Holmquist-Johnson-Cook Model . . . . .	137
4-5 Young's modulus ( $E$ ) as a function of mean normal stress . . . . .	144
4-6 Bulk modulus ( $K$ ) as a function of mean normal stress . . . . .	145
4-7 Stabilization boundary . . . . .	146
4-8 Irreversible hydrostatic work . . . . .	148
4-9 Hydrostatic yield function . . . . .	150
4-10 Deviatoric yield function . . . . .	151
4-11 Deviatoric yield function compared to 200 MPa experiment . . . . .	153
4-12 Strain rate orientation tensor - kN1 hydro . . . . .	157
4-13 Irreversible volumetric strain rate . . . . .	158
4-14 Comparison of data to model for kN1 hydro . . . . .	159
4-15 Strain rate orientation tensor - kN1 deviatoric, 200 MPa experiment . . . . .	160
4-16 Strain rate orientation tensor - kN2, 200 MPa experiment . . . . .	161
4-17 Time adjusted loading profile . . . . .	162
4-18 Adjusted axial strain results - 375 MPa experiment . . . . .	163
4-19 Strain rate orientation tensor - kN1, 375 MPa experiment . . . . .	164
4-20 Strain rate orientation tensor - kN2, 375 MPa experiment . . . . .	165
4-21 Comparison of analytical to experimental results - kN1, 375 MPa experiment . . . . .	166
4-22 Comparison of analytical to experimental results - kN2, 375 MPa experiment . . . . .	167
4-23 Strain rate orientation tensor - $\psi$ . . . . .	168
4-24 Strain rate orientation tensor - $\psi$ , unconfined experiment . . . . .	169

4-25 Strain rate orientation tensor - $\psi$ , unconfined experiment low PSD range . . . . .	170
4-26 Peak $\psi$ value as a function of $\chi$ . . . . .	171
4-27 Principal stress difference at peak $\psi$ as a function of $\chi$ . . . . .	172
4-28 Compressibility - dilatancy boundary . . . . .	173
4-29 Theoretical $\psi$ compared to unconfined experimental data, compressive domain . . . . .	174
4-30 Theoretical $\psi$ compared to unconfined experimental data . . . . .	175
4-31 Theoretical $\psi$ compared to 375 MPa experimental data . . . . .	176
4-32 Strain rate orientation tensor - $kN_2$ . . . . .	177
4-33 Strain rate orientation tensor - $kN_2$ , low PSD range . . . . .	178
4-34 Parameter $\xi_0$ as a function of $\chi$ . . . . .	179
4-35 Parameters $\xi_0$ and $\xi_0^{(1)}$ as a function of $\chi$ . . . . .	179
4-36 Parameters $\xi_0$ and $\xi_0^{(2)}$ as a function of $\chi$ . . . . .	180
4-37 Theoretical $\xi_0$ compared to experimental data . . . . .	180
4-38 Parameters $\xi_1$ and $\xi_2$ , comparison of experimental and theoretical results . . . . .	181
4-39 Experimental/theoretical comparison of $kN_2$ , $\chi = 0$ MPa . . . . .	181
4-40 Experimental/theoretical comparison of $kN_2$ , $\chi = 150$ MPa . . . . .	182
4-41 Experimental/theoretical comparison of $kN_2$ , $\chi = 375$ MPa . . . . .	182
4-42 Experimental/theoretical comparison of uniaxial compression test . . . . .	183
4-43 Experimental/theoretical comparison of 375 MPa hydrostatic compression test . . . . .	183
4-44 Experimental/theoretical comparison of 375 MPa deviatoric compression test . . . . .	184

Abstract of Dissertation Presented to the Graduate School  
of the University of Florida in Partial Fulfillment of the  
Requirements for the Degree of Doctor of Philosophy

HIGH PRESSURE AND HIGH STRAIN RATE BEHAVIOR OF  
CEMENTITIOUS MATERIALS: EXPERIMENTS AND  
ELASTIC/VISCOPLASTIC MODELING

By

Martin J. Schmidt

August 2003

Chair: Nicolaie D. Cristescu

Cochair: Oana Cazacu

Major Department: Mechanical and Aerospace Engineering

The goal of this dissertation was to experimentally investigate the high rate and high pressure mechanical response of a mortar and concrete mix and use or develop a constitutive model able to describe the observed behavior. Triaxial compression tests at a strain rate of  $10^{-6}$ /s, and for confining pressures ranging from 0 to 0.5 GPa were conducted. Dynamic tests in the range 60/s to about 160/s under both unconfined and confined conditions were conducted using the University of Florida's 7.62 cm diameter split Hopkinson pressure bar (SHPB). The data obtained in such tests allowed the quantification of the combined effects of confining pressure and strain rate on the deformation and strength of the materials. For mortar, dilatancy has been observed at high levels of the principal stress difference for both dynamic and quasi-static conditions. The unconfined dynamic compressive strengths are approximately double those of the quasi-static compressive strengths. Most of the confined SHPB mortar specimens showed very little damage post-test other than some chipping around the top edges, most likely due to localized tensile effects.

For the concrete selected for this research, WES5000, quasi-static hydrostatic tests conducted up to a pressure of 0.5 GPa allowed for the accurate determination of the dependence of the bulk modulus on pressure and the correct estimation of the material's compaction properties when subjected to pressures in the range encountered in dynamic events. For confined quasi-static conditions, the material exhibited hardening behavior up to failure. Both compressibility and dilatancy regimes of the volumetric behavior were observed, the dilatancy threshold being highly dependent on the level of confinement. The unconfined dynamic strength is as high as 1.5 times the quasi-static strength, the material generally exhibiting far more cracking under similar loading conditions than was observed in mortar. The confined dynamic tests showed similar stress-strain response as the quasi-static tests conducted at the same level of confinement. A decrease in strain rate sensitivity with increasing confining pressure was observed.

A new elastic/viscoplastic model that captures compressibility and dilatancy, as well as strain rate effects has been developed for concrete. As a general framework, the elastic-viscoplastic formulation of Cristescu was chosen due to its apparent capability to capture the behavior of interest and the fact that there are no a priori limitations or restrictions regarding the specific expressions of the yield function and viscoplastic potential. However, it was found that in order to capture the peculiarities of the volumetric response, namely the reduced dilatancy at very high pressure, the hypothesis of existence of a viscoplastic potential has to be abandoned. A new flow rule was proposed for WES5000. Procedures for determination of the constitutive functions were developed. Comparison between the model predictions and data showed that the proposed model describes with very good accuracy the high-pressure behavior of concrete.

## CHAPTER 1

### INTRODUCTION

The past century has seen tremendous advances in the use of concrete as well as numerical techniques for the design and analysis of concrete structures. It is reasonable to say that it has become the most ubiquitous of modern construction materials, used in everything from roads and bridges to modern office structures and massive hardened military command and control facilities designed to survive blast and impact loadings. Yet, it is perhaps the least understood of construction materials. Concrete is a composite material made up of fine aggregate (sand), coarse aggregate (rock), Portland cement and water. On a micro-scale, it is a heterogeneous and anisotropic material. Yet on a macro scale, it can be treated as a continuum. It has been reported that concrete exhibits both compressible and dilatant properties, pressure dependencies, and highly rate sensitive strength and failure properties in both tension and compression. The rate effects are truly pronounced in the regimes typical of impact and blast loading problems. It is in this highly dynamic realm that the need exists for improved concrete models. A material constitutive model needs to be capable of replicating the behavior of interest and be based on data gathered in stress and strain rate regimes representative of in situ material. The strain rates of interest for various classes of impact problems were tabulated by Zukas et al. [1] and are presented in Table 1-1. Wilbeck [2] reported that the impact pressures commonly seen for explosively driven problems or kinetic energy penetrators range from on the order of the strength of the target material to the strength of the projectile respectively. This implies that the pressure range of interest varies from tens of Mega-Pascals (MPa)

to the order of a Giga-Pascal (GPa) for a case involving a high-strength steel penetrator.

Table 1-1: Strain rate response as a function of impact velocity

Striking Velocity, km/s	Strain Rate, mm/mm/s
> 12	$10^8$
3to12	$10^7$
1to3	$10^5$
0.5to1	$10^4$
0.05to0.5	$10^2$
< 0.05	$10^0$

This program of research is composed of concomitant efforts of theoretical analysis, modeling, and experimental test, the main goals of which are

- 1) To characterize the behavior of WES5000 concrete over a broad range of stress and strain rate conditions.
- 2) To develop a model that could capture the main features of the observed behavior.

The remainder of this document is outlined as follows. Chapter 2 presents a review of testing devices and experimental techniques used to characterize the quasi-static (strain rate  $\simeq 10^{-6}/s$ ) behavior of geologic materials and geologically derived materials such as concrete. The concrete material used in the program is then presented along with experimental results under unconfined and confined conditions in the range of 50 to 500 MPa.

Chapter 3 discusses dynamic material characterization. A general background on dynamic material characterization is provided followed by a description of the confined dynamic Split Hopkinson Pressure Bar technique developed for this research effort. Results are presented for strain rates on the order of  $10^1/s$  to  $10^2/s$  under both confined and unconfined conditions.

In Chapter 4, after reviewing different approaches to concrete/geologic material constitutive modeling, an elastic/viscoplastic formulation is proposed.

The structure of the model is presented, followed by derivation of the constitutive functions, and determination of the model parameters based on experimental results generated in this effort. Finally, comparisons are made between theoretical predictions and experimental data. The summary and conclusions are presented in Chapter 5.

## CHAPTER 2

### EXPERIMENTAL INVESTIGATION OF THE QUASI-STATIC BEHAVIOR

#### 2.1 Background and Overview of Testing Devices and Quasi-Static Experimental Techniques

To fully understand the mechanical behavior of a material, tests must be conducted that correspond to the range of pressures, strains, and strain rates encountered in the applications of interest. For dynamic events such as projectile penetration, pressures may vary from the gigapascal range in close proximity to the nose, to near zero at nearby free surfaces [3]. Likewise, strain rates may vary from  $10^6 \text{ s}^{-1}$  near the event to virtually quasi-static response many penetrator diameters away. There is no one mechanical testing device with which it is possible to achieve this broad range of pressures and strain rates. Figure 2-1 shows the typical mechanical testing devices and the strain rates at which they are applicable. It is reproduced from a work by Lindholm (U. S. Lindholm, High Strain Rate Testing, In R. F. Bunshah, editor, Techniques in Metals Research, volume 5. Interscience, New York, 1971 [4]). Creep to quasi-static response characterization is generally accomplished through use of a load frame device, frequently hydraulically driven. Dynamic response is investigated using Hopkinson bars, split Hopkinson pressure bars, or flyer plate experiments. These testing devices and techniques are presented in Chapter 3. To fully characterize the quasi-static mechanical behavior, tests that induce a general 3-D stress or strain in the material specimen are required. Such tests require the use of some type of load cell. This may take the form of a cube cell. In a cube cell (sometimes referred to as a “true” triaxial cell), the specimen is held between 6 platens. The advantage to this type of test is that the load in all three principal directions may be controlled independently. The experimental



apparatus is by necessity more complex and costly. Specimen fabrication may also be more complicated and the pressure levels obtainable are generally below that of interest for penetration problems. The most commonly used device is the Kármán cell, named after Theodore von Kármán, who in 1911 conducted triaxial compression experiments on marble [5]. In a Kármán experiment, a cylindrical specimen is held between two platens of a load frame and placed in a hydrostatic confinement cell.

A typical experiment consists of two phases, hydrostatic and deviatoric. In the hydrostatic phase, the specimen is subjected to an all-around pressure which is gradually increased up to a predetermined level. The confining pressure is applied via a hydraulic fluid. In the deviatoric phase, the radial pressure is held constant while an axial load is applied at a constant rate to the specimen. The axial load, applied via the platens, is increased until the specimen fails. Measurements typically recorded include axial and radial strains, confining pressure, and axial load. With modern electronic servo-controls, it is possible to closely monitor and control the load, loading rate and the confining pressure. The experiment may be run under load or strain control and may be run monotonically or with creep or relaxation cycles. Figure 2-2, taken from Chinn and Zimmerman [6], displays a cut-away view of a typical Kármán device.

By performing a series of experiments at several confining pressures, it is possible to study the influence of the maximum and minimum principal stresses on material behavior. Based on data from such tests, continuum models can be developed and further used to predict material behavior for loading conditions which are not accessible through direct testing. Detailed discussions on how to interpret the data and evaluate the constitutive parameters are well documented in the literature [7, 8, 9]. Hydrostatic pressure in such experiments is limited by both material considerations and the design restrictions of the particular Kármán cell

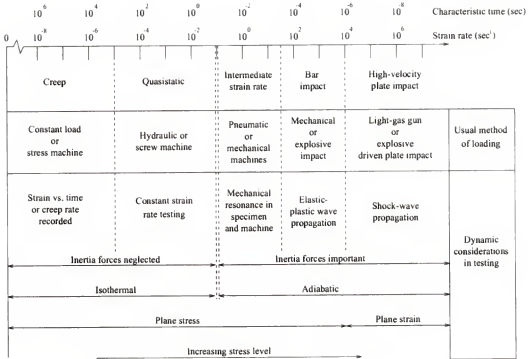


Figure 2-1: Dynamic aspects of mechanical testing

utilized. Kármán cells have been designed to accommodate hydrostatic pressures on the order of one gigapascal (GPa) [10].

Higher confining pressures, beyond 1 GPa, can be achieved through the use of a uniaxial strain compression device. Such a device is essentially a rigid cylindrical collar in which the specimen is compressed. Uniaxial strain is assumed and only the axial strain and applied load are measured. Descriptions of such devices are given by Bridgman [11] and Cristescu [12]. Drawbacks to this method include the exacting tolerances required of test specimens, often difficult to achieve with geologic material's, and the difficulty in quantifying the effects of friction in the experiment.

In this research effort, Kármán experiments were used to characterize the quasi-static behavior since this technique offered the possibility of testing over a broad range of confining pressures while allowing the measurement of both axial

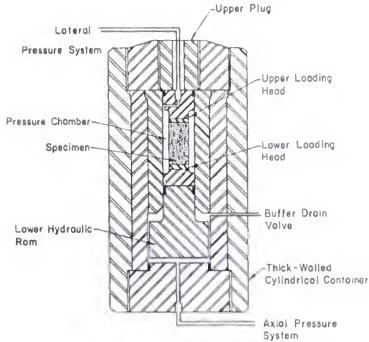


Figure 2-2: Section through triaxial Kármán device

and radial strains, and hence characterization of the volumetric behavior. The remainder of this chapter is organized as follows.

Section 2.1 describes the concrete material (WES5000) under investigation and the experimental plan. Sections 2.2 to 2.11 detail the testing protocol and the test results. Section 2.12 deals with evaluation of the elastic properties from the unload-reload cycles. Finally, Section 2.13 summarizes the quasi-static material characterization effort.

## 2.2 Material Description

### 2.2.1 Historical Note

The first use of what might be called concrete was by the the early Greeks who learned to combine lime and water with sand, crushed stone or brick and broken tiles. Archeological digs have shown that the Greeks utilized highly durable mixes as early as 1700 B.C. [13]. The Romans later learned to add a volcanic ash to the

mix. This ash, called *pozzolan* after the town of Pozzuoli Italy, gave the concrete added durability and strength. This volcanic ash is for all intents and purposes the same as the fly ash often added to modern concrete mixes. The first major use of concrete in large scale construction projects occurred in Rome approximately 2000 years ago. Perhaps the greatest example of the versatility and durability of Roman concrete is the Pantheon, constructed by the Roman Emperor Hadrian during the period 118 to 128 A.D.. It still stands in Rome and is used as a church to this day. The Pantheon is truly a marvel of ancient engineering and architecture. In fact, the 142.5 foot span of the Pantheon dome was not surpassed until the 19th century [14].

The secret of Roman concrete was lost in 410 A.D. when Alaric the Goth sacked Rome. It remained essentially lost until 1824, when Joseph Aspdin received his patent for Portland cement. Aspdin heated a mixture of finely ground clay and limestone until  $\text{CO}_2$  had been driven off, but at a temperature much lower than that required for clinkering. The prototype of modern cement did not appear until 1845 when Isaac Johnson burnt a mixture of clay and chalk until clinkering, so that the reactions necessary for the formation of strongly cementitious compounds took place [15]. Joseph Monier deserves the credit for making the first practical use of reinforced concrete in 1867, while the first cast-in-place concrete structures in the United States began appearing in the 1870s [16].

The French development of the explosive shell from 1885-90 led to the introduction of concrete into military construction as traditional masonry fortifications proved no match for the new offensive technology [17]. World War II saw the transition away from forwardly positioned defensive fortifications such as the French Maginot line, designed to counter a land based adversary, towards the use of hardened command control and communications facilities designed for defense against air delivered munitions. Since that time, the proliferation of concrete bunkers

has spread worldwide as nations have sought to protect vital national assets from conventional and nuclear threats. Today, the targeting of civilian structures by terrorist groups as well as an increased emphasis worldwide on building more earthquake resistant structures has made the understanding of construction materials, such as concrete, to dynamic loads far more than a matter of purely military interest.

### 2.2.2 Material Studied, WES5000

The concrete selected for study is referred to as WES5000. The aggregate size is such that it must pass through a 3/8 inch (9.5 mm) sieve. The 5000 stands for 5000 psi (34.5 MPa) unconfined compressive strength, the original design specification. In reality, the 90 day unconfined compressive strength is nominally 7000 psi (48.3 MPa). The ingredients and proportions for the mix are given in Table 2-1

Table 2-1: Ingredients and mixture proportions for WES5000 concrete.

Item	Mixture proportions, saturated surface-dry
Type I Portland cement	264.0 $kg/m^3$
Flyash	55.8 $kg/m^3$
9.5 mm local unprocessed chert coarse aggregate	1037.6 $kg/m^3$
Local unprocessed chert fine aggregate	840.7 $kg/m^3$
Water	145.9 $kg/m^3$
Water reducing admixture "300N"	0.65 $l/m^3$
High-range water reducing admixture "Rheobuild 716"	1.6 $l/m^3$

WES5000 was first formulated at the U.S. Army Corps of Engineer Research and Development Center Waterways Experiment Station (WES) as a standard test concrete for phenomenology studies. As such, a great deal of data exist for validation of the model. The WES5000 used in this study was poured by WES on 6 May 1998. The material was cast into two barrels and allowed to cure for approximately 30 days prior to coring. Two different diameter cores were taken. The cores for triaxial quasi-static testing were nominally 50mm in diameter and

were cut into lengths of approximately 110mm. The cores for Split Hopkinson Pressure Bar (SHPB) testing were nominally 75mm in diameter and were cut into lengths of approximately 76mm. The end faces on each sample were then ground to assure parallelism. Both unconfined compression and splitting tension tests were conducted at 28 days. Results of these experiments are presented in Table 2 2.

Table 2-2: Properties at 28 days for WES5000 concrete.

Test #	Unconfined compression	Splitting tension
1	45.85 MPa (6650 psi)	3.31 MPa (480 psi)
2	45.85 MPa (6650 psi)	3.07 MPa (445 psi)
3	45.16 MPa (6550 psi)	3.00 MPa (435 psi)
Avg.	45.62 MPa (6617 psi)	3.13 MPa (453 psi)

### 2.3 Experimental Design

One of the objectives of the experimental study was to determine the quasi-static behavior of WES5000 under a variety of loading conditions. Of particular interest was the influence of confining pressure on strength, and the material's deformation properties. The simplest characterization experiment which can be conducted is a uniaxial, or unconfined compression test. For most civil engineering applications, this is the only experiment which is run. Figure 2-3 shows a representation of a uniaxial compression test in which both axial and radial strains have been recorded. The pre-peak portion of the axial stress-strain curve is essentially linear over the first one third. The Young's modulus (or tangent modulus) may be taken as the slope of this line. An estimate of the Poisson ratio may also be determined from the ratio of the radial to axial strains over this linear portion. These moduli would only be applicable in static civil engineering applications where pressure or compression are not important. The most frequently reported measurement from such a test is the peak stress, or unconfined compressive strength, often denoted as  $f'_c$ . This term is more useful as a quality control measure than an actual material property.

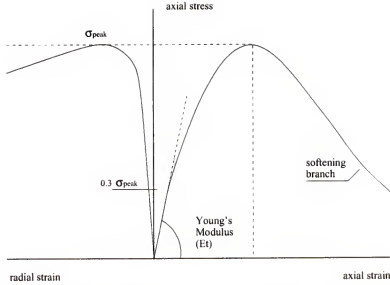


Figure 2-3: Stress-strain curve for concrete uniaxial compression test

ASTM C 801-91 [18] defines the American standard test method for determining the mechanical properties of concrete under triaxial loads. It calls for a series of monotonic Kármán type experiments conducted under one of three loading histories.

- Type I. Hydrostatic pressure is increased monotonically to a predetermined level, then held constant while the axial stress is increased monotonically until failure occurs.
- Type II. Hydrostatic pressure is increased monotonically to a predetermined level, then the axial stress is held constant while the lateral stress is decreased monotonically until failure occurs (lateral expansion test).
- Type III. The ratio of axial to lateral stresses is held constant and the stresses are increased monotonically until failure occurs (proportional loading test).

Under the conditions of a Kármán experiment, the stress tensor is given by Equation 2.1, where  $\sigma_3$  is the lateral, or radial load applied to the specimen via the hydraulic confining fluid. This radial load is also simply referred to as confinement

or  $\sigma_3$  throughout the text.

$$\sigma_{ij} = \begin{pmatrix} \sigma_1 & & \\ & \sigma_3 & \\ & & \sigma_3 \end{pmatrix} \quad (2.1)$$

Hydrostatic pressure, or mean normal stress, is defined as one-third the trace of the stress tensor, or

$$p = \frac{1}{3}(\sigma_1 + 2\sigma_3) \quad (2.2)$$

where  $p$  is used to represent the hydrostatic pressure, or mean normal stress.

In all of these tests, axial and radial strains are measured, as well as applied axial and radial loads. Thus, information regarding the volumetric response of the material and the failure surface as a function of confining pressure may be gathered. Tests of Type *I* are usually performed for characterization purposes and provide all the information necessary for the formulation of continuum level models. Tests of Type *II* and *III* are generally run for validation purposes. Information regarding the elastic moduli may be gathered in the same means as discussed for unconfined compression. In practice, unload-reload cycles are generally included in the loading profiles for determination of the elastic properties. The moduli are taken as the slope of the unload-reload curves. Figure 2-4 displays the results of a hydrostatic compression test on WES5000 with one unload-reload cycle. Significant hysteresis is evident in the unload-reload cycle. This hysteresis can make determination of the unload-reload slopes highly subjective. Cristescu [12, 7] has shown that the introduction of a creep stage (i.e. stress state held constant) prior to the unload-reload cycle eliminates the viscous effects such that unloading is purely elastic. In a creep experiment, the specimen is allowed to deform under a state of constant stress. The evolution of the strain with time is monitored until the strain rate of the material approaches zero. This is indicative that the material



has reached a stabilized state. Unloading and reloading from this stabilized state should not be influenced by viscous properties and the material response should be purely elastic. In order to evaluate the viscosity of the material, as well as

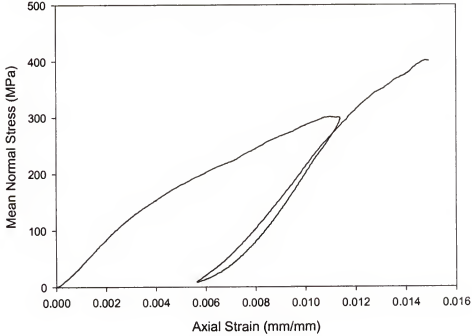


Figure 2-4: Monotonic hydrostatic compression test exhibiting hysteretic behavior

minimizing its effect on any unloading-reloading cycles, the decision was made to include a creep step prior to any unloading-reloading. Furthermore, by including several such cycles (creep-unload-reload) in each phase of the experiment the quantity of information gathered could be maximized. Figures 2-5 and 2-6 show the proposed hydrostatic and deviatoric experiments respectively. Figure 2-5 is presented in terms of volume strain as a function of mean normal stress, where volume strain is defined as the trace of the strain tensor, or under the conditions of a Kármán experiment as:

$$\varepsilon_v = \varepsilon_1 + 2\varepsilon_3 \quad (2.3)$$

where  $\varepsilon_v$ ,  $\varepsilon_1$ , and  $\varepsilon_3$  are the volume strain, axial strain and radial strain respectively. The terms  $\dot{\varepsilon}_v$  and  $\dot{\varepsilon}_1$  in Figures 2-5 and 2-6 are the time rate of change,

or strain rate for the volume strain and axial strain respectively. The over-dot notation will be utilized throughout this text to signify time rate of change.

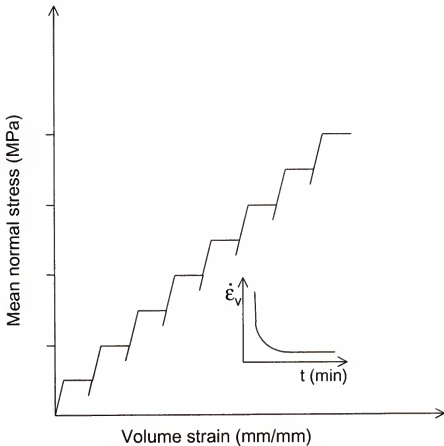


Figure 2-5: Schematic of hydrostatic creep experiment

A series of such experiments was conducted at the U. S. Army Corps of Engineer Engineering Research and Development Center, Waterways Experiment Station in Vicksburg Mississippi to fully characterize the material. The experimental matrix is given in Table 2-3. In this table under test type, TXC refers to a triaxial compression test, while UC refers to uniaxial compression. Creep implies creep steps were included. One experiment, 9902B016, was run with relaxation steps. The presence of asterisks in the data columns implies that no data of that type was taken in the experiment. This was usually due to failure of the membrane separating the material specimen from the hydraulic fluid.



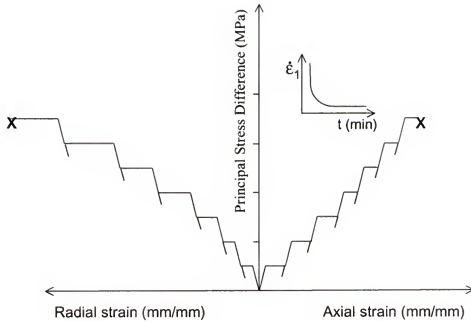


Figure 2-6: Schematic of deviatoric shear creep experiment

Prior to each test, the WES5000 specimen was carefully weighed and measured. Post test, the specimens were dried in an oven to remove all moisture. This allowed calculation of the specimen as tested density as well as the dry density, and hence the as-tested moisture content of the material could be evaluated. Axial and radial P-wave and S-wave velocity measurements were also taken. The results are given in Table 2-3. WES5000 is inherently rather porous and prone to having voids, making it a difficult material with which to work. This porous nature makes it impractical to directly instrument the specimens with strain gauges except at very low confining pressures. At higher pressures, the thin gauge substrate would be prone to “popping” into the tiny voids or pores over which it had been applied, thus rendering it non-functional. Rather, Linear Variable Differential Transformers (LVDTs) were utilized to measure the axial and radial deformation of the material. The LVDT is an electromagnetic device that produces an electrical voltage proportional to the displacement of a movable magnetic core. These LVDTs were housed in a “bird cage” apparatus surrounding the specimen. The radial LVDTs were

connected via two metal studs glued to the specimen midpoint at diametrically opposite points. Since pressure is transmitted to the specimen via a confinement fluid, precautions must be taken to prevent fluid infiltration into the specimen. The specimen is generally encased in a latex membrane. Care must be taken in specimen preparation to open and patch all surface voids in order to prevent the membrane from being forced down into these voids and punctured. A gypsum paste was used to patch all voids. Subsequent to patching of the voids, the specimen was encased in the latex membrane, and this membrane was then surrounded by a layer of plumbers putty. The putty served the function of self sealing any potential punctures of the inner membrane. A second latex membrane was then applied over the putty and the membrane coated with a sealant to prevent its degradation by the petroleum based hydraulic fluid. Figure 2-7 displays a sample prepared for testing with radial LVDTs attached. The entire “bird cage” is then lowered into the confinement cell for testing. WES’s Secodyne 500K pound load frame (see Figure 2-8) coupled with a 600 MPa capacity Kármán cell was utilized for all the experiments. The loading rate/profile was computer programmable, allowing for precise control of the experiments under load, displacement or strain control.

## 2.4 Unconfined Compression

The first experiment conducted (9902A02) was a monotonic unconfined compression test. While not generally revealing from a model development standpoint, the unconfined compressive strength, or  $f'_c$ , is an often quoted figure of merit when comparing various concrete mixes or individual batches. Figure 2-9 shows the results of the experiment. In this case, the specimen was instrumented with both axial and radial strain gauges as well as axial and radial LVDTs. Note the very close correlation apparent between the LVDT and radial strain gauge signals. For the axial strain, there appears to be an initial difference in the signals with the



Figure 2-7: Sample prepared for testing



Figure 2-8: Waterways Experiment Station Secodyne 500K pound load frame

LVDTs indicating a greater amount of axial deformation. This initial discrepancy is most likely due to localized effects at the platen-specimen interface at the onset of the experiment. The strain gauges would not record these effects since they could measure deformations only in the vicinity of the point where they are attached. The LVDTs on the other hand record the deformation of the entire specimen. However, after this initial stage, which shall be referred to as “seating”, strain gauge and LVDT signals are in excellent agreement. The compressive-dilatant nature of the material can be determined from examination of the volume strain curve. A positive volume strain slope is indicative of material compressibility, while a negative slope indicates material dilatancy. Therefore, from the volume stress-strain curve, it may be concluded that the material is initially compressible, but becomes dilatant as the stress increases. The transition point from compressibility to dilatancy is referred to as the compressibility-dilatancy boundary. The unconfined compressive strength at 121 days curing time was found to be 60 MPa (8685 psi).

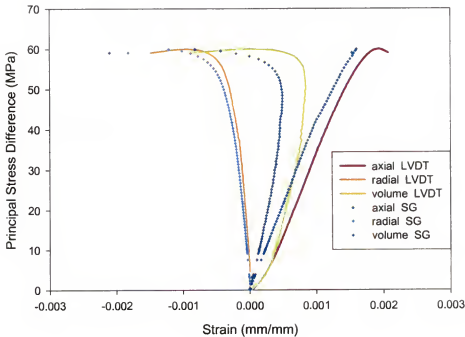


Figure 2-9: Unconfined compression test



## 2.5 300 MPa Experiment

The initial test matrix developed, called for a series of hydrostatic compression phase followed by deviatoric phase experiments with several loading-creep-unloading-reloading cycles. The loading rates were to be held such that the axial strain rate would be on the order of  $10^{-6}$ . Creep cycle duration was to be on the order of 30 minutes to allow the material to achieve stabilization. Tests were run under these conditions at 150, 300 and 450 MPa confinement. Results of the 300 MPa experiment (9902B01) are presented in Figures 2-10 through 2-15. The convention observed in this dissertation is that compressive stresses and strains are positive. Measurements were recorded at one second intervals. Figure 2-10 shows the hydrostatic compression phase of the experiment. At the onset of loading, there appears to be a sudden negative jump in the radial strain. This is not believed to be indicative of any material behavior, rather it is likely associated with specimen "seating". The axial and radial strains correlate well, hence the material can be considered isotropic. If a correction were made for the initial offset on the radial LVDT, the correlation between the two signals would be even greater. Upon examination however, the response of the unload-reload cycles for the radial signal appears far too stiff. The degree of hysteresis in the signal also appears to be significant. This is especially peculiar since there is virtually no hysteresis apparent in the axial signal. Figure 2-11 displays only the first two cycles of the hydrostatic loading. Here the initial radial offset is more visible. It is also more clearly visible that there is virtually no hysteresis present in the axial unload-reload cycles. This is indicative of the fact that the material has had time to reach stabilization via creep (i.e. it is on the stabilization boundary) and that it is responding elastically upon unloading. This is not observed in the radial signal, further bringing into question the validity of the radial unload-reload data. Figures 2-12 through 2-15 present the deviatoric response of the material. The quality of the axial signal

appears quite good, with little apparent hysteresis in the unload-reload cycles. A peak principal stress difference (PSD) of 504 MPa was achieved in the experiment. Figures 2-13 and 2-14 show the radial deformeter data. Inspection of the first creep cycle indicates that the material is creeping in the positive direction (radial contraction). According to Cristescu [8] this behavior has been observed in creep testing of highly porous rocks. At the second creep stage, the material is exhibiting oscillatory behavior between expansion and contraction. On subsequent cycles, the material exhibits only radial expansion in the creep cycles. There is still some degree of hysteresis apparent in the radial unload-reload cycles, though far less than observed in the hydro phase of the experiment. The first three cycles alone are displayed in Figure 2-14. Here the creep behavior can more clearly be seen. There is a good deal of noise in the data surrounding the second creep cycle. This may have been due to localized aggregate cracking or void collapse influencing the radial signals. There was also a certain amount of oscillation recorded at the onset of the deviatoric test. This is not believed to be indicative of any true material behavior. Overall, the confidence in the radial LVDT data is considered low. Figure 2-15 depicts the axial radial and volumetric curves together. It can be seen from the volume curve that the material exhibits purely compressible behavior up to the onset of failure. The complete experiment was conducted over a period of 6 hours and 38 minutes.

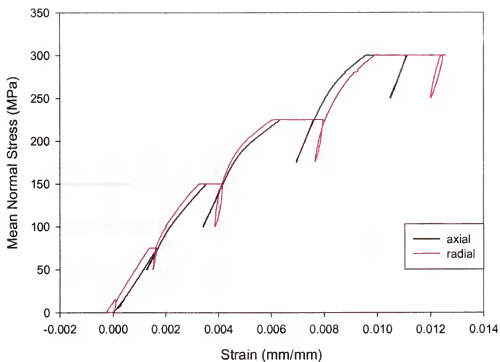


Figure 2-10: Hydrostatic compression phase, 300 MPa Kármán experiment

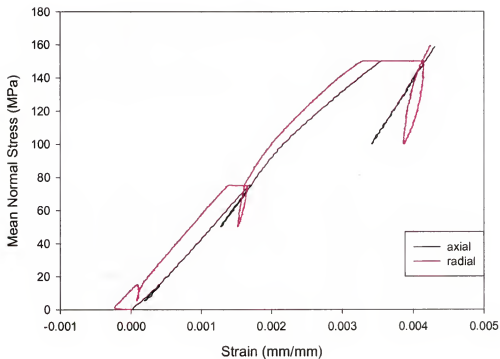


Figure 2-11: Hydrostatic compression phase (low pressure range), 300 MPa Kármán experiment

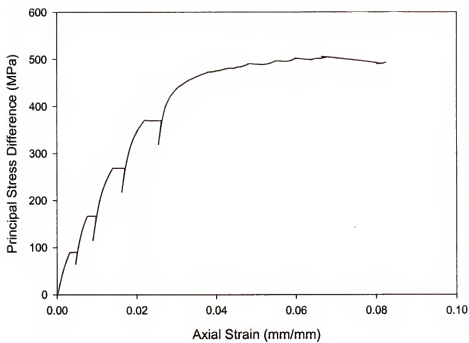


Figure 2-12: Deviatoric phase of 300 MPa Kármán experiment, axial strain

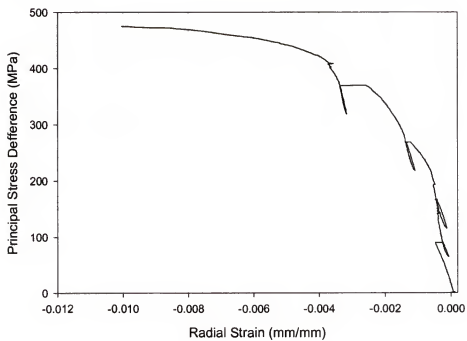


Figure 2-13: Deviatoric phase of 300 MPa Kármán experiment, radial strain

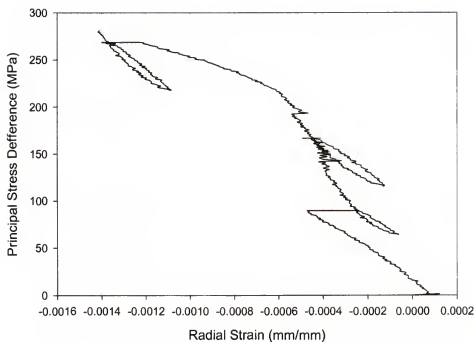


Figure 2-14: Deviatoric phase of 300 MPa Kármán experiment, radial strain (low PSD range)

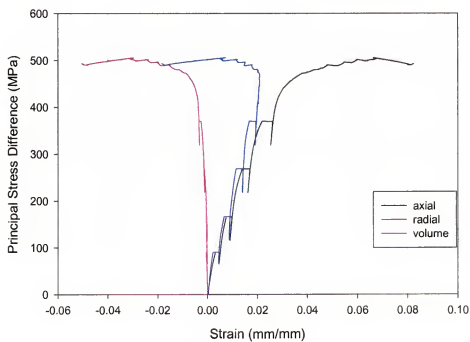


Figure 2-15: Deviatoric phase of 300 MPa Kármán experiment, all strains

## 2.6 450 MPa Experiment

Results of the tests run at 450 MPa radial confinement (9902B02) are presented in Figures 2-16 through 2-21. Figure 2-16 shows the full hydrostatic compression phase of the experiment. At first glance, the behavior of the material does not appear to be isotropic in that the axial and radial signals do not appear to correlate well. However, the difference is actually rather small (on the order of a few tenths of a percent strain) and may well be within the accuracy limits of the LVDTs. The overall behavior of the radial signals is much improved over those in the 300 MPa creep experiment, with little apparent hysteresis in the unload-reload cycles. Figure 2-17 shows a detailed view of the first 2 cycles. Some evidence of the axial seating phenomena is visible, but it is not pronounced. Figures 2-18 through 2-21 display the deviatoric phase of the experiment. There was again an apparent anomaly in the data at the onset of the deviatoric phase, much like that discussed for 9903B01. However, as presented here, the data has been adjusted to remove the initial offsets. The axial LVDT results, as depicted in Figure 2-18, appear quite good with a peak principal stress difference of 671 MPa achieved. Figure 2-19 presents the complete radial signal. Once again, there is some degree of hysteresis apparent in the unload-reload cycles which was not seen in the axial signals. Figure 2-20 displays in detail the first two cycles. The initial oscillatory behavior is again observed at the first creep cycle, however the creep direction is negative for the second and all subsequent cycles. Finally, Figure 2-21 shows the axial, radial, and computed volumetric curves together. Again it is seen that the material is compressible until very near the onset of failure. The complete experiment was conducted over 8 hours and 12 minutes.

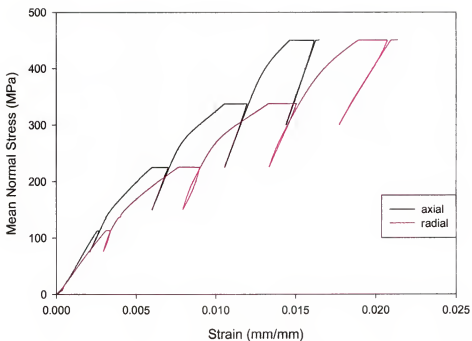


Figure 2-16: Hydrostatic compression phase, 450 MPa Kármán experiment

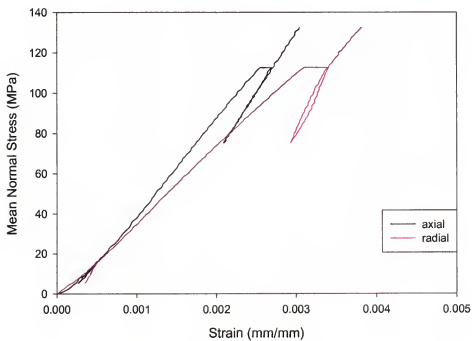


Figure 2-17: Hydrostatic compression phase (low pressure range), 450 MPa Kármán experiment

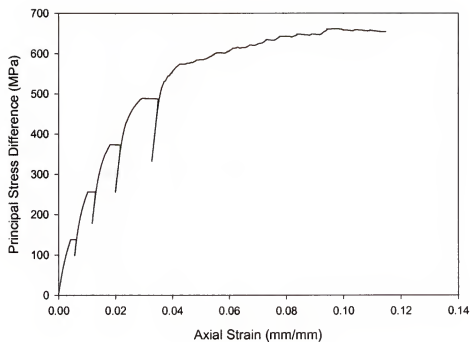


Figure 2-18: Deviatoric phase of 450 MPa Kármán experiment, axial strain

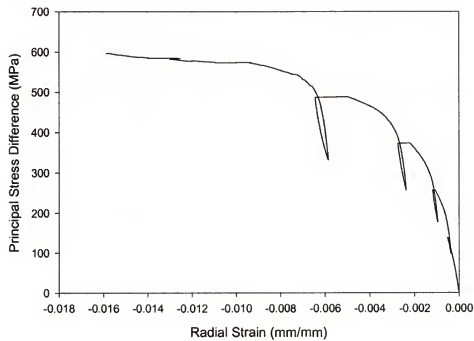


Figure 2-19: Deviatoric phase of 450 MPa Kármán experiment, radial strain



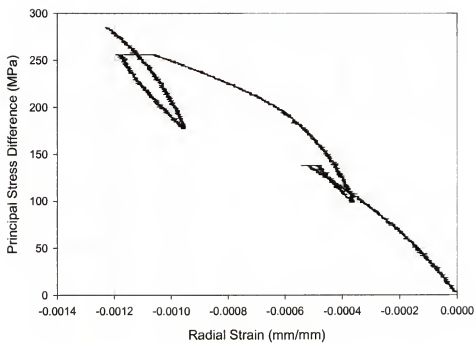


Figure 2-20: Deviatoric phase of 450 MPa Kármán experiment, radial strain (low PSD range)

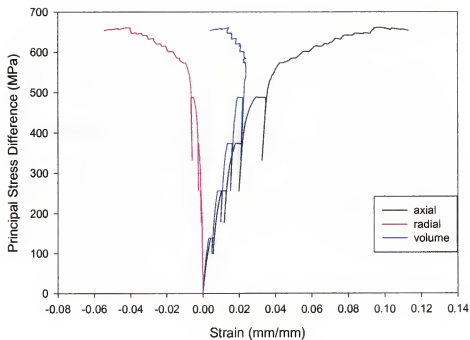


Figure 2-21: Deviatoric phase of 450 MPa Kármán experiment, all strains

## 2.7 150 MPa Experiment

Results of the 150 MPa experiment (9902B08) are presented in Figures 2-22 through 2-27. Figure 2-22 displays the hydrostatic compression phase of the experiment. Results seem to indicate that the material is not behaving very isotropically. Even taking into account the initial platen-specimen interface seating phenomena, the radial response appears much stiffer. This can be seen clearly in the slopes of the corresponding unload-reload cycles. Figure 2-23 presents the first two cycles of the hydrostatic compression experiment. Here the platen-specimen interface phenomena discussed earlier for the unconfined experiment can be clearly seen. Figures 2-24 through 2-27 present the deviatoric response of the material. The axial strain results appear quite good, with a peak principal stress difference of approximately 390 MPa achieved. Once again, the radial signals indicate a certain amount of hysteresis. Radial contraction is again seen in the first creep cycle with the onset of the oscillatory phenomena visible in the second cycle. This can be more clearly seen in Figure 2-26. Figure 2-27 displays all the strain signals together. Again the transition to dilatancy is not apparent in the volume strain signal until the onset of failure.

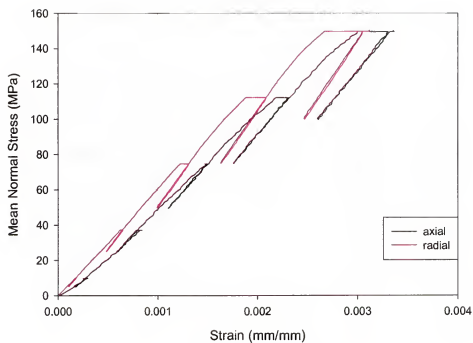


Figure 2-22: Hydrostatic compression phase, 150 MPa Kármán experiment

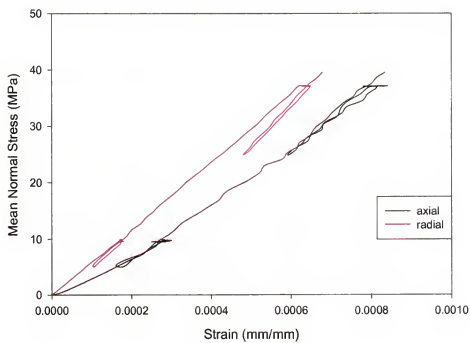


Figure 2-23: Hydrostatic compression phase, 150 MPa Kármán experiment, first 2 cycles

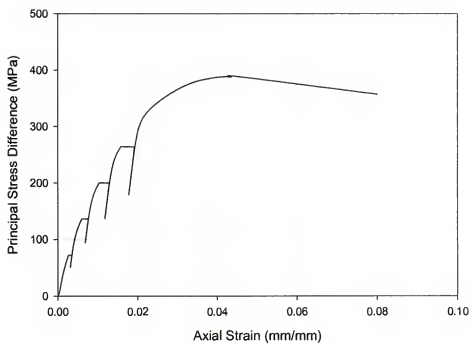


Figure 2-24: Deviatoric phase of 150 MPa Kármán experiment, axial strain

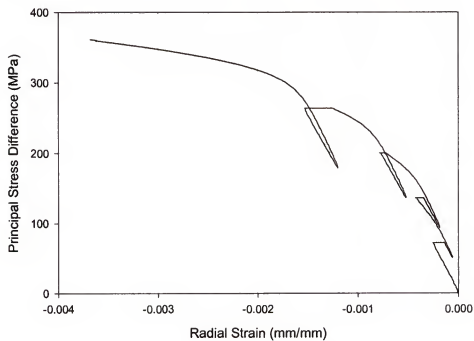


Figure 2-25: Deviatoric phase of 150 MPa Kármán experiment, radial strain

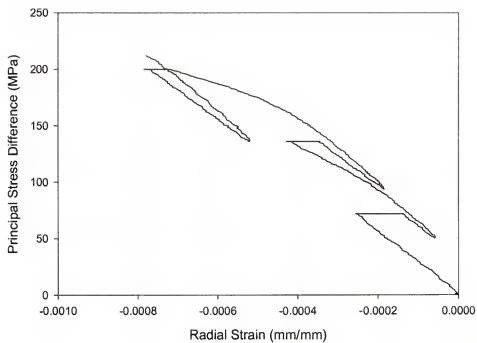


Figure 2-26: Deviatoric phase of 150 MPa Kármán experiment, radial strain (low PSD range)

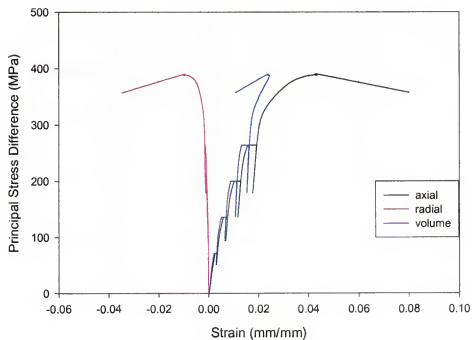


Figure 2-27: Deviatoric phase of 150 MPa Kármán experiment, all strains

## 2.8 500 MPa Hydrostatic Compression Experiment

Following completion of the 150 MPa experiment, a decision was made to re-examine the experimental procedure. Consistent anomalies had been apparent in the radial strain measurements for the experiments conducted so far. These were believed to be at least partly due to calibration of the LVDTs. For a full experiment, the expected level of radial deformation in the deviatoric phase can be expected to be on the order of 10% (see Figure 2-25), while the total deformation in the compression phase is generally on the order of 1%. Therefore, LVDTs ranged for the total expected level of deformation in the compression-deviatoric shear experiment may not be sensitive enough to record the very small strains in the hydrostatic phase. The duration of the experiments was also proving to be taxing on the equipment and technicians, this in turn was driving up the cost of the experimentation. In order to resolve the issue of instrumentation sensitivity, it was decided to conduct one additional purely hydrostatic compression experiment with multiple creep-unload-reload cycles. Since only the hydrostatic portion would be conducted, the LVDTs could be more appropriately calibrated. All subsequent experiments would be run with a monotonic hydrostatic compression phase, followed by a full deviatoric test (with creep-unload-reload cycles). Since at the end of the creep cycle the material response is theoretically purely elastic, the unloading could be conducted at as high a rate which could be easily controlled. These last two modifications were made in an effort to shorten the length of the experiments.

Results of the 500 MPa hydrostatic compression experiment (9902B012) are presented in Figure 2-28. A total of 7 creep-unload-reload cycles were conducted, with the creep pressure held for a duration of 15 minutes. The material appears to behave quite isotropically up to the fifth creep-unload-reload cycle. At this point the response of the radial gauges indicates much stiffer response than is indicated by the axial gauges. Overall, the quality of the data appears excellent for both

axial and radial measurements. Figure 2-29 displays the first two creep-unload-reload cycles in detail. Once again, there is good correlation between the two signals. The absence of a discernable creep plateau at 50 MPa is indicative that the material is responding largely elastically at this pressure range. Finally, Figure 2-30 displays a plot of volume strain rate as a function of time for the 500 MPa hydrostatic compression experiment. The plot indicates that for the four cycles, the volume strain rate has dropped to very nearly zero by the end of the creep phase. As predicted, there is virtually no hysteresis apparent in the unload-reload phase following these initial cycles. In the final three cycles, the volume strain rate does not reach zero prior to the unload-reload phase (there is no reload following the seventh creep cycle), and there is indeed a small degree of hysteresis apparent following the sixth cycle. The overall duration of the experiment was 3 hours and 3 minutes.

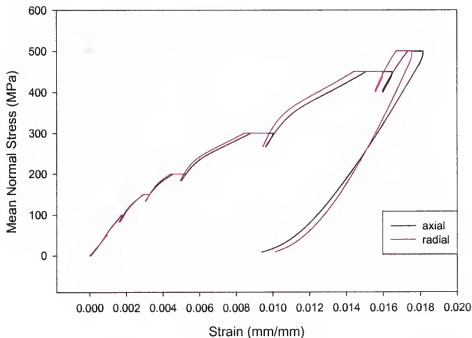


Figure 2-28: Hydrostatic compression Kármán experiment to 500 MPa

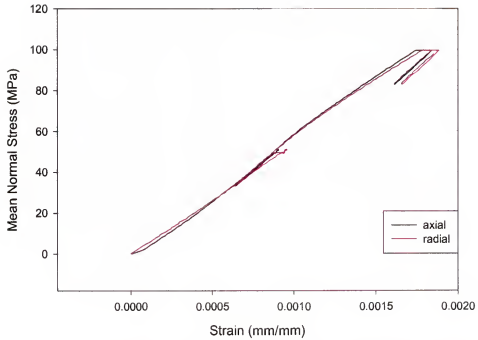


Figure 2-29: Hydrostatic compression Kármán experiment to 500 MPa, first 2 cycles

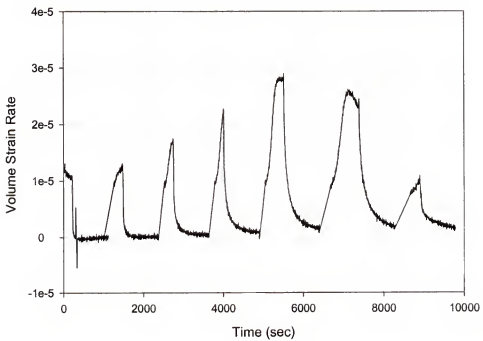


Figure 2-30: Volume strain rate vs. time for 500 MPa hydrostatic compression experiment



## 2.9 50 MPa Experiment

Following the 500 MPa hydrostatic compression test, experiments were run at 50 MPa, 200 MPa, 300 MPa, 100 MPa and 375 MPa radial confinement. Results of the 50 MPa experiment (9902B013A) are presented in Figures 2-31 through 2-35. Figure 2-31 displays the results of the monotonic hydrostatic compression phase of the experiment. Close examination of the data shows a small initial negative offset to the axial data, indicative of specimen seating. There does not appear to be good correlation between the axial and radial signal for this phase of the experiment. One should consider however that the magnitudes of the measured strain is quite small with respect to the calibration of the instrumentation. Figure 2-32 displays the axial strain signal as a function of principal stress difference for the deviatoric shear portion of the experiment. The quality of the data appears quite good with no hysteresis evident in the unload-reload cycles. There is a good deal of "jitter" in the signal for the final unload-reload cycle and the subsequent load to failure. This is perhaps indicative of material damage. Figure 2-33 shows the radial strain signal for the deviatoric shear phase. Once again, there is evidence of radial expansion in the first creep cycle. The overall quality of the data appears good with no significant hysteresis in the unload-reload cycles. The first two creep-unload-reload cycles are detailed in Figure 2-34. Here the radial expansion in the first cycle can be clearly seen, as well as oscillatory behavior in the second cycle. Close inspection also indicates that there is some lag in the response of the radial signal at the onset of the deviatoric loading. The initial lack of appreciable radial strain at the onset of the deviatoric phase, and following the reload portion of the first cycle is evidence of this lag in response. Finally, Figure 2-35 displays all the signals together. The transition from compressibility to dilatancy is apparent in the volumetric strain signal only near failure. The material exhibits strain hardening behavior up to failure, indicative of a brittle material. The sample achieved a peak

principal stress difference of 221 MPa prior to failure. The overall length of the experiment was 2 hours and 51 minutes.

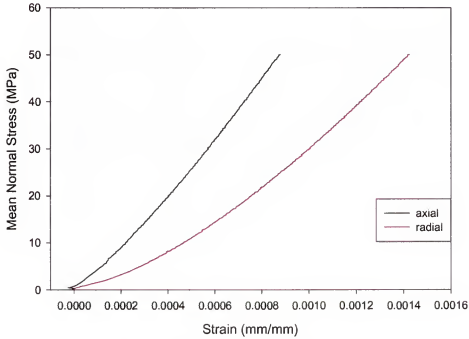


Figure 2-31: Hydrostatic compression phase, 50 MPa Kármán experiment

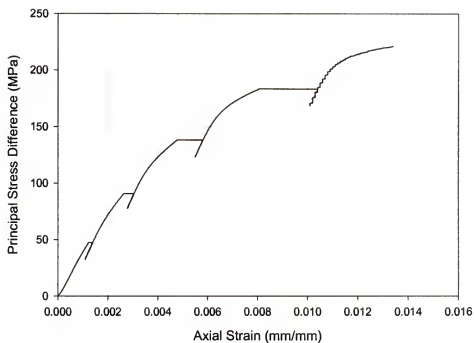


Figure 2-32: Deviatoric phase of 50 MPa Kármán experiment, axial strain

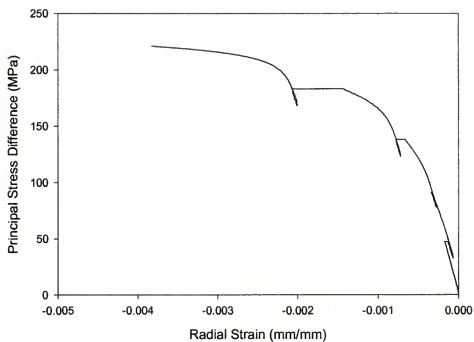


Figure 2-33: Deviatoric phase of 50 MPa Kármán experiment, radial strain

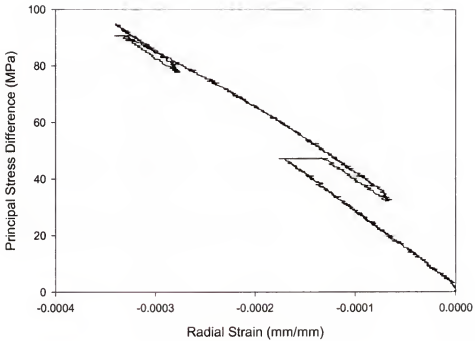


Figure 2-34: Deviatoric phase of 50 MPa Kármán experiment, radial strain first 2 cycles

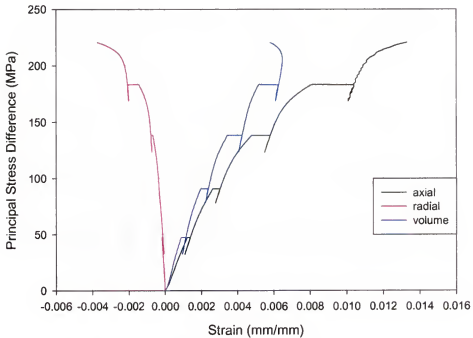


Figure 2-35: Deviatoric phase of 50 MPa Kármán experiment, all strains

## 2.10 200 MPa Experiment

The next series of figures (2-36 through 2-40) displays the results of the 200 MPa radial confinement experiment (9902B014). Figure 2-36 shows the axial and radial strain signals for the monotonic hydrostatic compression phase of the experiment. Excellent correlation is indicated between the two signals indicating a high degree of material isotropy. The next figure presents the axial strain signal as a function of principal stress difference for the deviatoric shear phase of the experiment. Again the quality of the data appears very good with no hysteresis apparent in the unload-reload cycles. The radial response for the deviatoric phase of the experiment is presented in Figure 2-38. Again, there are indications that the gauges are not initially responding to the applied deviatoric load. The response lag is far more pronounced in this experiment than it was in the 50 MPa experiment. The first creep cycle again displays radial expansion. There does not appear to be any appreciable level of hysteresis in the final two creep-unload-reload cycles. An expanded view of the first two cycles is shown in Figure 2-39. Here, the lag in response is clear not only at the onset of deviatoric loading, but also following the first unload cycle. It is most likely that this lag is due to a mechanical problem in the LVDT cage apparatus. The slope of the reload side, once the gage begins responding, is very close to that from the unload side. The second cycle once again displays oscillatory behavior in the creep cycle and there is again indication of the LVDT not responding for the reload portion of the cycle, though to much less a degree. The volumetric, axial and radial signals are presented together in Figure 2-40. Once again, the transition from compressibility to dilatancy is only apparent at the onset of failure. The material does not show signs of strain hardening in this experiment, rather, near failure, the stress level is constant for increasing strain. This is indicative of a transition from brittle to ductile behavior. A peak principal

stress difference of 457 MPa was achieved in the experiment, which was conducted over a period of 3 hours and 44 minutes.

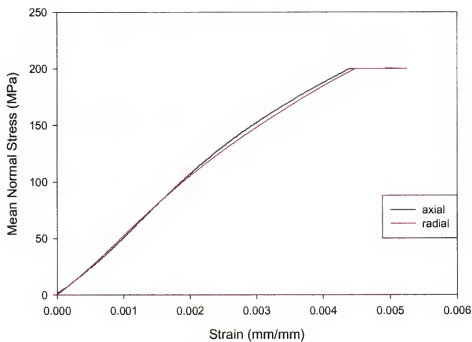


Figure 2-36: Hydrostatic compression phase, 200 MPa Kármán experiment

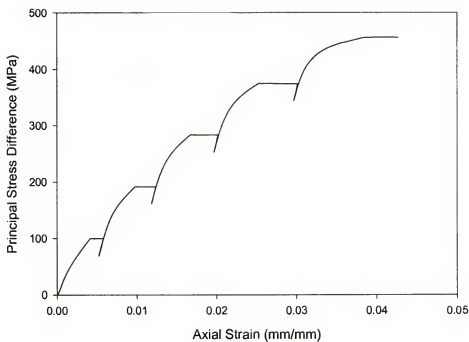


Figure 2-37: Deviatoric phase of 200 MPa Kármán experiment, axial strain

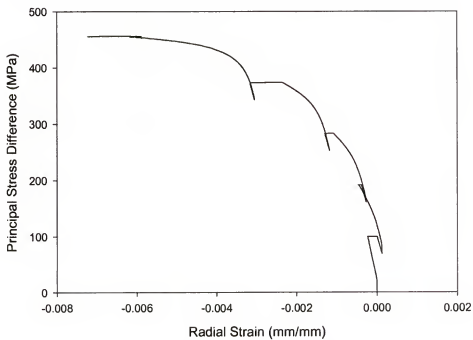


Figure 2-38: Deviatoric phase of 200 MPa Kármán experiment, radial strain

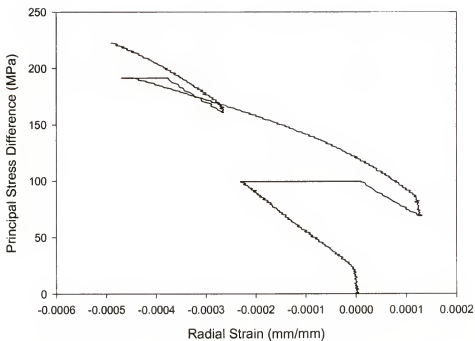


Figure 2-39: Deviatoric phase of 200 MPa Kármán experiment, radial strain first 2 cycles

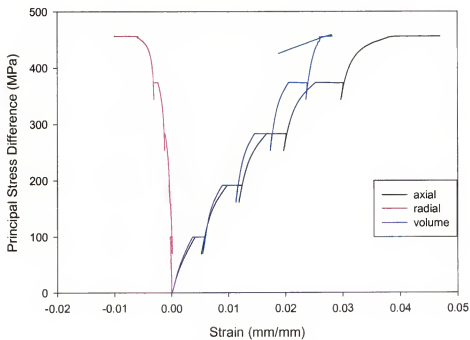


Figure 2-40: Deviatoric phase of 200 MPa Kármán experiment, all strains



### 2.11 300 MPa Experiment (Second)

The next experiment was conducted at a radial confinement of 300 MPa (9902B015). This second experiment under the 300 MPa confinement conditions was intended to serve two purposes. First, it was desirable to conduct a second experiment under nearly identical conditions due to the obvious problems with the radial deformeters in the first experiment. Second, it would give some qualitative sense regarding the reproducibility of the experiments. Figure 2-41 displays the results of the monotonic hydrostatic compression phase of the experiment. There is generally very good agreement between the two signals. Axial strain results for the deviatoric shear phase of the experiment are presented in Figure 2-42. Once again, the quality of the data is excellent with no significant hysteresis in the unload-reload cycle. Following the final creep cycle, the data exhibits a significant amount of noise which is likely due to aggregates breaking in the specimen. Figure 2-43 displays the radial strain signal as a function of principal stress difference. The familiar radial expansion and subsequent oscillating behavior in the first two creep cycles is again evident. Following the final creep-unload-reload cycle, there is a significant “glitch” in the data indicated by a sudden radial expansion. This point corresponds to the onset of noise in the axial signal and is likely due to a localized aggregate fracture or void collapse in the vicinity of the radial gauge mounts. Figure 2-44 presents a detailed view of the radial strain for the first two creep-unload-reload cycles. There is no evidence here of the response delay observed in the previous two experiments. All the signals are presented together in Figure 2-45. Again, the transition from compressibility to dilatancy is only very near material failure. The entire experiment was conducted over a period of 4 hours and 15 minutes, a significant reduction from the 6 hours and 38 minutes in the first 300 MPa experiment. A peak principal stress difference of 570 MPa was achieved in the experiment, somewhat higher than the 504 MPa measure in

the first 300 MPa experiment. This difference is no doubt due partly to natural experimental scatter, but also to the additional work performed on the specimen in the hydrostatic compression creep cycles of the first experiment.

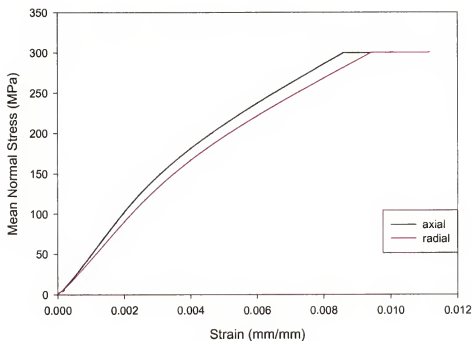


Figure 2-41: Hydrostatic compression phase, 300 MPa Kármán experiment

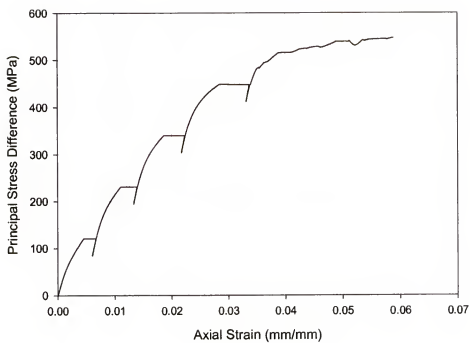


Figure 2-42: Deviatoric phase of 300 MPa Kármán experiment, axial strain

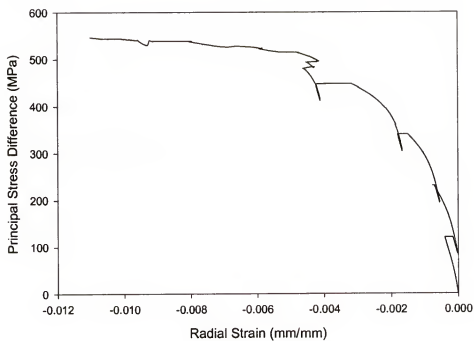


Figure 2-43: Deviatoric phase of 300 MPa Kármán experiment, radial strain

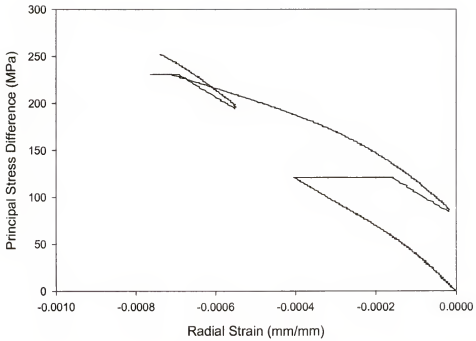


Figure 2-44: Deviatoric phase of 300 MPa Kármán experiment, radial strain first 2 cycles

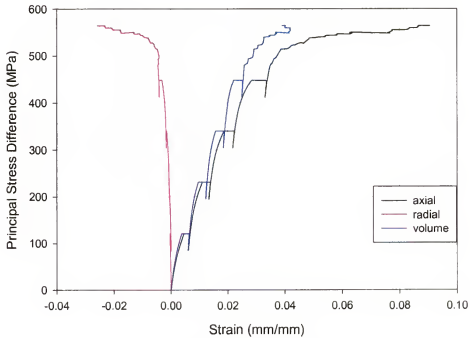


Figure 2-45: Deviatoric phase of 300 MPa Kármán experiment, all strains

### 2.12 100 MPa Experiment

The next experiment conducted was at 100 MPa radial confinement (9902B016). This experiment differed from the previous ones in that relaxation cycles were included in lieu of creep cycles. In a relaxation cycle, the applied stress is controlled in such a way that the strain remains constant. For this experiment, only the axial stress was feedback controlled, the radial confining pressure remained constant. This experiment was included in the matrix to provide an alternate stress path for later constitutive model validation. Results of the monotonic hydrostatic compression phase of the experiment are depicted in Figure 2-46. Correlation between the axial and radial strain signals are again quite good. The axial strain as a function of principal stress difference for the deviatoric shear phase of the experiment is presented in Figure 2-47. The quality of the data appears quite good with no hysteresis apparent in the unload-reload cycles. Radial strain results are depicted in Figure 2-48. Since the confining pressure was not adjusted to control the radial strain, data was not constant throughout the relaxation phase. The response appears to be initially invariant, followed by radial expansion up to the unload cycle where the slope increases significantly. During the reload cycle, the LVDT response lag seems to have reappeared. This response lag can more clearly be seen in Figure 2-49, which depicts the first two relaxation-unload-reload cycles in detail. Finally, all the signals are presented together in Figure 2-50. In this experiment, the material was not tested to failure and as the volumetric strain curve indicates, remained purely compressive throughout the test. The overall duration of the experiment was 2 hours and 45 minutes.

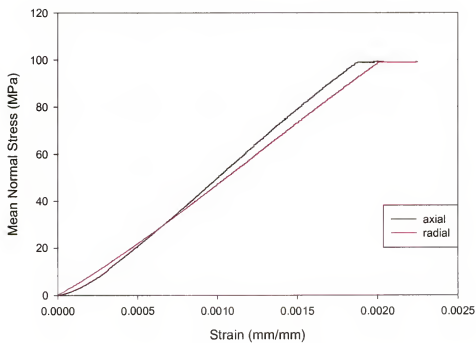


Figure 2-46: Hydrostatic compression phase, 100 MPa Kármán experiment

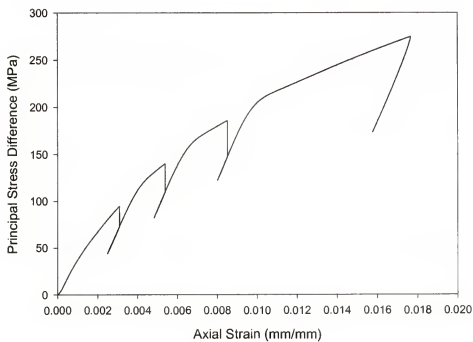


Figure 2-47: Deviatoric phase of 100 MPa Kármán experiment, axial strain

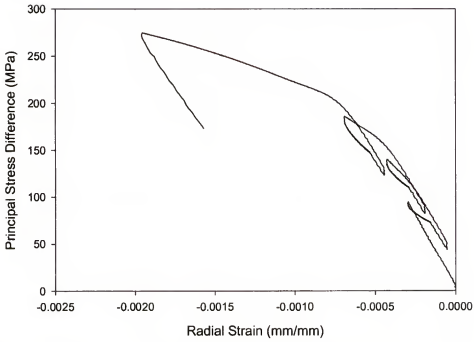


Figure 2-48: Deviatoric phase of 100 MPa Kármán experiment, radial strain

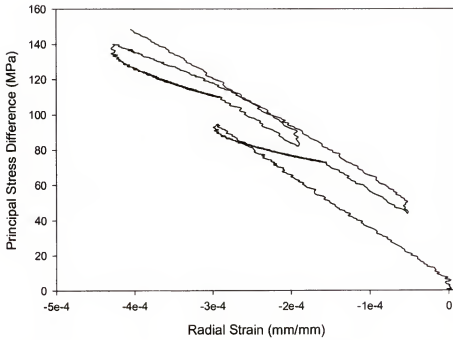


Figure 2-49: Deviatoric phase of 100 MPa Kármán experiment, radial strain first 2 cycles

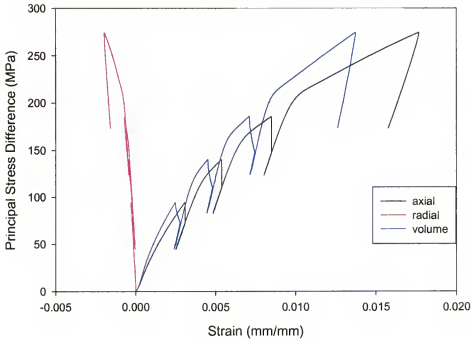


Figure 2-50: Deviatoric phase of 100 MPa Kármán experiment, all strains

### 2.13 375 MPa Experiment

The final experiment in our matrix was conducted at 375 MPa radial confinement (9902B017). Results of the monotonic hydrostatic compression phase are given in Figure 2-51. Relatively good correlation is seen in the axial and radial signals. The axial strain as a function of principal stress difference is presented in Figure 2-52. The quality of the axial data is quite good with little hysteresis in the unload-reload cycle. The signal again becomes noisy towards the end of the deviatoric loading as the specimen approached failure. The radial strain for the deviatoric shear phase is presented in Figure 2-53. Oscillatory behavior is again evident in the single creep cycle conducted. A detailed view of this creep-unload-reload cycle is presented in Figure 2-54. The response lag for the radial LVDT does not appear to be an issue in this experiment. All the signals are presented together in Figure 2-55. Again, the transition from compressibility to dilatancy only occurs



near failure. A peak principal stress difference of 617 MPa was achieved. The overall duration of the experiment was 3 hours and 3 minutes.

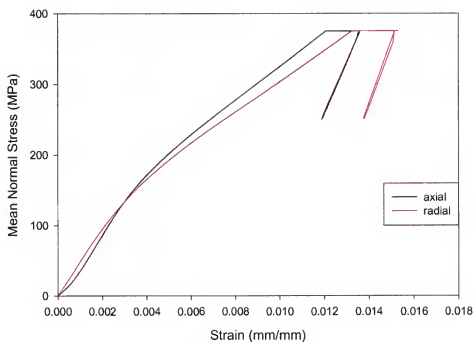


Figure 2-51: Hydrostatic compression phase, 375 MPa Kármán experiment

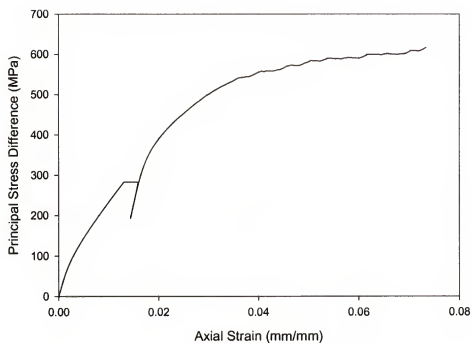


Figure 2-52: Deviatoric phase of 375 MPa Kármán experiment, axial strain

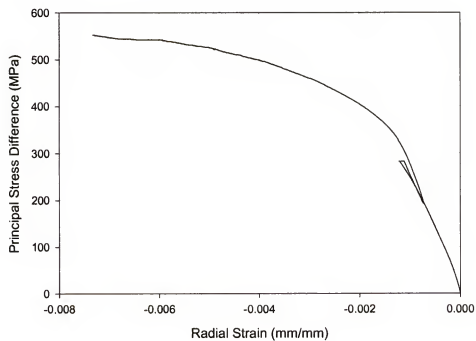


Figure 2-53: Deviatoric phase of 375 MPa Kármán experiment, radial strain

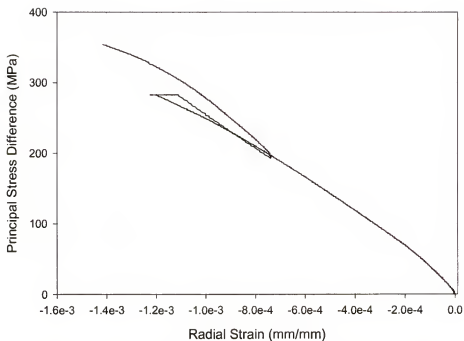


Figure 2-54: Deviatoric phase of 375 MPa Kármán experiment, radial strain first 2 cycles

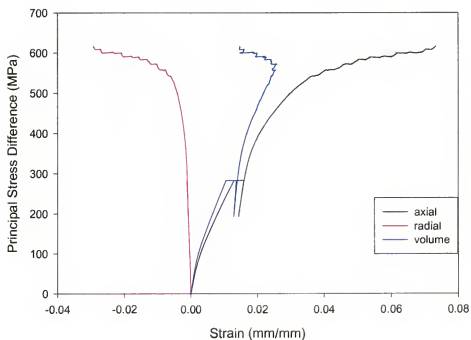


Figure 2-55: Deviatoric phase of 375 MPa Kármán experiment, all strains

## 2.14 Elastic Parameter Evaluation

The elastic parameters are taken from the slopes of the unload-reload cycles in the Kármán experiments. The Young's modulus,  $E$ , is determined from the slope of the axial strain vs. principal stress difference curve unload-reload cycles. By examining the recorded value of the principal stress difference, the commencement of the reload cycle was unmistakable. For this reason,  $E$  was determined from this portion of the cycle. In evaluating the slope, a least squares fit was made to the data. Figure 2-56 presents a typical result, in this case, the data was taken from the first unload-reload cycle of the 200 MPa deviatoric experiment. Generally, the  $r^2$  value for the least squares fit showed excellent correlation with the value of 0.998 presented here being quite typical. The term  $r^2$  as used here is a goodness of fit statistic such that:

$$r^2 = 1 - \frac{SSE}{SSM} \quad (2.4)$$

where  $SSE$  is the sum of the squared errors (residuals) and  $SSM$  is the sum of squares about the mean. Values for  $E$  from the different quasi-static experiments are presented as a function of mean normal stress in Figure 2-57. Visual inspection of the figure indicates a very clear and consistent trend in the data, with all the experiments in general agreement.

Values for the bulk modulus were taken from the slope of the unload-reload cycles of the volume strain versus mean normal stress curves, for both the hydro-static and deviatoric phases of the Kármán experiments. For consistency with the analysis of the Young's modulus,  $K$  values were also estimated from the reloading portion of each cycle. This proved to be somewhat problematic due to the response lag problems discussed previously for the radial deformeters on the reload cycles. Inspection of the data indicated that once the LVDTs actually started to respond, the slope of the data was nearly parallel to that of the down load cycles. Therefore,

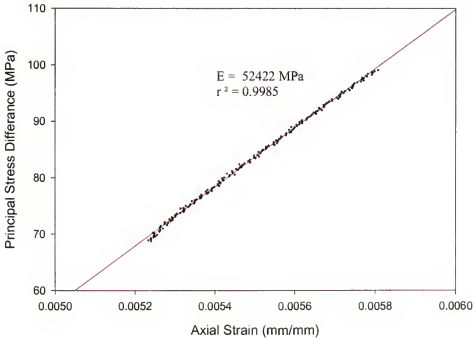


Figure 2-56: Least squares analysis for determination of Young's modulus

when necessary, the least squares fit to the data was taken starting at the point when the gauges appeared to be responding normally. For the evaluation of  $K$  from the hydrostatic compression data, since the axial signals were felt to be more reliable than the radial, only the axial signals were used in calculating the volume strain. This was possible due to the isotropic nature of the material (i.e.  $\varepsilon_v = 3\varepsilon_1$ ). Results of the data analysis for  $K$  are presented in Figure 2-58. With the exception of the values determined from the first test at 300 MPa confining pressure, the experiments appear to be in very good agreement. It was not expected that the results from this experiment would correlate well due to the problems observed in the radial measurements.

### 2.15 General Comments

Several conclusions/observations can be made at this point regarding the WES5000 quasi-static Kármán experiments. There was generally very good correlation between the axial and radial strain signals for the hydrostatic compression phase of the experiments. It is therefore quite reasonable to treat the material as

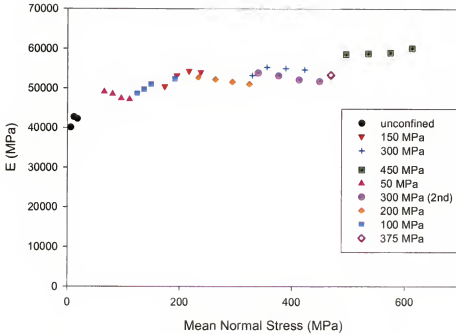


Figure 2-57: Young's modulus ( $E$ ) as a function of mean normal stress, experimental data

isotropic in nature. There were recurring problems with the radial strain signals, most likely tied to calibration issues and the mechanical linkage used to transmit radial deformation to the LVDTs. Generally, there is a higher degree of confidence in the axial signals recorded than the radial signals. There was a consistent transition in slope observed in the axial hydrostatic signals in the vicinity off 110 to 125 MPa confinement. According to Cargile [19], this can be attributed to compression cracking and breakdown of the mortar. This phenomena was not observed in the two tests conducted at 100 MPa and 50 MPa. The radial oscillatory behavior observed in the first two deviatoric shear phase creep cycles was consistent in all the experiments conducted. As was mentioned previously, Cristescu observed this behavior previously in highly porous rocks. Cristescu and Cazacu [20] have attempted to model this behavior in mortar using an elliptic yield function. In this study, insufficient data was collected in the lower principal stress difference regime to adequately map out this behavior. The deformation observed in the creep cycles,

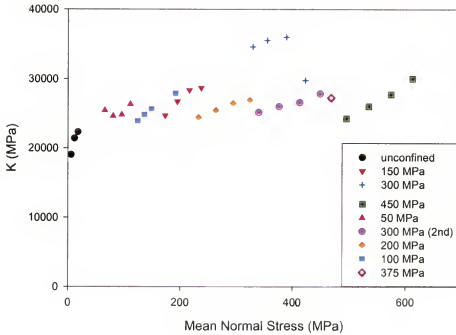


Figure 2-58: Bulk modulus ( $K$ ) as a function of mean normal stress, experimental data

as well as the effect of achieving stabilization in resolving the hysteresis issues in the unload-reloading cycles shows that there are strong time dependencies in the material. Figures 2-58 and 2-57 show that the elastic parameters are clearly pressure dependent. Finally, the peak value of principal stress difference observed in each experiment was plotted as a function of radial confining pressure. The results are presented in Figure 2-59. A very clear, remarkably consistent trend is evident in the data. Only the data point for the 100 MPa experiment appears somewhat low, however that experiment was not actually run to failure.

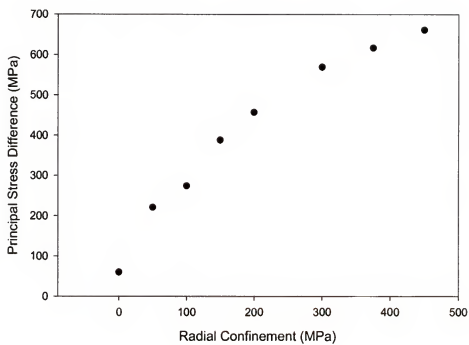


Figure 2-59: Peak principal stress difference as a function of radial confinement



## CHAPTER 3

### DYNAMIC MATERIAL CHARACTERIZATION

In Chapter 2, techniques for characterization of geologic materials at elevated pressures and quasi-static strain rates were discussed. Higher strain rate material characterization (i.e.  $10^1\text{s}^{-1}$  and higher) is generally carried out via bar impact experiments, or high-velocity plate impact experiments. Both experimental techniques will be reviewed in Section 3.1 of this chapter, as well as their applicability to geologic materials. In Section 3.2, issues regarding dynamic testing will be discussed and an experimental plan will be detailed for characterizing a mortar and the material under study, WES5000 under both unconfined and confined conditions using a Split Hopkinson Pressure Bar. The experimental set-up and test protocol will be presented in Section 3.3. The results of the tests conducted along with concluding remarks are given in Sections 3.4 and 3.5, respectively.

#### 3.1 Dynamic Characterization Techniques

##### 3.1.1 The Hopkinson Bar

Higher strain rate testing, on the order of  $10^1$  to  $10^4\text{ s}^{-1}$ , is usually accomplished via use of bar impact devices (see Figure 2–1). Bertram Hopkinson was among the first to perform laboratory investigations concerning the propagation of elastic waves in bars. In 1914, he reported on a device for measuring the pressure produced by explosive and impact loading [21]. His device consisted of a steel cylindrical bar suspended horizontally by wires so that it could swing in a pendulum fashion. One end of the bar was referred to as the “firing end”, which was subjected to explosive loading or ballistic impact, causing a compressive elastic stress pulse to be propagated down the bar. To the other end of the bar, Hopkinson attached small disks constructed of the same material as the bar. Hopkinson

referred to these disks as “time-pieces”, and they were held on to the end of the bar via either a wrung fit or magnetic attraction. As an elastic stress pulse propagated down the bar from the firing end, it would transmit into the time-piece and reflect off of the free surface as a tensile pulse. The time-piece would then separate from the bar once the reflected tensile pulse reached the bar interface. Momentum is trapped in the time-piece corresponding to a portion of the original stress pulse twice the length of the time-piece. By catching the time-piece in a ballistic pendulum the captured momentum could be determined, while the amplitude swing of the bar would indicate the momentum remaining in the bar. If the time-piece was of sufficient length to trap the momentum in its entirety, the bar would remain still upon separation. Thus, by varying the length of the time-piece, both the pulse magnitude and duration could be determined. However, the technique did not allow to determine the shape of the stress pulse. This apparatus came to be known as the Hopkinson pressure bar. To overcome this limitation, Davies, in 1948, devised an electrical capacitance technique for measuring stress pulses in a Hopkinson bar [22]. The use of electrical resistance strain gauges to measure the elastic stress pulse in bars did not become common until the late 1950’s and early 1960’s [23]. Still, Hopkinson pressure bar is utilized today in the measurement of explosive blast because the environment is too harsh for a conventional gauge to survive.

### 3.1.2 Compressive Split Hopkinson Pressure Bar Testing

The Split Hopkinson Pressure Bar (SHPB) is a modified Hopkinson pressure bar which was proposed by Kolsky [24]. For this reason, in the literature the SHPB is sometimes also referred to as a Kolsky bar. The apparatus setup is depicted in Figure 3-1. The SHPB consists of a short impactor (striker bar) and two long high-strength steel bars referred to as the incident and transmitter bars, respectively. The specimen is sandwiched between the incident and transmitter bar. The striker bar impacts the incident bar and produces a nearly square elastic compressive

stress pulse in the incident bar. The pulse propagates down the incident bar and at the specimen bar interface, a portion of the pulse is transmitted to the specimen, and a portion is reflected back due to an impedance mismatch. At the other end of the specimen, a portion of the wave is likewise transmitted to the “transmitter” bar and a portion reflected back into the specimen. Electrical strain gauges mounted at the mid point of the incident and transmitter bars record the passage and magnitude of the incident, reflected, and transmitted stress pulses. A brief summary of the SHPB equations for obtaining applied load, strain, and strain rate is given below.

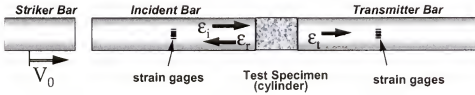


Figure 3-1: Split Hopkinson pressure bar

Consider the elastic impact of two circular cross-section bars as depicted in Figure 3-2. Let  $E$ ,  $A$ ,  $\rho$ ,  $L$ ,  $V$ , and  $C$  represent the bars respective Young's modulus, cross-sectional area, density, length, velocity, and acoustic wave speed. Bar-1 impacts bar-2 at its left end, thus  $V_1 > V_2$ . Assuming that the two bars remain in contact for a finite period of time  $\tau$ , then the load at the interface of each bar is the same, i.e.

$$P_1 = \sigma_1 A_1 = \sigma_2 A_2 = P_2 \quad (3.1)$$

Conservation of momentum yields:

$$-\rho_1 A_1 C_1 (V_1 - v) = -\rho_2 A_2 C_2 (v - V_2) \quad (3.2)$$

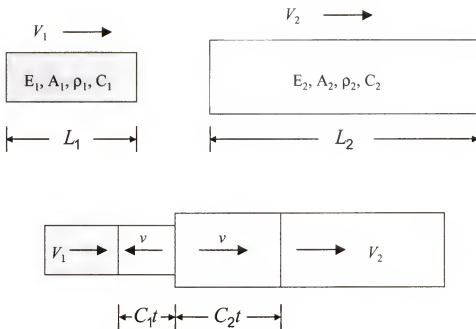


Figure 3-2: Elastic impact of two circular bars

where  $v$  therefore is:

$$v = \frac{\rho_1 A_1 C_1 V_1 + \rho_2 A_2 C_2 V_2}{\rho_1 A_1 C_1 + \rho_2 A_2 C_2}. \quad (3.3)$$

Hence, the stresses in the two bars may be expressed as:

$$\sigma_1 = -\rho_1 A_1 C_1 \frac{\rho_2 A_2 C_2 (V_1 - V_2)}{\rho_1 A_1 C_1 + \rho_2 A_2 C_2} \quad (3.4)$$

$$\sigma_2 = -\rho_2 A_2 C_2 \frac{\rho_1 A_1 C_1 (V_1 - V_2)}{\rho_1 A_1 C_1 + \rho_2 A_2 C_2} \quad (3.5)$$

If the two bars are of the same material and cross sectional area, then:

$$\rho_1 A_1 C_1 = \rho_2 A_2 C_2 = \rho A C_0 \quad (3.6)$$

and

$$\sigma_1 = \sigma_2 = \sigma. \quad (3.7)$$

The peak stress,  $\sigma$ , then is:

$$\sigma = \rho C_0 \frac{(V_1 - V_2)}{2} \quad (3.8)$$

Let bar-1 represent the striker and bar-2 the incident in a SHPB apparatus. Since the incident bar is always initially at rest,  $V_2 = 0$ , and the striker bar velocity may simply be denoted by  $V$ . Then, Equation 3.8 becomes

$$\sigma = \rho C_0 \frac{V}{2}. \quad (3.9)$$

The compressive pulse, of magnitude given by Equation 3.9, propagates back down the striker bar away from the impact point. The leading edge of the pulse reflects from the free surface at the back face of the striker bar,  $L_1$ , as a tensile pulse. Upon it's arrival back at the impact interface, the two bars separate, leaving a compressive pulse traveling in the incident bar, the length of the pulse being:

$$\tau = \frac{2L_1}{C_0}. \quad (3.10)$$

Note that the pulse length and magnitude is determined by the striker bar length and velocity respectively (Equations 3.9 and 3.10).

### Load and Strain Analysis

Figure 3-3 shows an expanded view of a material specimen sandwiched between the incident and transmitted bar for a SHPB compression test. Here the subscripts 1 and 2 are used to denote the incident and transmitted bar ends, respectively. Let  $\varepsilon_i$ ,  $\varepsilon_r$ , and  $\varepsilon_t$  be the incident, reflected, and transmitted strains

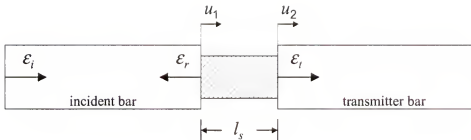


Figure 3-3: Split Hopkinson pressure bar expanded view

respectively, while  $u_1$  and  $u_2$  denote the displacements of the ends of the incident and transmitted bars, respectively. Under the assumption that wave propagation in the bars is one dimensional and that the behavior is elastic, it follows that:

$$\frac{\partial^2 u}{\partial t^2} = C_0^2 \frac{\partial^2 u}{\partial x^2} \quad (3.11)$$

where  $t \equiv$  time,  $x \equiv$  the 1-D Lagrangian coordinate, and  $C_0$  is the elastic wave speed in the bar defined as:

$$C_0 = \frac{E}{\rho}. \quad (3.12)$$

The classical d'Alembert solution to this 1-D wave equation is:

$$u(x, t) = f(x - C_0 t) + F(x + C_0 t) \quad (3.13)$$

where  $f$  and  $F$  are arbitrary functions depending on the initial conditions.

The function  $f$  represents a wave travelling in the positive  $x$  direction (to the right in our frame of reference), while  $F$  corresponds to a wave traveling in the opposite direction. Thus,  $f$  and  $F$  may be thought of as the incident and reflected waves.

Equation 3.13 may then be written:

$$u(x, t) = f(x - C_0 t) + F(x + C_0 t) = u_i + u_r. \quad (3.14)$$

Since the strain is :

$$\varepsilon = \frac{\partial u}{\partial x} \quad (3.15)$$

Substitution into Equation 3.14 yields:

$$\frac{\partial u(x, t)}{\partial x} = \frac{\partial}{\partial x} f(x - C_0 t) + \frac{\partial}{\partial x} F(x + C_0 t) = \varepsilon_i + \varepsilon_r \quad (3.16)$$

where  $\varepsilon_i$  and  $\varepsilon_r$  represent the incident and reflected strains respectively.

The deflection of the incident and transmitter bar interfaces are given by:

$$u_1 = \int_0^t C_0 \varepsilon_1 dt \quad (3.17)$$

and

$$u_2 = \int_0^t C_0 \varepsilon_2 dt \quad (3.18)$$

Assuming stresses, strains, and loads are positive in compression, the Equations 3.17 and 3.18 may be written in terms of the incident ( $\varepsilon_i$ ), reflected ( $\varepsilon_r$ ), and transmitted ( $\varepsilon_t$ ) strains.

$$u_1 = C_0 \int_0^t (\varepsilon_i + \varepsilon_r) dt \quad (3.19)$$

$$u_2 = C_0 \int_0^t (\varepsilon_t) dt \quad (3.20)$$

The average strain in the specimen is:

$$\varepsilon_s = \frac{u_1 - u_2}{l_s} \quad (3.21)$$

where  $l_s$  is the specimen length. Substitution of Equations 3.19 and 3.20 into Equation 3.21 yields:

$$\varepsilon_s = \frac{C_0}{l_s} \int_0^t (\varepsilon_i + \varepsilon_r - \varepsilon_t) dt \quad (3.22)$$

Next, using Hooke's law, the load on each end of the specimen is obtained:

$$P_1 = EA(\varepsilon_i + \varepsilon_r) \quad (3.23)$$

and

$$P_2 = EA\varepsilon_t \quad (3.24)$$

where  $E$  and  $A$  are the Young's modulus and cross-sectional area of the SHPB, respectively. The average force in the specimen then becomes:

$$P_{av} = \frac{EA}{2} (\varepsilon_i + \varepsilon_r + \varepsilon_t) \quad (3.25)$$

A general assumption is that the specimen is in a state of uniform stress or in other words, the loads at the ends of the specimen are equal. It follows that:

$$\varepsilon_i + \varepsilon_r = \varepsilon_t \quad (3.26)$$

and

$$\varepsilon_s = \frac{C_0}{l_s} \int_0^t (\varepsilon_t - \varepsilon_r - \varepsilon_r - \varepsilon_t) dt \quad (3.27)$$

In summary, for a direct compression test, the average stress, average strain, and average strain rate in the specimen are given by the relations:

$$\varepsilon_s = \frac{2C_0}{L_s} \int_0^t \varepsilon_r dt \quad (3.28)$$

$$\sigma_s = E \frac{A_b}{A_s} \varepsilon_t \quad (3.29)$$



$$\dot{\varepsilon}_s = \frac{2C_0}{L_s} \varepsilon_r \quad (3.30)$$

where the subscripts  $r$  and  $t$  refer to the reflected and transmitted signals respectively, while  $s$  is in reference to the specimen and  $b$  the bar.  $E$  is the elastic modulus of the bar,  $C_0$  is the elastic wave speed in the bar,  $L_s$  is the length of the specimen, and  $A$  refers to cross sectional area. In general, the Equations 3.28 through 3.30 represent the basic features of the SHPB, the specimen stress is proportional to the transmitted strain, the strain rate is proportional to the reflected strain, and the specimen strain is proportional to the integral of the reflected strain. It is important to note that these expressions represent average values and are calculated from uniaxial stress-state assumptions in the specimen and elastic behavior in the bars.

### 3.1.3 Dynamic Tensile Testing

Tensile testing data, either under quasi-static or dynamic conditions is usually obtained by conducting a splitting tension test, also referred to as a Brazilian test. In fact, the Brazilian test is the only method recognized by the ASTM for determining quasi-static concrete tensile strength. The required geometry and testing procedure is detailed in ASTM C496-96. Figure 3-4 illustrates the testing procedure. A cylindrical concrete specimen is subjected to a diametral compressive force along its longitudinal axis. The load is applied at a rate within prescribed limits until specimen failure occurs. The state of stress within the specimen is characterized by high compressive forces at the point of contact between the specimen and the platens of the load frame, and a uniform tensile zone towards the center. According to Neville [15], this tension zone runs along approximately 75% of the diameter of the specimen. Although the compressive forces are of far greater magnitude, due to the fact that concrete is much weaker in tension than in compression, the specimen fails in tension before the compressive loads reach a

critical value. Figure 3-5 illustrates the stress distribution within the specimen. At failure, the magnitude of the tension force is given by:

$$\sigma_y = \frac{2P}{\pi LD} \quad (3.31)$$

Ross [25] was the first to conduct a dynamic Brazilian test in a SHPB. Making the assumption that the maximum load sustained in the specimen is equal to the measured transmitted load, the dynamic tensile strength is:

$$\sigma_{max} = \frac{2P}{\pi LD} = \frac{2R_b^2 \sigma_T}{LD} \quad (3.32)$$

where  $\sigma_{max}$  is the maximum sustained tensile load,  $R_b$  is the bar radius,  $L$  is the specimen length, and  $D$  is the specimen diameter. The average strain rate is determined from the slope of the transmitted stress-time signal:

$$\dot{\epsilon}_{avg} = \frac{\Delta\sigma}{E_c \Delta t} \quad (3.33)$$

where:  $\Delta\sigma$  is the change in stress over time interval  $\Delta t$  and  $E_c$  is the concrete elastic modulus obtained from static strength tests. Finite element analysis was used to verify that the stress distribution in the Brazilian sample under dynamic loading is nearly equivalent to that in the static case [26, 27, 28].

Classical Hopkinson pressure bar could also be used to generate tensile data on concrete. The concrete sample is cemented to the end of the bar opposite the firing end. The load is then applied to the Hopkinson bar, usually with a striker bar but sometimes through direct application of an explosive charge to the firing end. A compressive pulse travels down the bar, and at the bar-specimen interface, a portion of the pulse is reflected back into the bar and a portion transmitted into the specimen. At the free surface of the specimen, the compressive pulse is reflected back as a tensile one. If the magnitude of the resulting tensile pulse is greater than the dynamic strength of the specimen, tensile failure, referred to as spall, will

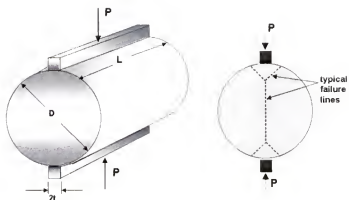


Figure 3-4: Brazilian test

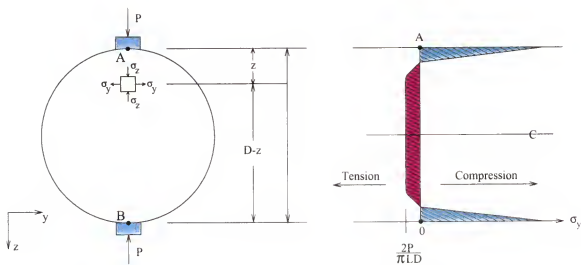


Figure 3-5: Stresses and stress distribution for the Brazilian test

occur trapping the momentum from the portion of the pulse exceeding the dynamic tensile strength in the spalled off section. Direct application of strain gauges to the specimen allows for measurement of both the initial compressive pulse and the reflected pulse corresponding to the dynamic tensile strength. One advantage to this technique is that the specimen is under true uniaxial tension. However, the initial compressive load may also impart some level of damage into the material. Recent applications of the Hopkinson bar for dynamic tensile testing of brittle materials has been reported by Díaz-Rubio et al. [29].

#### 3.1.4 Confined Dynamic Testing

All of the techniques discussed so far have been used for dynamic testing under unconfined conditions. As has been discussed previously, the behavior of most geologic materials is highly sensitive to hydrostatic pressure. It is therefore desirable to gather dynamic data under confined conditions. One method of achieving confining pressure in a dynamic SHPB test is by attempting to limit the lateral expansion of the specimen. Lankford et al. [30] Walker et al. [31], and Chen and Ravichandran [32] have reported on efforts to apply autofrettaged (shrink fit) rings to ceramic specimens. Very high confining pressures were thus achieved at strain rates in excess of  $1000 \text{ s}^{-1}$ . The disadvantages of this technique include the difficulty of specimen fabrication and the impossibility of maintaining a constant pressure throughout the experiment. While confining pressure as a function of time could be inferred by instrumenting the rings, it is generally difficult to accurately establish what the initial state of confinement was. An alternative method proposed by Bhushan and Jahsman [33] makes use of a massive steel collar to confine the specimen. Though specimen preparation appears easier than in the autofrettaged approach, due to tight tolerances, the SHPB specimens had to be kept in a freezer prior to insertion in the collar. Analysis is performed under the assumption of uniaxial strain conditions. Once again, the confining pressure on

the specimen is not constant throughout the experiment and pressure levels must be inferred. Note that the influence of frictional forces would also be very difficult to quantify in both techniques. An alternative method was proposed by Malvern [34], who coupled a hydrostatic confinement cell to a SHPB. The confinement cell, shown in Figure 3-6 coupled with an axial preload device is capable of placing the specimen under true hydrostatic confinement prior to application of the dynamic axial load. Confining pressures were held fairly constant due to internal accumulator action provided by air trapped in the cell. This technique is quite close to a dynamic Kármán test. The primary disadvantage of this technique is that the range of confining pressures achievable with this cell is relatively low (3000 psi).

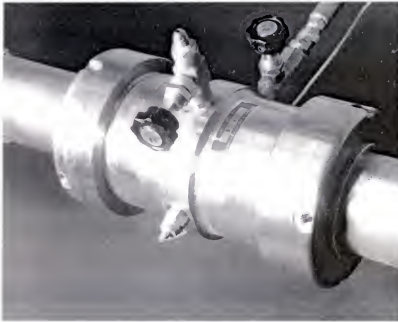


Figure 3-6: Hydrostatic confinement cell

### 3.1.5 Plate Impact Experiments

In a plate impact experiment, a thin disk sample of concrete is fired from a gas gun and normally impacted into a hard steel target plate. Elastic response of the steel plate and uniaxial strain conditions in the concrete specimen are

assumed. The transient response of the back face of the plate is recorded using a VISAR [35] laser interferometer. Knowing the density and acoustic velocity of the target material, it is possible to calculate the average stress at the specimen-target interface as  $\sigma = \frac{1}{2}\rho c V_{fs}$ , where  $\sigma$ ,  $V_{fs}$ ,  $\rho$ , and  $c$  are the average longitudinal stress at the specimen/target interface, particle velocity at the rear surface of the target, mass density and longitudinal elastic wave speed of the target material. These flyer plate experiments have been demonstrated to yield constitutive data at strain rates from approximately  $10^3 s^{-1}$  to  $10^5 s^{-1}$  under confining pressures on the order of 1 to 1.5 GPa [36]. Kipp et al. [37] reported on a series of reverse ballistic flying plate experiments in which WES5000 was utilized. In a reverse ballistic experiment, the concrete material is the target plate. Unfortunately, since specimen strains are not directly measured in the flyer plate experiment, it is not possible to directly develop a stress strain model based on results of such tests. Flyer plate data can thus serve only for validation purposes. When using the VISAR technique on a heterogenous material like concrete, there appear instrumentation issues as well. Because the VISAR measures only the free surface response in a highly localized area, either the average response from a number of experiments must be utilized, or several VISAR employed in a single experiment to ensure that the measurement is representative of the macroscopic level material properties and not of local aggregates or other local defects.

### 3.2 Dynamic Experimental Program

In order to dynamically characterize the WES5000 concrete, a series of Split Hopkinson Pressure Bar (SHPB) experiments were conducted under both confined and unconfined conditions. For comparison purposes, a second mortar material was also characterized. The experimental matrix called for a total of three different dynamic loading rates at four different confining conditions. The experimental matrix is given in Table 3-1.

Table 3-1: Dynamic Kármán test matrix

Confined dynamic Kármán tests								
	Confining pressure							
	0		$L_p$		$M_p$		$H_p$	
Striker bar velocity	C	M	C	M	C	M	C	M
Quasi – static	3	3	3	3	3	3	3	3
$L_v$	3	3	3	3	3	3	3	3
$M_v$	3	3	3	3	3	3	3	3
$H_v$	3	3	3	3	3	3	3	3
Subtotal	24		24		24		24	

A total of 96 experiments are included in this matrix. The quasi-static loading conditions are intended to provide a baseline characterization for comparison purposes. The confining conditions  $L_p$ ,  $M_p$ , and  $H_p$  refer to low, medium and high levels of confining pressure respectively. Likewise, in the striker bar velocity column,  $L_v$ ,  $M_v$ , and  $H_v$  stands for low, medium, and high velocities. The proposed matrix represents a large number of experiments. It was felt that this was required due to the inherent variability of the concrete specimens as well as to the novel nature of the experiments. The duplicate conditions also allowed to check that the data generated are representative of the material behavior.

### 3.3 Experimental Setup

#### 3.3.1 SHPB

The issue of ensuring that tests were conducted with specimens that can be assumed to be homogeneous (representative volume elements) was discussed earlier in this chapter. It was pointed out that for WES5000, a minimum SHPB diameter of approximately 40mm was required. The tests were carried out at the Material Properties Laboratory at the University of Florida's Graduate Engineering Research Center (GERC) using a 76.2mm diameter SHPB. The GERC's SHPB is ideally suited for this effort and represents one of only a few devices of its size available in the world. The incident and transmitter bars are each 3.10m (122in) in length. Two striker bars of 0.762m (30in) and 1m (40in) are available. They are

capable of generating a loading pulse of approximately  $300\mu s$  and  $400\mu s$  duration, respectively. The incident and transmitter pressure bars, as well as the strikers are fabricated from ETD-150 steel, whose density, bar-wave speed, and Poisson's ratio are  $7,650\text{ kg/m}^3$ ,  $5,150\text{ m/s}$  and 0.32, respectively. The strikers are launched with a gas gun, fabricated by Terra-Tek Systems, Inc. The firing chamber of the gun has a maximum chamber pressure of 4.1 MPa ( 2000 psi). The propellant gas is furnished by a nitrogen bottle. An optical device for measuring striker bar velocity is positioned at the mouth of the gas gun barrel. A full strain-gauged bridge is permanently mounted at the midpoint of each pressure bar. Strain gauge conditioning is provided via Measurements Group model 2311 strain gauge conditioning amplifiers with a bandwidth of 1.25 MHz. Data signals are recorded by a Nicolet 4094 digital oscilloscope capable of recording at  $0.5\text{ }\mu s$  intervals. The GERC's SHPB is shown in Figure 3-7.



Figure 3-7: University of Florida GERC SHPB



Radial confinement may be applied to the material sample using a confining cell originally developed by Malvern [34]. The confinement cell is constructed of 17-4 PH Stainless Steel (Condition A) with a maximum operating pressure of 20.7 MPa (3000 psi). The design includes a factor of safety of 10. The cell contains 4 access ports, including one which accommodates a pressure gauge. A cut away drawing of the pressure cell is shown in Figure 3-8

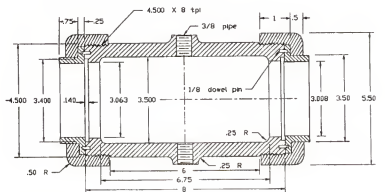


Figure 3-8: Cut away view of GERC confinement cell (all dimensions in inches)

In order to measure the pressure in the confining cell, a Kulite model HKM-375-5000-A transducer, with a natural frequency of 1.12 MHz, was selected for the study. To achieve a triaxial pre-test load on the test specimens, a hand operated hydraulic load cell was utilized. Figure 3-9 shows the load cell in position at the far end of the transmitter bar. In order to restrain the incident bar, a “bar restraint” was designed and positioned near the mouth of the gas gun. The device consisted of a steel plate with a counter-sunk hole cut into it (see Figure 3-10). A small bar or “stop” was machined from ETD-150 steel to fit into the counter-sunk hole. The smaller inner diameter of the stop matched the outer diameter of both the striker and incident bars. Figures 3-11 and 3-12 show the stop and the end restraint with the stop in place, respectively.



Figure 3-9: Hydraulic load cell for SHPB

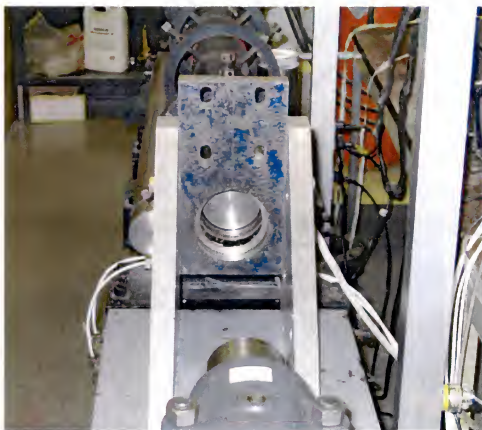


Figure 3-10: End restraint for SHPB



Figure 3-11: Bar stop for SHPB

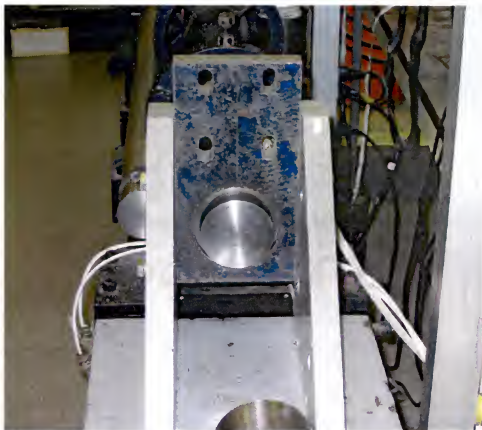


Figure 3-12: End restraint with stop in place for SHPB

### 3.3.2 Quasi-Static Setup

For the baseline quasi-static characterization, an MTS 815 rock mechanics system load frame was utilized. Since the load frame did not possess a confinement cell, a means was required to adapt the SHPB confinement cell to a conventional hydraulic load frame. Two attachments were designed for the MTS machine, essentially consisting of high-strength tool steel bars with special attachments for connecting to the upper and lower platens of the load frame. The adaptors are shown in position on the MTS machine with the SHPB cell attached in Figure 3-13.

### 3.3.3 Specimen Design/Preparation

According to Gray [38], radial and longitudinal inertia errors, as well as friction effects can be reduced by choosing a sample size that minimizes the areal mismatch between the sample and the bar diameter, and maintains a sample  $L/D$  ratio of 0.5 to 1.0. It is also desirable from an homogeneity standpoint to have an equal number of aggregates across both the specimen length and diameter. For these reasons, a nominal  $L/D$  ratio of 1-to-1 was selected. The WES5000 samples were cored from the same material batch utilized in the quasi-static experiments of Chapter 2. The cores taken were nominally 75 mm in diameter and were cut into lengths of approximately 76 mm. The end faces on each sample were then ground to assure parallelism. The diameter and length of each specimen was measured with a set of digital calipers and weighed on a digital balance. The samples utilized were screened according to end face parallelism, roundness, and obvious large surface flaws. Due to the porous nature of WES5000, surface preparation was necessary for both strain gage application and to ensure that the latex membranes utilized to isolate the specimens from the fluid in the confined experiments were not forced into pores or voids causing punctures. Preparing the samples was a multi-step process. The specimen was first probed with a pick to



Figure 3-13: Load frame modified for confined test

identify and open larger surface voids. These voids were then filled with a gypsum paste. The use of a gypsum past was recommended by Waterways Experimental Station and it was believed it would not influence the strength properties of the material. The paste was then sanded down even with the surface of the specimen and excess dust removed with a damp cloth. Prior to strain gage instrumentation, an initial application of epoxy is required. This initial application is sanded down smooth and the specimen again cleaned and neutralized. A second application of epoxy is then applied for actual gage application. However, trial showed that the epoxy tended to be absorbed into the gypsum and upon drying resulted in depressions in the specimen unsuitable for gage application. In order to avoid this, an intermediate layer of cement epoxy was applied. This was then sanded down smooth, cleaned as called for, and the gage epoxy applied. It was felt that this would not affect the overall material behavior. Following strain gauge application, clamps were placed on the specimens to apply a uniform pressure on the gauge. The specimens were then allowed to cure for several days in a warm area prior to conducting the tests. For comparison purposes, mortar was also tested. This material was formulated and prepared for the study by the Air Force Research Laboratory Materials Directorate's Pavement Division at Tyndall Air Force Base. Samples of this material were cast into molds on 8 May 1998. Mixture properties for the mortar are provided in Table 3-2.

Table 3-2: Ingredients and mixture proportions for mortar

Item	Mixture proportions, saturated surface-dry
Type I Portland cement	450g
Sand, sieve #4	1620g
WRDA-19 0.5%	3.7g
"F" fly ash	297g
Water, w/c = 0.55	411g

Measurements Group precision strain gauges were utilized in the experiments. Gauge type EA-06-10CBE-120, with a gauge length of one-inch was selected for the WES5000 to average out the local aggregate effects, while type EA-06-0500BH-120, with a gauge length of 0.5 inch was selected for the mortar because the mix doesn't contain any aggregates. Two axial and two radial gauges were applied to each specimen. The application of both axial and radial gauges allowed measurement of volume changes under dynamic conditions. Figures 3-14 and 3-15 show instrumented WES5000 and a mortar samples.



Figure 3-14: Strain gauges applied to WES5000 SHPB specimen

### 3.3.4 Experimental Protocol

In this section, the protocol observed for the confined SHPB experiments is presented. First, special care is required to ensure that the striker bar is fully retracted into the barrel of the gas gun. Next, the bar stop is inserted into the restraint and the incident bar moved towards the stop until the two are in contact. The UF/GERC confining cell, along with the locking flange o-ring and collar are



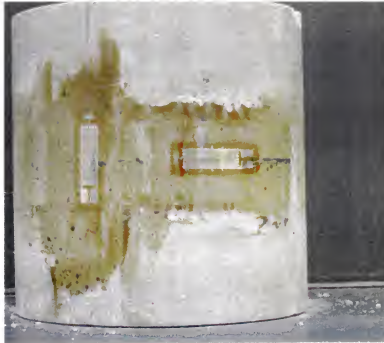


Figure 3-15: Mortar SHPB specimen with strain gauges applied

then positioned onto the transmitter bar. Proper orientation is required in that the incident side flange is of slightly greater inner diameter to allow feed-through of the instrumentation wires, and the respective flanges are matched to specific sides of the cell. Next, thin ETD-150 steel disks of the same outer diameter as the pressure bars are placed on both the incident and transmitter faces and held in place with a piece of electrical tape. A thin layer of grease is applied to the interface to assure good contact is achieved. The disks serve to protect the incident and transmitter bar faces from any damage due to contact with the hard aggregate. The disks were polished after each test to remove any burrs or scratches. A latex membrane is then placed over the transmitter bar and secured at one end with electrical tape. The latex membrane is to be utilized as a barrier between the specimen and the confining fluid. Figure 3-16 shows this first stage of experimental setup.

The specimen is next placed between the incident and transmitter bars. To minimize frictional effects, a thin layer of grease is applied to the face of the disks covering the bar faces. The specimen is held in place with one wrap of electrical



Figure 3-16: Setup: cell in place on SHPB

tape at each end (Figure 3-17). The strain gauges are then connected to electrical leads made of 34-gage solid core copper wire. A very fine wire was necessary so that it would pass between the incident side flange and the pressure bar. Special care was required so as not to tangle or kink the very fine wires. The wires are led down the bar and held in place with a strip of electrical tape. A strip of tape was also placed over each gauge (Figure 3-18). Finally, the latex membrane is pulled over the specimen and secured in place with a piece of electrical tape (Figure 3-19).

The confinement cell is then carefully slid into position over the specimen. Due to close tolerances, a water based lubricant is first applied to the membrane (Figure 3-20). The o-rings and flange are then placed in position. Locking collars are threaded onto the cell and tightened with a set of specially designed spanner wrenches. The pressure applied to the flange, and subsequently the o-rings, by the locking collar causes the o-rings to seal around the SHPB. The pressure gauge may now be threaded into the instrumentation port and securely tightened. Pressurization is applied to the confining cell via a 20.7 MPa (3000 psi) capacity hydraulic accumulator. The accumulator is next filled with water and connected



Figure 3-17: Setup: specimen in place and secured

to the confinement cell through an opening in the SHPB support structure (Figure 3-21). The pressurization fluid selected was water because the latex membrane would have degraded through contact with normal petroleum based hydraulic fluid. Water is forced into the confinement cell when the accumulator is pressurized. The air trapped in the cell was expected to provide internal accumulator action for damping of the pressure during the actual test [34]. The external accumulator was not expected to provide any pressure damping since its response time was believed far too slow considering that the duration of the experiment was on the order of a few hundred micro-seconds. It did prove however to be an excellent means of maintaining a nearly constant pressure prior to launching the striker bar as well as compensating for minor leaks prior to testing. The accumulator is charged using a high pressure hose connected to a high pressure nitrogen bottle. Pressurization of the system is a multi-step process. A small axial load is applied using the



Figure 3-18: Setup: electrical leads connected

hydraulic hand pump, then the accumulator is pressurized via the nitrogen tank to the same level. The axial load is monitored with a pressure gauge (Kulite HKS-11-375-2000 SG) attached to the pump and connected to a digital readout. The cell pressure was monitored by a pressure gauge, whose output was read on one of the oscilloscopes. It was necessary to apply the axial load first to assure that the radial pressure did not force the bars apart, causing the specimen to lose contact with the SHPB. By continuing the step-wise process of increasing the axial load, then matching the radial pressure, the specimen could be safely brought up to the desired hydrostatic load. Once the specimen is under the desired level of hydrostatic confinement, the strain gauges are balanced and the instrumentation set to record. The gas gun could then be charged to the desired pressure and fired. Data was recorded on the Nicolet 4094 B oscilloscopes.



Figure 3-19: Setup: latex membrane in place and secured

Setup for the quasi-static experiments utilizing the MTS machine was almost identical. The only exception is that the step wise hydrostatic loading was done by programming the MTS machine . Once the desired level of hydrostatic confinement was achieved, it was kept constant and the axial load was applied via the platens of MTS machine. Data was recorded with a computer based data acquisition system.

### 3.4 Experimental Results

#### 3.4.1 Quasi-Static Baseline

Characterization experiments were conducted on mortar and WES5000 samples under quasi-static loadings conditions (strain rate  $\approx 10^{-6}$ ) for four different confining pressures. The specimen sizes were of the same dimensions as those used for the SHPB tests. Each specimen was strain gauged both axially and radially (two each) so that the volumetric response could be measured. Each experiment was given a unique designator, either QSMCXX, QSMUXX, QSCCXX.

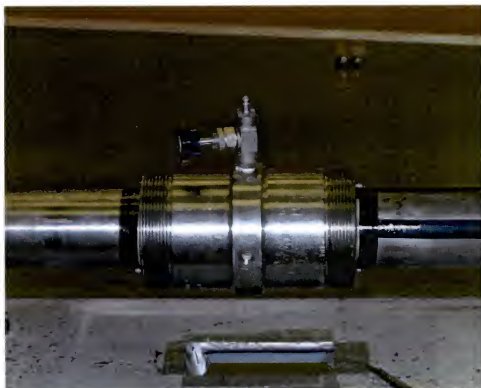


Figure 3-20: Setup: confinement cell in position over specimen

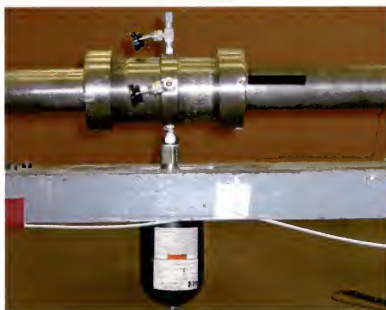


Figure 3-21: Setup: accumulator and end caps connected

or QSCUXX, where QSMC, QSMU, QSCC and QSCU refer to quasi-static mortar confined, quasi-static mortar unconfined, quasi-static concrete confined and quasi-static concrete unconfined respectively. The XX is a unique numerical designator. The following two sections summarize the quasi-static results for mortar and WES5000, respectively.

### Mortar

A total of 13 quasi-static experiments were conducted on mortar samples under both confined and unconfined conditions. The confining pressures corresponding to  $L_p$ ,  $M_p$ , and  $H_p$  in Table 3-1 are 1.72 MPa (250 psi), 3.45 MPa (500 psi) and 6.89 MPa (1000 psi) respectively. Nominal loading rate was 133 Newtons/s (30  $lb_f/s$ ). The experiment identifier, confining condition under which they were run, and the peak principal stress difference are summarized in Table 3-3.

Table 3-3: Quasi-static mortar results

Experiment #	Confining pressure (MPa)	$q_{max}$ (MPa)	Comments
QSMU01	-	49.5	
QSMU02	-	50.0	
QSMU03	-	56.0	unload-creep-reload cycles
QSMU04	-	54.5	unload-creep-reload cycles
QSMC01	3.45	70.2	
QSMC02	3.45	63.1	
QSMC03	3.45	63.8	
QSMC04	3.45	69.0	
QSMC05	1.72	63.6	
QSMC06	1.72	59.0	
QSMC07	6.89	78.1	
QSMC08	6.89	64.0	membrane failure
QSMC09	6.89	81.6	

Figures 3-22 through 3-25 show the principal stress difference versus strain curves for the various loading conditions. Only one representative curve is shown for each condition. The plots show initial compressibility, followed by a gradual transition to dilatancy. The dilatancy threshold depends on the confinement, the

higher the confinement, the closer is the dilatancy threshold to the peak stress reached in the test. Representative principal stress difference vs. volume strain curves are presented for the four levels of confinement in Figure 3-26. Here the effect of confinement on strength and dilatancy can be clearly seen. The right axis of Figure 3-26 is expressed in terms of Confinement Increase Factor, or CIF. The CIF is defined as the principal stress difference normalized by the unconfined compressive strength. Even at the relatively low confinement level of 6.89 MPa, a strength enhancement of almost 1.5 times is observed. The average values of the peak stresses (strength) are shown in Table 3-4 and a plot of peak stresses versus confinement pressure is shown in Figure 3-27. Note that over the confining pressure range investigated, the relationship between strength and confinement pressure is nearly linear.

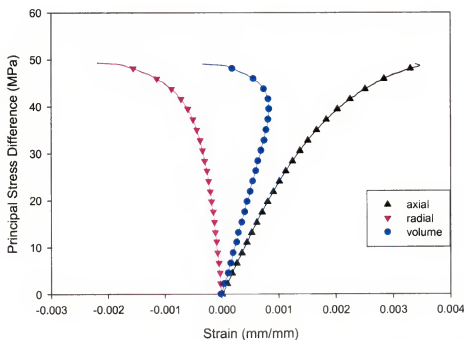


Figure 3-22: Quasi-static mortar unconfined compression experiment - QSMU01



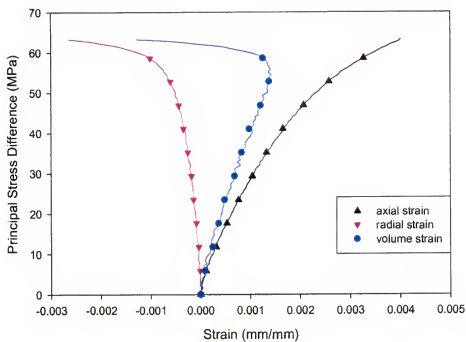


Figure 3-23: Quasi-static mortar confined (QSMC05) - 1.72 MPa confinement

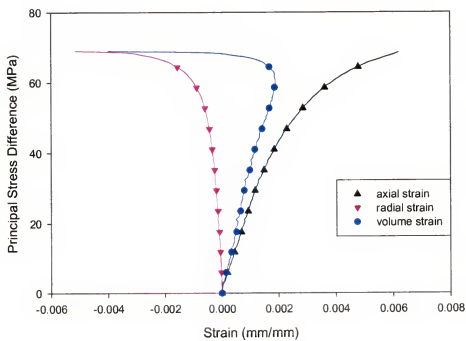


Figure 3-24: Quasi-static mortar confined (QSMC04) - 3.45 MPa confinement

Table 3-4: Average peak principal stress difference at failure for mortar.

Confining pressure (MPa)	0	1.72	3.45	6.89
Avg. peak principal stress diff. (MPa)	52.5	61.3	66.5	79.85

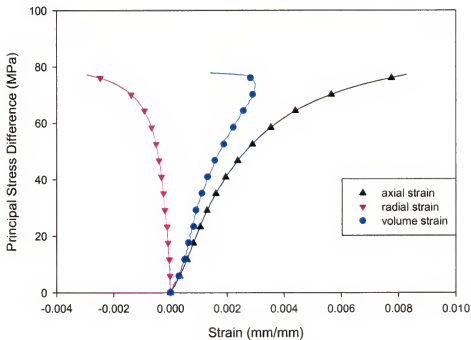


Figure 3-25: Quasi-static mortar confined (QSMC07) - 6.89 MPa confinement

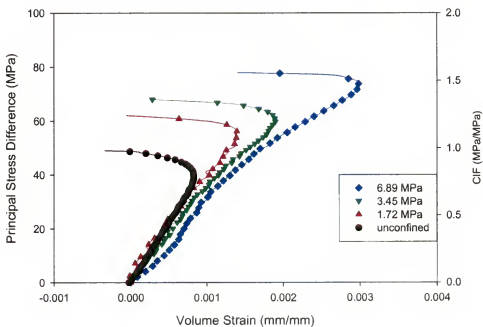


Figure 3-26: Confinement effect on quasi-static mortar behavior

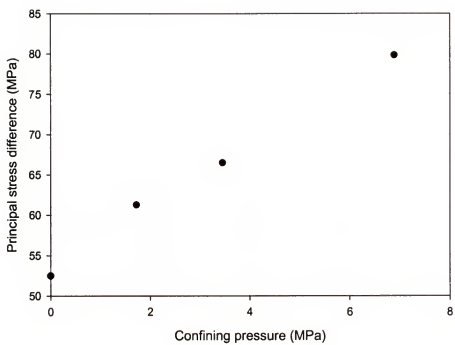


Figure 3-27: Peak principal stress difference at failure as a function of confinement for mortar

### WES5000

A total of 14 quasi-static experiments were conducted on WES5000 samples under both confined and unconfined conditions. The confining pressures were the same as those utilized in the quasi-static mortar experiments. The nominal loading rate was 133 Newtons/s (30  $lb_f/s$ ). The experiment identifiers, confining conditions under which they were run, and the peak principal stress differences are summarized in Table 3-5.

Table 3-5: Quasi-static WES5000 results

Experiment #	Confining pressure (MPa)	$q_{max}$ (MPa)	Comments
QSCU01	-	62.9	
QSCU02	-	64.9	
QSCC01	3.45	107.7	
QSCC02	3.45	100.5	
QSCC03	3.45	100.9	
QSCC04	3.45	112.4	
QSCC05	6.89	68.5	membrane failure
QSCC06	6.89	120.7	
QSCC07	6.89	41.0	membrane failure
QSCC08	6.89	75.3	membrane failure
QSCC09	1.72	52.5	membrane failure
QSCC10	1.72	48.6	membrane failure
QSCC11	1.72	86.7	
QSCC12	1.72	91.7	

Performing these experiments with WES5000 proved to be very problematic. The one successful experiment at 6.89 MPa (1000 psi) required 68 minutes to complete. In Chapter 2, it was briefly discussed that because of the heterogeneous nature of WES5000, under high confinement, strain gage measurements are nearly impossible. The same problems were encountered during testing under very low confining pressures. As the experiment progressed, and the axial load on the specimen increased, the likelihood of a membrane failure and gage failure dramatically increased. Due to the tight tolerances of the GERC confinement

cell, the use of multiple membranes and layers of putty surrounding the specimen (the technique utilized by WES and discussed in Chapter 2) was not an option. However, the correlation between the successful experiments was quite good. Figures 3-28 through 3-31 present the principal stress difference versus strain curves for the various loading conditions. Only one representative plot is shown for each condition. The data generated at the GERC is consistent with the data generated at WES for unconfined conditions and confining pressures below 50 MPa (see Chapter 2). The curves show initial compaction, followed by a gradual transition to dilatancy with the transition to dilatancy moving closer to the failure strength as confinement is increased. Representative principal stress difference vs. volume strain curves are presented for the four levels of confinement in Figure 3-32. Here the effect of confinement on strength and dilatancy can be clearly seen. For confinement levels of 6.89 MPa, CIF values of almost 2 were observed. Average values of peak principal stress difference were taken for each loading condition. The average values are shown in Table 3-6 and are plotted in Figure 3-33. Over the confining pressure range investigated, the relationship between strength and confinement pressure is nearly linear.

Table 3-6: Average peak principal stress difference at failure for WES5000

Confining pressure (MPa)	0	1.72	3.45	6.89
Avg. peak principal stress diff. (MPa)	63.9	89.2	105.4	120.7

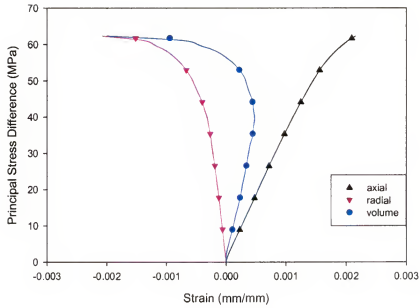


Figure 3-28: Quasi-static concrete unconfined (QSCU01)

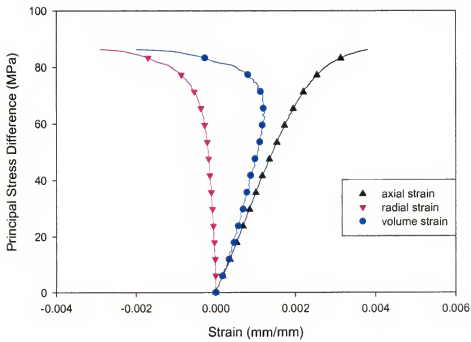


Figure 3-29: Quasi-static concrete confined (QSCC11) - 1.72 MPa confinement

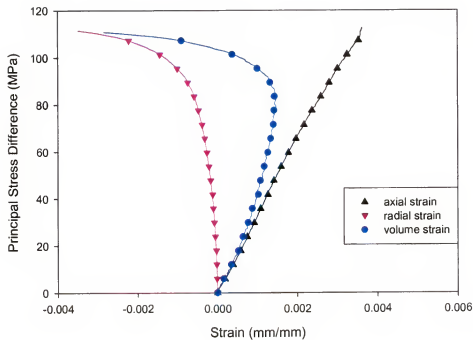


Figure 3-30: Quasi-static concrete confined (QSCC04) - 3.45 MPa confinement

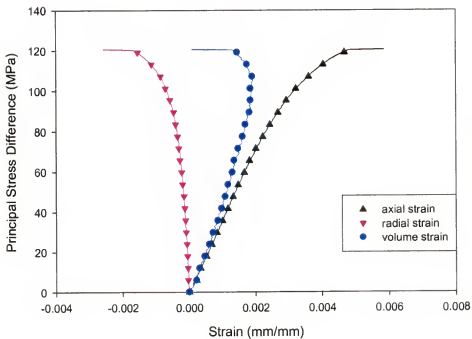


Figure 3-31: Quasi-static concrete confined (QSCC06) - 6.89 MPa confinement

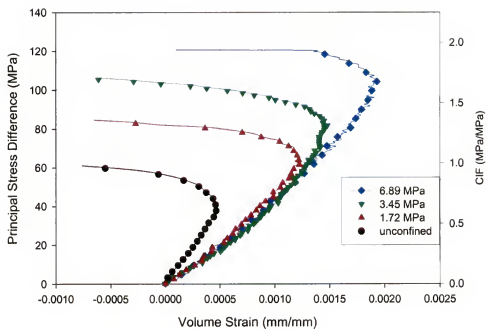


Figure 3-32: Confinement effect on quasi-static WES5000 behavior

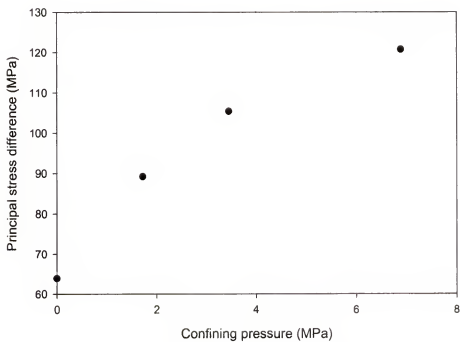


Figure 3-33: Peak principal stress difference at failure as a function of confinement for WES5000



### 3.4.2 SHPB Results

In order to characterize the dynamic behavior of WES5000, and the mortar material, a series of unconfined SHPB and confined experiments at 1.72 MPa (250 psi), 3.45 MPa (500 psi), and 6.89 MPa (1000 psi) were conducted following the protocol outlined in Section (3.3.4) of this chapter. The range of striker bar velocities was selected based on the capacity of the gas gun firing chamber. The highest velocity was taken to be the speed obtained by the 0.762m bar when the gun was pressurized to 3.45 MPa, the lowest was selected to correspond to a chamber pressure of 1.39 MPa (200 psi), while a mid-range velocity corresponded to 2.41 MPa (350 psi). For convenience, the low, medium, and high confining conditions are referred to as  $L_p$ ,  $M_p$ , and  $H_p$ , respectively while the low, medium, and high velocity conditions are denoted by  $L_v$ ,  $M_v$ , and  $H_v$ .

#### Dynamic Characterization of Mortar

A total of 36 SHPB experiments were performed on the mortar material under confined and unconfined conditions. The test conditions are given in Table 3-7. DCMC and DCMU stands for Dynamic Compression Mortar Confined and Unconfined respectively. Each experiment was also given a two digit numerical identifier. Experiments DCMC01 through DCMC12 were performed for the purposes of developing the experimental protocol and the results are not presented here.

A one-wave analysis was utilized, thus the peak principal stress difference values (referred to as  $q_{max}$ ) were derived solely from the transmitted pulse. Since strains were measured directly on the specimens, there was no need to time shift and combine the incident and reflected pulses to determine the axial strains. Due to the large number of tests there was a great deal of motivation to develop a technique for partially automating the process. Most existing techniques rely on the precise timing of the pulses. Kaiser [39] developed a technique based on

Table 3-7: Mortar SHPB test conditions

Experiment #	Design condition	Striker (m)	$P_g(MPa)$	$P_c(MPa)$	Date
DCMC13	$L_v M_p$	0.762	1.38	3.45	8-Mar-1999
DCMC14	$L_v M_p$	0.762	1.38	3.45	8-Mar-1999
DCMC15	$L_v M_p$	0.762	1.38	3.45	17-Mar-1999
DCMC16	$H_v M_p$	0.762	3.45	3.45	17-Mar-1999
DCMC17	$H_v M_p$	0.762	3.45	3.45	24-Mar-1999
DCMC18	$H_v M_p$	0.762	3.45	3.45	29-Mar-1999
DCMC19	$M_v M_p$	0.762	2.41	3.45	2-Apr-1999
DCMC20	$M_v M_p$	0.762	2.41	3.45	2-Apr-1999
DCMC21	$M_v M_p$	0.762	2.41	3.45	4-Apr-1999
DCMC22	$M_v H_p$	0.762	2.41	6.14	4-Apr-1999
DCMC23	$L_v H_p$	0.762	1.38	6.89	29-Apr-1999
DCMC24	$L_v H_p$	0.762	1.38	6.89	30-Apr-1999
DCMC25	$H_v H_p$	0.762	3.45	6.89	3-May-1999
DCMC26	$H_v H_p$	0.762	3.45	6.89	3-May-1999
DCMC27	$H_v L_p$	0.762	3.45	1.72	3-May-1999
DCMC28	$H_v L_p$	0.762	3.45	1.72	1-May-1999
DCMC29	$L_v H_p$	1.0	2.07	6.89	13-May-1999
DCMC30	$L_v H_p$	1.0	2.07	6.89	14-May-1999
DCMC31	$M_v L_p$	1.0	4.14	1.72	14-May-1999
DCMC32	$M_v L_p$	1.0	4.27	1.72	17-May-1999
DCMC33	$M_v H_p$	1.0	4.27	6.89	20-May-1999
DCMC34	$M_v H_p$	1.0	4.27	6.89	24-May-1999
DCMC35	$M_v H_p$	1.0	4.27	6.89	25-May-1999
DCMC36	$L_v L_p$	1.0	2.07	1.72	25-May-1999
DCMC37	$L_v L_p$	1.0	2.07	1.72	26-May-1999
DCMC38	$L_v L_p$	1.0	2.07	1.72	27-May-1999
DCMC39	$M_v L_p$	1.0	4.27	1.72	27-May-1999
DCMU01	$L_v$	0.762	1.03	-	23-Sep-1998
DCMU02	$L_v$	0.762	1.03	-	23-Sep-1998
DCMU03	$L_v$	0.762	1.38	-	22-Oct-1998
DCMU04	$L_v$	0.762	1.38	-	26-Oct-1998
DCMU05	$H_v$	0.762	3.45	-	19-Nov-1998
DCMU06	$M_v$	0.762	2.41	-	7-Feb-2000
DCMU07	$M_v$	0.762	2.41	-	7-Feb-2000
DCMU08	$M_v$	0.762	2.41	-	7-Feb-2000
DCMU09	$H_v$	0.762	3.45	-	7-Feb-2000

taking numerical derivatives of the signal and applying a rule regarding a minimum number of same sign derivatives to identify the start of the pulse. The technique utilized in this research was a statistical one. The leading pre-trigger signal background noise was evaluated and the standard deviation and mean determined. Using the mean, the signal could be automatically base-line shifted, accounting for any instrumentation offset. Based on the background noise analysis, the incident and transmitted signals were compared to the standard deviation. A consistent positive deviation from the standard deviation was determined to indicate the start of the pulses. Since the mid-point of the SHPB specimen was half way between the two SHPB strain gauges, the specimen strain gauges were set to zero corresponding to a point half the difference between the start of the incident and transmitted pulse. The results of the SHPB mortar experiments are summarized in Table 3-8. The column heading labeled "Comments" always contains a letter which is either A, B, C, or D. These letter designators are an attempt to provide a qualitative measure of the damage observed in the specimen post test. A designation of "A" means that there was either no, or only superficial visible damage to the specimen, "B" corresponded to cracking in the specimen. Crack orientation was generally at a 45-degree orientation to the vertical axis, indicative of shear failure. A damage state of "C" was meant to indicate that the specimen was no longer capable of sustaining any appreciable load. This generally meant that the specimen was in several pieces post test. The designation of "D" was indicative of total material failure, and was only observed in the unconfined experiments. Figures 3-34 through 3-36 are representative of the visible damage observed post test for mortar. There were no instances of the severe level-C failure in the mortar experiments. In fact, most of the specimens showed very little damage post test other than some chipping around the top edges, most likely due to localized tensile effects.

Table 3-8: Mortar SHPB results

Experiment #	$V_s$ (m/s)	$\dot{\epsilon}$ (s <sup>-1</sup> )	$q_{max}$ (MPa)	Comments
DCMC13	-	-	-	A (no data)
DCMC14	-	74.9	40.0	A
DCMC15	-	67.1	62.34	A
DCMC16	-	120	94.1	B
DCMC17	-	117	117.97	A
DCMC18	-	130	107.5	A
DCMC19	11.14	110	96.0	B
DCMC20	11.23	90	106.7	A
DCMC21	11.23	105	101.2	B (no press.)
DCMC22	7.79	62	88.75	A
DCMC23	7.6	54	90.3	A
DCMC24	7.76	60	93.4	A
DCMC25	13.78	122	136.9	A
DCMC26	13.71	-	-	B (no press.)
DCMC27	13.61	120	104	B
DCMC28	13.93	131	103.6	B
DCMC29	7.51	-	-	A
DCMC30	-	41	107.6	A
DCMC31	10.8	87	107.6	B
DCMC32	11.01	51	95.9	B
DCMC33	11.31	48.7	115.6	A
DCMC34	11.19	38.3	117	A
DCMC35	11.04	54	113.9	A
DCMC36	7.23	46	89.3	A
DCMC37	7.27	46.2	76.7	B
DCMC38	7.29	40	84.0	B
DCMC39	11.16	88	100.2	B
DCMU01	-	71.2	70.18	D
DCMU02	-	65.2	65	D
DCMU03	-	75	75.5	D
DCMU04	-	60	76.9	D
DCMU05	-	156	98.6	D
DCMU06	11.36	108	117.1	D
DCMU07	11.32	-	-	D
DCMU08	11.39	111	113.6	D
DCMU09	14.01	125	126.6	D

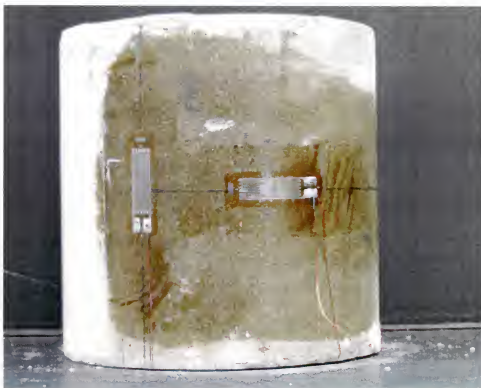


Figure 3-34: Damage state A - DCMC14



Figure 3-35: Damage state B - DCMC27

In order to evaluate the influence of loading rate and confinement on the materials volumetric behavior and strength, plots were made for each experiment of axial, radial, and volume strain as a function of principal stress difference, or  $q$ . Representative examples for each loading case are presented below. Figure 3-37 shows the results of the unconfined test DCMU04, conducted under low striker bar velocity conditions. The strain rate determined from the reflected pulse was 60/s. The response of the specimen is qualitatively similar to the unconfined response, in that it exhibits both compressive and dilatant behavior. Significant strength enhancement over the unconfined compressive strength is also observed. Only the data recorded at 25  $\mu$ s intervals are shown in the plots. According to Davies and Hunter [22]  $\pi$  reverberations are required for the specimen to “ring up” and achieve a uniform stress state. Since the elastic wave speed of mortar is approximately 4.8 km/s, about 100  $\mu$ s would be required for the specimen to achieve a uniform stress state. Thus, for the lowest loading rate condition, stress uniformity can be assumed only at the onset of failure. Therefore, from the unconfined experiments, only information concerning the peak load as a function of strain rate may be deemed reliable. Volumetric strain curves as a function of principal stress difference for unconfined conditions and at three different strain rates (from quasi-static to 160/s) are presented in Figure 3-38. The concept of a Dynamic Increase Factor (DIF) is introduced here to help quantify the influence of loading rate on strength. The DIF is defined as the dynamic strength normalized by the unconfined compressive strength [40]. The DIF is given on the right hand axis of Figure 3-38. For the examples shown, over the range of strain rates, the material continues to exhibit both compressible and dilatant behavior. Strength enhancement is obvious with a DIF value of approximately 1.8 apparent for the 160/s strain rate curve. The transition from compressibility to dilatancy also appears to be rate sensitive.



Figure 3-36: Damage state D - DCMU07

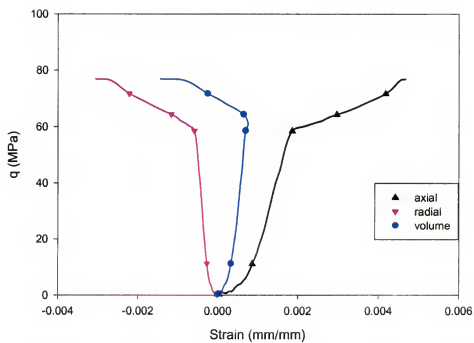


Figure 3-37: Direct compression mortar unconfined (DCMU04) -  $L_v$  condition

Next presented are results of the experiments at 1.72 MPa confinement corresponding to low, medium, and high striker velocity. In all three cases, after the initial stress rise, the majority of the material deformation took place under uniform stress conditions. Under each condition, mortar exhibits both compressive and dilatant behavior. Damage was not observed for the  $L_v L_p$  case, though it was present in the other two cases. Note that rate effects are less pronounced than under unconfined conditions.

Figures 3-42 to 3-44 are representative of the results observed at moderate confining conditions. Once again, the mortar exhibits compressibility and dilatancy. Rate effects again do not appear as pronounced as in the unconfined case. The major portion of each experiment also took place under uniform stress conditions. No damage was observed in any of the three cases presented.

The behavior in the experiments under 6.89 MPa confinement is purely compressive, hence markedly different than in those under lower confinement. No cracking was observed. The uniform stress assumptions again appears to have applied in all tests.

In order to quantify the influence of loading rate on strength at the various levels of confinement, the dynamic strengths given in Table 3-8 were normalized by the quasi-static strengths corresponding to the same level of confinement, thus yielding the DIF values as a function of confinement. In Figure 3-63 the DIF is plotted as a function of the  $\log_{10}(\dot{\epsilon})$ . It appears that under unconfined conditions, mortar follows the same rate sensitive trends as those reported in the literature for cementitious materials [40, 41, 42]. However, under confined conditions the DIF values for mortar are significantly lower.

Several conclusions may be drawn at this point. Though mortar is highly rate sensitive at unconfined conditions, the rate sensitivity appears to diminish with confinement. This same observation was also reported for concrete by Malvern and



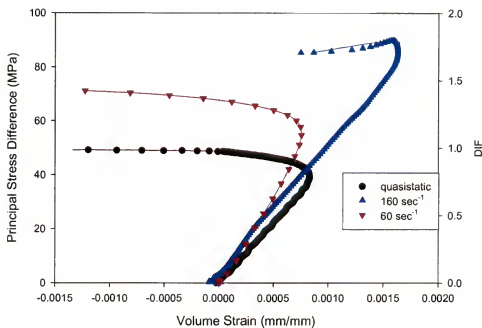


Figure 3-38: Unconfined mortar response at three different strain rates

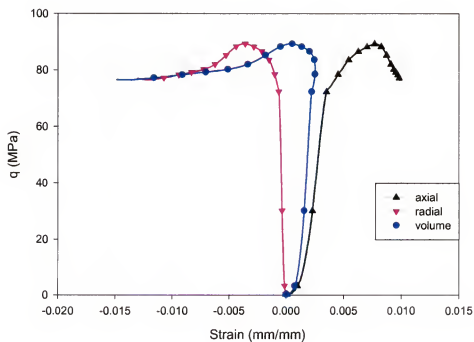


Figure 3-39: Direct compression mortar confined (DCMC36) -  $L_v$ ,  $L_p$  condition

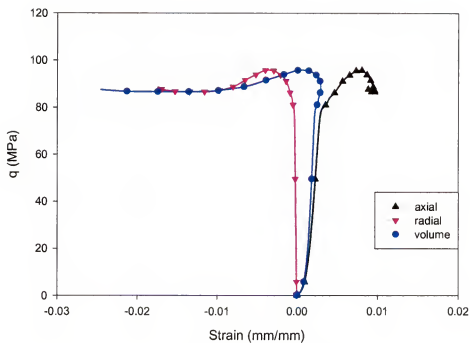


Figure 3-40: Direct compression mortar confined (DCMC32) -  $M_v, L_p$  condition

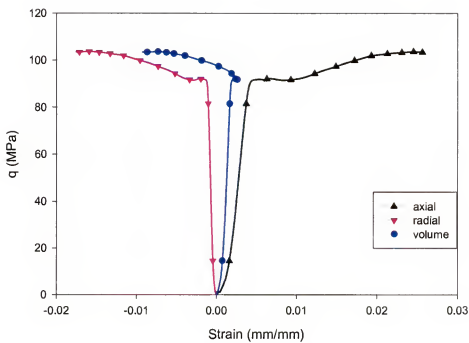


Figure 3-41: Direct compression mortar confined (DCMC28) -  $H_v, L_p$  condition

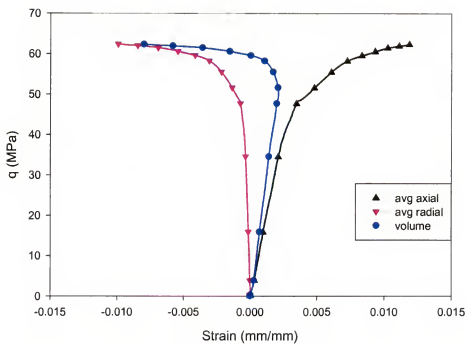


Figure 3-42: Direct compression mortar confined (DCMC15) -  $L_v, M_p$  condition

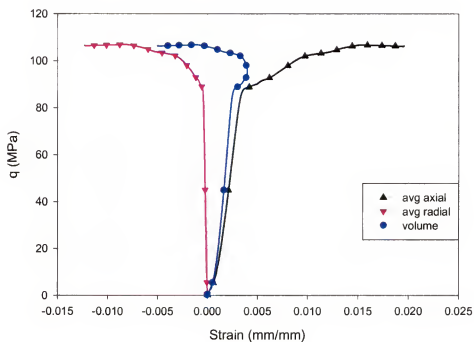


Figure 3-43: Direct compression mortar confined (DCMC20) -  $M_v, M_p$  condition

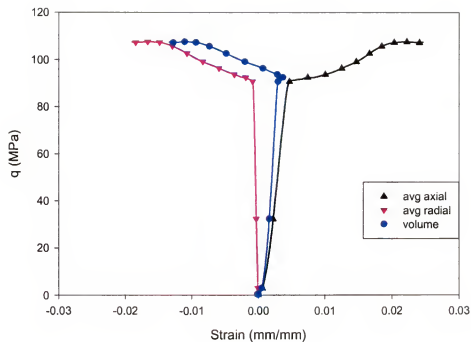


Figure 3-44: Direct compression mortar confined (DCMC18) -  $H_v$ ,  $M_p$  condition

Jenkins [34] and Malvern et al. [43]. The materials susceptibility to damage under shear loads appears to be more a function of confinement than loading rate. Also, though the uniform stress requirements were not met under uniaxial conditions, minimal levels of confinement yielded valid constitutive property data over the majority of the duration of the experiments.

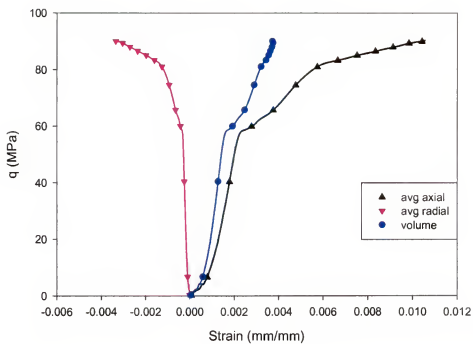


Figure 3-45: Direct compression mortar confined (DCMC29) -  $L_v, H_p$  condition

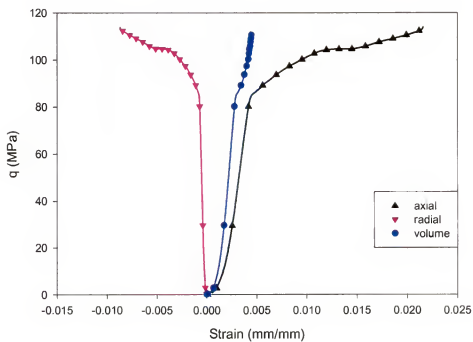


Figure 3-46: Direct compression mortar confined (DCMC35) -  $M_v, H_p$  condition

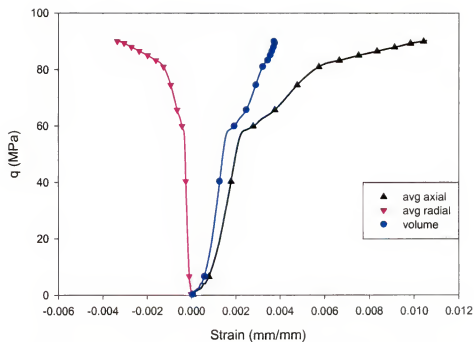


Figure 3-47: Direct compression mortar confined (DCMC26) -  $H_v$ ,  $H_p$  condition

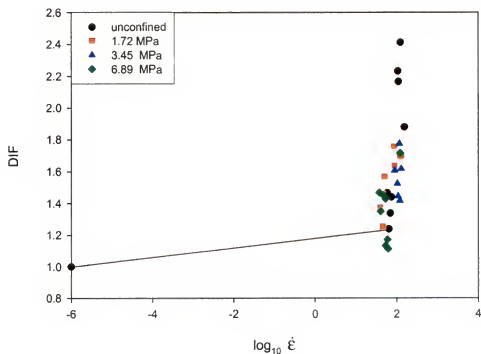


Figure 3-48: Effect of confinement on mortar DIF

### WES5000

The following section presents the dynamic characterization effort undertaken for WES5000. The same analysis techniques utilized for the mortar samples were employed. A total of 35 SHPB experiments were conducted under both confined and unconfined conditions. Table 3-9 summarizes the conditions under which the experiments were conducted. The naming convention utilized is the same as for mortar, obviously DCCC and DCCU stand for Dynamic Compression Concrete Confined and Unconfined, respectively. Results as well as comments concerning the experiments are summarized in Table 3-10. The same damage designations letters used in discussing the results on mortar are utilized for WES5000.

Figures 3-49 through 3-52 show the observed damage. Unlike mortar, the more severe type "C" response was observed in a number of cases under confined conditions. In order to evaluate the material response to the different loading conditions, the principal stress difference versus axial, radial, and volumetric strains curves were plotted. Representative results corresponding to each loading condition are shown in Figures 3-53 through 3-62.

Figure 3-53 shows the results of an unconfined SHPB experiment (DCCU03) conducted under the low striker bar velocity conditions ( $L_v$ ). The lines represent all the recorded data, while the symbols (circles and triangles) represent data points recorded at every 25  $\mu\text{s}$ . The volumetric stress strain curve shows that the material exhibits both compressive and dilatant behavior. Note also that WES5000 exhibits strong rate dependency, the unconfined strength at a strain rate of  $55.6 \text{ s}^{-1}$  is nearly the double of the quasi-static strength. A damage level of "D" was observed for unconfined conditions regardless of the striker bar velocity. Under the Davies-Hunter criteria, approximately 100  $\mu\text{s}$  would again be required for achievement of stress uniformity. Careful examination of the data (Figure 3-53) shows that the specimen fails in a little over 75  $\mu\text{s}$ , thus the specimen never

Table 3-9: Test conditions for WES5000 SHPB experiments

Experiment #	Design condition	Striker(m)	$P_g$ (MPa)	$P_c$ (MPa)	Date
DCCC01	$L_v M_p$	1.0	2.07	3.45	17-May-1999
DCCC02	$L_v M_p$	1.0	2.07	3.45	19-May-1999
DCCC03	$L_v M_p$	1.0	2.07	3.45	19-May-1999
DCCC04	$M_v M_p$	1.0	4.27	3.45	19-May-1999
DCCC05	$L_v M_p$	1.0	2.07	3.45	25-May-1999
DCCC06	$M_v M_p$	1.0	4.27	3.45	25-May-1999
DCCC07	$L_v H_p$	1.0	2.07	6.89	28-May-1999
DCCC08	$L_v H_p$	1.0	2.07	6.89	28-May-1999
DCCC09	$H_v L_p$	0.762	3.45	1.72	24-Nov-1999
DCCC10	$H_v L_p$	0.762	3.45	1.72	30-Nov-1999
DCCC11	$L_v L_p$	0.762	1.38	1.72	6-Jan-2000
DCCC12	$L_v L_p$	0.762	1.38	1.72	13-Jan-2000
DCCC13	$M_v L_p$	0.762	2.41	1.72	17-Jan-2000
DCCC14	$M_v L_p$	0.762	2.41	1.72	18-Jan-2000
DCCC15	$H_v H_p$	0.762	3.45	3.45	25-Jan-2000
DCCC16	$H_v M_p$	0.762	3.45	3.45	25-Jan-2000
DCCC17	$M_v H_p$	0.762	3.45	6.89	26-Jan-2000
DCCC18	$L_v H_p$	0.762	1.38	6.89	26-Jan-2000
DCCC19	$M_v H_p$	0.762	2.41	6.89	27-Jan-2000
DCCC20	$H_v H_p$	0.762	3.45	6.89	31-Jan-2000
DCCC21	$M_v H_p$	0.762	2.41	6.89	31-Jan-2000
DCCC22	$L_v H_p$	0.762	1.38	6.69	14-Feb-2000
DCCU01	$L_v$	0.762	1.38	-	22-Dec-1998
DCCU02	$L_v$	0.762	1.38	-	22-Dec-1998
DCCU03	$L_v$	0.762	1.38	-	22-Dec-1998
DCCU04	$L_v$	0.762	1.38	-	22-Jan-1999
DCCU05	$M_v$	0.762	2.41	-	22-Jan-1999
DCCU06	$M_v$	0.762	2.06	-	3-Feb-2000
DCCU07	$M_v$	0.762	2.06	-	3-Feb-2000
DCCU08	$M_v$	0.762	2.06	-	3-Feb-2000
DCCU09	$M_v$	0.762	2.41	-	7-Feb-2000
DCCU10	$M_v$	0.762	2.41	-	7-Feb-2000
DCCU11	$H_v$	0.762	3.45	-	7-Feb-2000
DCCU12	$H_v$	0.762	3.45	-	14-Feb-2000
DCCU13	$M_v$	0.762	3.45	-	14-Feb-2000



Table 3-10: Results for WES5000 SHPB experiments

<i>Experiment #</i>	$V_s$ (m/s)	$\dot{\epsilon}$ (s <sup>-1</sup> )	$q_{max}$ (MPa)	<i>Comments</i>
DCCC01	—	-	100.18	A
DCCC02	7.44	48	121.7	A
DCCC03	7.52	47	121.1	B
DCCC04	11.34	54	136.4	B
DCCC05	7.27	46.5	128.6	B
DCCC06	11.06	77.8	164	C
DCCC07	7.26	49.8	85.1	A
DCCC08	7.37	50.0	91.1	A
DCCC09	-	-	-	B (no press. signal)
DCCC10	-	139.7	166.2	B
DCCC11	8.18	57	121.5	B
DCCC12	8.18	59	123.57	B
DCCC13	-	104	139	C
DCCC14	11.51	113.8	138.8	C
DCCC15	-	113.9	123.6	B
DCCC16	-	113.8	123.6	B
DCCC17	-	0.762	138.8	B
DCCC18	8.19	42	138.1	A
DCCC19	-	80.8	160.1	B
DCCC20	14.27	103.5	176.8	C
DCCC21	-	77.4	168.6	B
DCCC22	8.01	47.6	123.6	A
DCCU01	-	63.3	67.8	D
DCCU02	-	65.8	89.2	D
DCCU03	-	55.6	114.56	D
DCCU04	-	60.7	89.64	D
DCCU05	-	109.3	120.786	D
DCCU06	10.37	96.8	121.978	D
DCCU07	10.37	101.3	119.467	D
DCCU08	10.38	94.49	146.455	D
DCCU09	11.42	105.37	128.587	D
DCCU10	11.39	88.5	153.008	D
DCCU11	14.06	129.15	155.45	D
DCCU12	13.98	126.4	163.769	D
DCCU13	13.93	133.39	160.623	D



Figure 3-49: Damage state A - WES5000

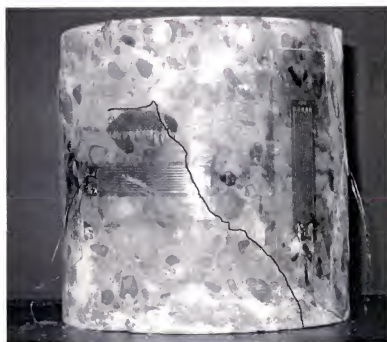


Figure 3-50: Damage state B - WES5000



Figure 3-51: Damage state C - WES5000



Figure 3-52: Damage state D - WES5000

achieves a uniform stress state. Thus, only the peak stress as a function of time may be considered as being representative of the material behavior. The same conclusion can be drawn concerning the results obtained for the higher impact velocities. Also, as for mortar at higher velocities, transition to dilatant behavior is not observed.

The next three figures (3-54 to 3-56) present representative results under low confinement corresponding to low, medium, and high loading rates, respectively. In all three cases, the material first exhibits compressive behavior, followed by a transition to dilatancy. Significant dynamic strength enhancement is again observed, though not on the same order as in the unconfined case. Except for a small portion of the experiment conducted under  $L_v$  conditions, the specimens fail prior to achieving stress uniformity and can not be considered valid SHPB experiments except for discerning the influence of loading rate on failure strength. For all three conditions presented, severe diagonal cracking was observed.

The following three cases concern moderate confinement at low, medium, and high loading rates. Stress uniformity was achieved prior to failure. Regardless of the strain rate, compressibility followed by dilatant behavior is observed. Strain rate influence is less pronounced than under unconfined conditions. No visible damage was observed for the lowest strain rate conditions, however significant diagonal cracking was observed under higher strain rates.

Finally, Figures 3-60 to 3-62 show the test results under 6.89 MPa conditions corresponding to three different loading rates. Under moderate and high loading rate conditions the material exhibits both compressive and dilatant behavior, but at the lowest loading rate tested, only compressive behavior was observed. No damage was observed at the lowest loading rate, while significant cracking occurred under higher loading rate conditions. In order to quantify the influence of loading rate on strength, the dynamic strengths given in Table 3-10 were normalized by the

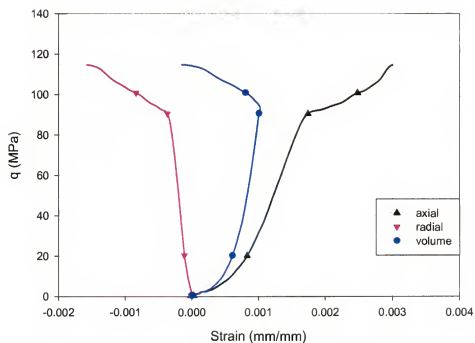


Figure 3-53: Direct compression concrete unconfined (DCCU03) -  $L_v$  condition

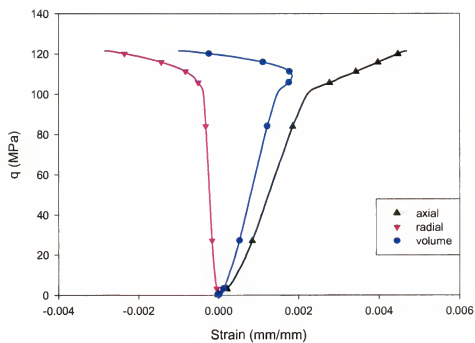


Figure 3-54: Direct compression concrete confined (DCCC11) -  $L_v, L_p$  condition

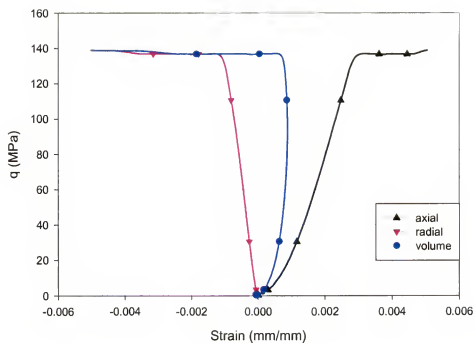


Figure 3-55: Direct compression concrete confined (DCCC13) -  $M_v$ ,  $L_p$  condition

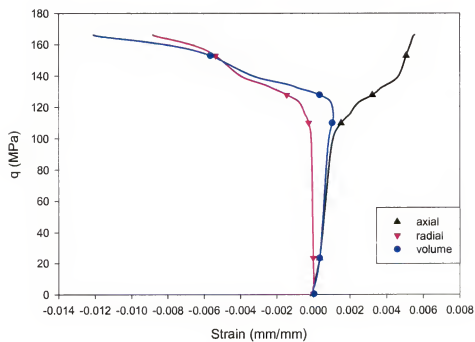


Figure 3-56: Direct compression concrete confined (DCCC10) -  $H_v$ ,  $L_p$  condition

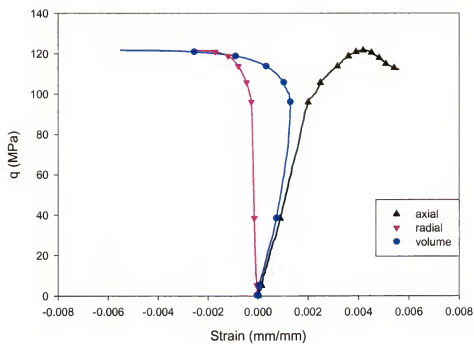


Figure 3-57: Direct compression concrete confined (DCCC02) -  $L_v$ ,  $M_p$  condition

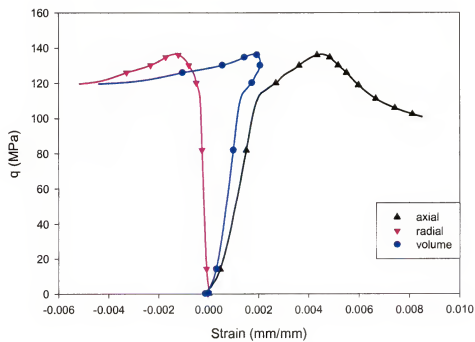


Figure 3-58: Direct compression concrete confined (DCCC04) -  $M_v$ ,  $M_p$  condition

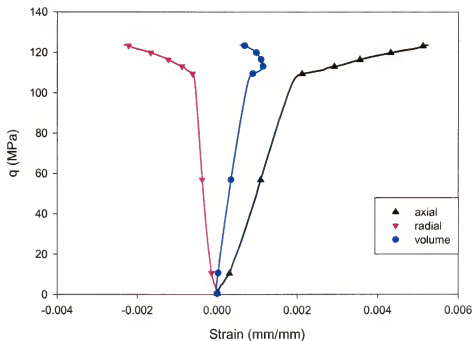


Figure 3-59: Direct compression concrete confined (DCCC15) -  $H_v$ ,  $M_p$  condition

quasi-static strengths corresponding to the same level of confinement, thus yielding the DIF values as a function of confinement. In Figure 3-63 the DIF is plotted as a function of the  $\log_{10}(\dot{\epsilon})$ . It can be concluded that under unconfined conditions, WES5000 follow the same trends as mortar and those reported in the literature [40, 41, 42] for other cementitious materials. However, under confined conditions the DIF values for WES5000 are significantly lower. This is again in agreement with the findings of Malvern and Jenkins [34] and Malvern et al. [43]. Note also that WES5000 generally exhibited far more cracking under similar loading conditions than mortar. Thus, while WES5000 is a significantly stronger material, it also exhibits far less ductility. Finally, it was again observed that minimal levels of confinement can be utilized to generate valid constitutive property data in a SHPB even for brittle materials such as concrete.



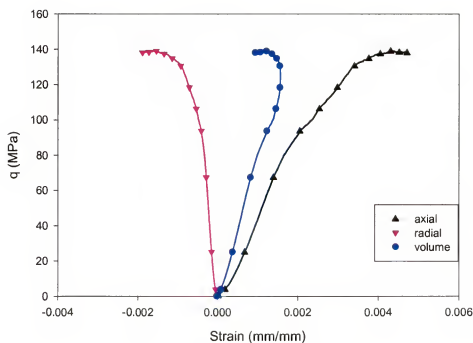


Figure 3-60: Direct compression concrete confined (DCCC18) -  $L_v, H_p$  condition

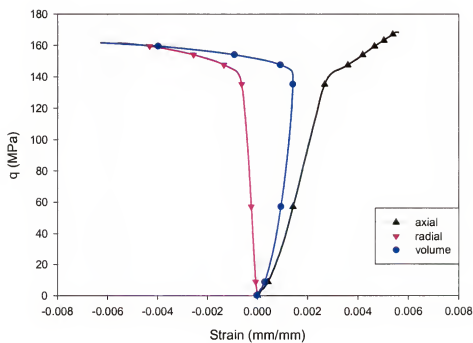


Figure 3-61: Direct compression concrete confined (DCCC21) -  $M_v, H_p$  condition

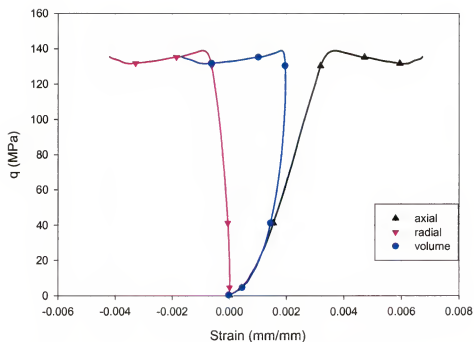


Figure 3-62: Direct compression concrete confined (DCCC17) -  $H_v, H_p$  condition

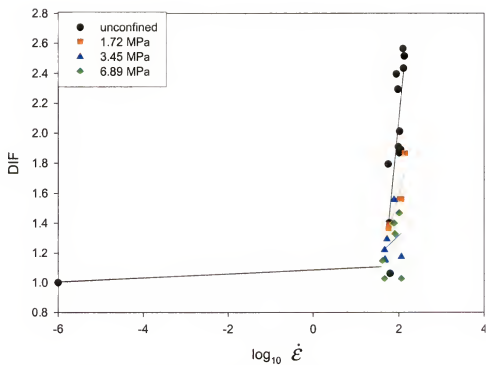


Figure 3-63: Effect of confinement on WES5000 DIF

## CHAPTER 4 CONSTITUTIVE MODELING

### 4.1 Introduction

A constitutive model consists of a set of stress-strain (time) relationships. The choice of a material model formulation is generally guided by three factors, these being:

- The scale of the problem
- The type of material and behavior of interest for a given problem
- Available computational resources.

In this chapter, after a review of concrete continuum based constitutive models, an elastic/viscoplastic model for WES5000 concrete is presented. The model developed is based on data obtained in the series of tests reported in Chapters 2 and 3. The procedure for determination of the constitutive functions and the parameters involved in their expressions is outlined. Finally, comparisons are made between the theoretical predictions and experimental results.

### 4.2 Concrete Constitutive Modeling Review

#### 4.2.1 Introductory Note

The development of material models is inseparably linked to the development of advanced numerical analysis techniques and computational capabilities. The accuracy and utility of numerical simulations are limited by the material descriptions (Zukas et al. [1]) whereas the degree of complexity of constitutive models is limited by the computation time and robustness of numerical algorithms used in the simulations. Nowadays, general purpose finite element and finite difference methods provide means for simulating penetration events and allow a wide range of thought experiments that would not be otherwise possible. One of the earliest works in the

area of Finite Element Methodology was that of mathematician Richard Courant, who in 1943 used piecewise linear functions on triangles [44] to obtain numerical solution of partial differential equations. The triangular linear element is referred to as the Courant element. The work of Turner, Clough, Martin and Topp in 1956 is generally regarded as the first paper on Finite Element Methodology in engineering [45]. In this landmark paper, the authors proposed to use the displacement method to derive the stiffness of plane elements. In 1960, Clough [46] coined the phrase Finite Element Method (FEM) in a paper presented at the 2<sup>nd</sup> ASCE Conference on Electronic Computation. The first application of FEM to the analysis of reinforced concrete beams was by Ngo and Scordelis [47] in 1967. Due to the lack of generally accepted constitutive equations for concrete [48], in most of the early FEM analyses concrete was considered to obey a linear elastic stress-strain law. Also, FEM methods were mostly applied to simulate quasi-static structural problems while finite difference methods were applied to hypervelocity impact problems. However, early finite difference formulations were used in conjunction with material models that did not account for strength effects. All materials were treated as fluids, thus the term “hydrodynamic code,” or “hydrocode,” came into use. To better describe lower velocity regime problems, later versions of hydrocodes included strength effects. More details concerning hydrocode’s development can be found in the review paper by Anderson [49]

#### 4.2.2 Micromechanical Modeling

There is a tremendous amount of information available in the open literature concerning modeling the behavior of concrete. In micromechanics based effective medium models, the overall continuum properties of concrete are estimated using different averaging (homogenization) procedures from the properties and structure of each of its microconstituents. Specifically, concrete is considered to be a composite consisting of randomly distributed inclusions (aggregate particles) embedded

in a continuous, porous matrix (hardened cement paste). It is to be noted that the most widely used effective medium homogenization methods such as the self-consistent method, the differential scheme, the generalized self-consistent method and Mori-Tanaka methods [50] do not apply to arbitrarily located and oriented microcracks. Embedded in the mentioned averaging techniques is the restriction that there is a dilute concentration of defects and that those defects are non-interacting [51]. Improved formulations that account for interacting microcracks have been developed by Ju and co-workers (e.g. Ju and Tseng [52]) for 2-D conditions. The great majority of these micromechanics based models are applicable only to short-term quasi-static stress conditions. Very few models account for high-strain rate, high-pressure behavior. Examples include Xia [53] and Thoma et al. [54]. An alternative method to obtain the macro-level properties in terms of the properties of the constituents is offered by the mixture theory [55]. Such an approach was used by Ortiz [56] for concrete. In all effective medium models, the material is treated as quasi-homogeneous (statistical homogeneity assumptions) at the macro-scale. At difference with effective medium models, in Discrete Element models (DEM) the material is treated as heterogeneous at the macro-scale. Specifically, the material is discretized into individual elements or blocks, which are allowed to interact as stress is applied [57]. Void growth and cracking are represented by separation of adjoining elements due to shear induced sliding. Hentz et al. [58] has recently reported on a concrete DEM model in which elastic forces with a local rupture criteria are applied between interacting elements. Macro-scale level experiments and numerical simulations are used to calibrate the model parameters. Applications of DEM to modeling the dynamic behavior of concrete have been reported by Camborde et al. [59] and Donzé et al. [60], who used the technique in the analysis of flyer plate and SHPB experiments, respectively. Very good agreement with experiments was obtained. However, DEM approach is generally not applicable

to large scale problems. The microstructural variables that must be recorded and used in the computation of the deformations may require an unduly large amount of storage capacity and manipulation of data. Computation time required to solve even simple problems can be excessive. Material boundary interface treatments, numerical accuracy and mesh dependencies may also dominate the problem.

#### 4.2.3 Macromechanical Models

A promising approach for practical large-scale problems is to treat concrete as a homogeneous continuum. Two main methods have been adopted: (1) empirical methods and (2) constitutive modeling. Empirical models result from curve-fits of experiments by means of simple functions. The characteristics of these functions are chosen just to meet the shape of the experimentally observed stress-strain curves and do not have any physical basis. Generally, empirical laws are one-dimensional and apply only to problems having boundary conditions and loading paths similar to those used in the tests based on which the laws were derived. It is possible to take into account the macroscopic experimental results by constructing a continuum model with a set of thermodynamic internal state variables that characterize the microstructure of the material. In the case of cementitious materials, damage related parameters are used extensively as internal variables accounting for the effect of microcracking on the macroscopic behavior. Most of the early work and most of the models that have been actually applied to concrete are based on a single scalar representation of the damage (e.g. Kachanov [61], Lemaitre and Chaboche[62], Lemaitre[63], etc). However, test results under both quasi-static and dynamic conditions show that damage itself and its effect on the material effective compliance are anisotropic. To account for the directionality of damage, different higher order tensorial representations were proposed. The list runs from vectors (e.g. Davison and Stevens [64], Krajcinovic and Fonseka [65], Talreja [66]), second order tensors (e.g. Vakulenko and Kachanov [67], Dragon

and Mroz [68], Kachanov [69, 70], Cordebois and Sidoroff [71], Murakami [72], Murakami and Kamiya [73], etc.) to fourth-order tensors (e.g. Chaboche [74], Simo and Ju [75], Chow and Wang [76], Lubarda and Krajcinovic [77], Halm and Dragon [78], etc.). However, the existing continuum damage mechanics (CDM) models are rate-independent and unable to describe simultaneously: (1) the directionality of damage and the corresponding induced anisotropy in behavior and (2) damage activation-deactivation process. Very few CDM models accounting for the dynamic behavior of cementitious materials have been proposed. At Sandia, Taylor et al. [79], have proposed a CDM model which uses a scalar damage parameter and combines the theory of fracture mechanics governing the behavior of individual cracks with the fragment size equation, which is based on kinetic energy considerations (Grady [80]). However, the model allows for damage growth only under hydrostatic tension; under compression loading the model is rate independent. Considerable efforts have also been undertaken to adapt models developed for metallic materials to describe the non-linear irreversible behavior of concrete. The most widely used formulations are Mohr-Coulomb or Drucker-Prager [48] which account for the experimentally observed influence of hydrostatic pressure on the behavior. It is thus assumed that concrete is perfectly plastic, i.e. the yield locus is fixed in the stress space. Hence, the yield surface coincides with the failure surface. According to Mohr-Coulomb theory failure occurs under compression when

$$\tau = \sigma_n \tan \phi_0 + C_0 \quad (4.1)$$

where:  $\tau$  is the shear stress on the failure plane,  $\sigma_n$  is the normal stress on that plane, and  $\phi_0$  and  $C_0$  are material constants. The angle of internal friction,  $\phi_0$ , and the cohesion  $C_0$  can be determined from triaxial compression data. Under tensile conditions it is generally assumed that the material fails if a predetermined level is achieved. This so called "tension cut-off" is estimated from unconfined tests. The

Drucker-Prager criterion is given by:

$$F_s = \sqrt{J_2} - p \tan \beta - d \quad (4.2)$$

where  $J_2$  is the second invariant of the stress deviator,  $p$  is the mean stress,  $\beta$  is a measure of the internal angle of friction, and  $d$  is the cohesion. Note that Mohr-Coulomb and Drucker-Prager surfaces are open in the direction of increasing hydrostatic compression. If the associativity assumption is adopted, i.e. the plastic potential coincides with the yield function, these criteria predict levels of dilatancy far in excess of what it is observed experimentally. The reason for this can be seen graphically in Figure 4-2. Indeed, the incremental volumetric strain rate vector is always in the direction of volumetric expansion. The Osborn model and Osborn and Matuska model for concrete which is implemented in HULL [81], a widely used and accepted continuum mechanics code, employs a Mohr-Coulomb yield criterion. The material parameters are obtained based on triaxial data generated by Chinn and Zimmerman [6] in the 1960s. It is stated that the Osborn model has been used “successfully in scores of calculations of penetrations into concrete at velocities from a few hundred to over 1000 feet/second.” However, experimental evidence clearly suggests that for cementitious materials a clear distinction exists between the stress conditions at which inelastic behavior initiates and those corresponding to failure. Among the models that account for pre-failure irreversible response double-surface models have become quite popular. These models are characterized by a hardening yield locus, referred to as cap, and by a fixed failure surface which is a limit of the admissible stress states. Typically, cap models are completed by providing a non-associative flow rule and elastic moduli which are stress-level dependent. Figure 4-3 illustrates the modified Drucker/Prager cap constitutive model. The shear failure surface is Drucker-Prager surface given by Equation 4.2. The cap has an elliptical shape in the plane  $(\sqrt{J_2}, I_1)$  and hardens or softens as



a function of the volumetric plastic strain: compaction produces hardening, while dilation produces shear induced softening. It is defined by:

$$F_c = \left\{ (p - p_a)^2 + \left[ \frac{R\sqrt{J_2}}{(1 + \alpha - \alpha/\cos\beta)} \right]^2 \right\}^{1/2} - R(d + p_a \tan\beta) = 0 \quad (4.3)$$

where  $R$ ,  $\alpha$  are constants and  $p_a$  is a function of the plastic volumetric strain.

Plastic flow is associated on the cap, and nonassociated on the failure surface.

Among the authors that applied this cap type model to describe concrete behavior under quasi-static conditions are Faruque and Chang [82], Simo et al. [83], etc. Very recently, Warren et al. [84] applied the same type cap model to describe the response of concrete targets to high-velocity impact. Schwer and Murray [85] proposed a cap model that depends on all three stress invariants. The numeric singularities at the cap and failure surface intersections are handled by smoothing the intersections. This model has been implemented into the FEM codes DYNA2D and DYNA3D. While cap type models have become widely accepted because they pair a relative simplicity, and therefore a limited number of parameters, to a description of the main features of the behavior of concrete, their applicability to high-velocity problems is questionable. This is due to the fact that such model are rate-insensitive. A review of rate-type constitutive equations is presented in the next section.

### Rate Dependent Models

To characterize the temporal growth of permanent deformation (flow of matter by creep) and strain rate effects on the behavior of certain materials viscoplastic models have been proposed. The basis of what is today called the mathematical theory of viscoplasticity was laid by Bingham [86]. According to Bingham, viscoplasticity is made up of two fundamental properties which are "yield value" and "mobility". The yield value is dependent on the shear stress required to start the deformation while the mobility is proportional to the rate of deformation

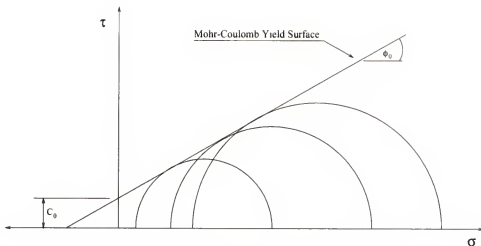


Figure 4-1: Mohr-Coulomb yield criterion

after the yield value has been exceeded. Hohenemser and Prager [87] proposed the first elastic/viscoplastic model. The basic hypotheses of this model are that the total strain rate is the sum of two components: the elastic component  $\dot{\varepsilon}_{ij}^E$  and the viscoplastic component  $\dot{\varepsilon}_{ij}^{vp}$  such that

$$\dot{\varepsilon}_{ij} = \dot{\varepsilon}_{ij}^E + \dot{\varepsilon}_{ij}^{vp} \quad \text{with} \quad 2G\dot{\varepsilon}_{ij}^E = \dot{\sigma}'_{ij} \quad (4.4)$$

and the viscoplastic strain rate being:

$$\dot{\varepsilon}_{ij}^{vp} = \frac{1}{2\eta} \left( 1 - \frac{k}{\sqrt{J_2}} \right) \sigma'_{ij} \quad \text{if} \quad J_2 > k^2 \quad (4.5)$$

where  $k$  is the yield value in shear and  $\sigma'_{ij}$  is the stress deviator.

Concerning the development of the mathematical modeling of strain rate effects on the irreversible strain properties of materials, an important date is 1948, with the introduction of Sokolovskii's [88] rate-type constitutive equation of the general form:

$$\dot{\sigma} = \phi(\varepsilon, \sigma) \dot{\varepsilon} + \psi(\varepsilon, \sigma) \quad (4.6)$$

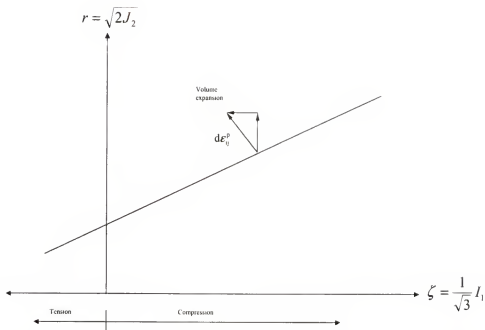


Figure 4-2: Dilatancy associated with yield surface open in positive direction

with  $\phi(\varepsilon, \sigma) = E$ , and

$$\psi(\varepsilon, \sigma) = \begin{cases} 0 & \text{if } |\sigma| < \sigma_Y \\ (-\text{sign } \sigma)F(|\sigma| - \sigma_Y) & \text{if } |\sigma| \geq \sigma_Y \end{cases} \quad (4.7)$$

where  $\sigma_Y > 0$  is the yield limit and  $F$  is a smooth function with  $F(r) > 0$ ,  $F'(r) > 0$  for  $r > 0$  and  $F(0) = 0$ . For any state  $(\varepsilon, \sigma)$  with  $|\sigma| < \sigma_Y$ , the response is elastic. From any state  $(\varepsilon, \sigma)$  with  $|\sigma| > \sigma_Y$ , the material relaxes to the state  $(\varepsilon, \sigma_Y)$  if  $\sigma > \sigma_Y$  or to the state  $(\varepsilon, -\sigma_Y)$  if  $\sigma < -\sigma_Y$ . Malvern [89, 90] also proposed a rate-type law of the type given by Equation 4.6 with  $\phi(\varepsilon, \sigma) = E$  and

$$\psi(\varepsilon, \sigma) = \begin{cases} 0 & \text{if } 0 \leq \sigma \leq f(\varepsilon), \quad \varepsilon \geq 0 \\ -kF(\sigma - f(\varepsilon)) & \text{if } \sigma > f(\varepsilon), \quad \varepsilon \geq 0 \end{cases} \quad (4.8)$$

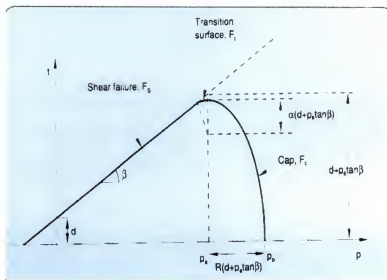


Figure 4-3: Modified Drucker/Prager cap model

where  $k > 0$  is a viscosity constant. Malvern considered  $F(r) = r$ . Other particular forms of the function  $F$  can be found in the monograph by Cristescu and Suliciu [88]. The curve  $\sigma = f(\varepsilon)$  is the quasi-static loading curve.

Another important date is 1951, with Malvern's law of logarithmic dependence of strength on strain rate [91]:

$$\sigma = f(\varepsilon) + a \ln(1 + b\dot{\varepsilon}) \quad (4.9)$$

where  $\sigma = f(\varepsilon)$  is the static stress-strain relation,  $\dot{\varepsilon}$  is the strain rate (irreversible strain rate), whereas  $a$  and  $b$  are material constants.

The Johnson-Cook model, which is one of the most widely used models for describing high strain behavior in metals, is essentially a variation on Equation 4.9.

$$\sigma = (A + B\varepsilon^n) \left[ 1 + C \ln \left( \frac{\dot{\varepsilon}}{\dot{\varepsilon}_0} \right) \right] (1 - T^{*m}) \quad (4.10)$$

In this equation,  $\varepsilon_0$  is a reference strain rate equal to  $1.0s^{-1}$ ,  $T^*$  is the homologous temperature, and  $A$ ,  $B$ ,  $n$ ,  $m$  and  $C$  are material constants. The Johnson-Cook

model was modified for use on brittle and geologic materials by Holmquist, Johnson and Cook [92]. This model states that:

$$\sigma^* = [A(1 - D) + BP^{*N}] [1 + C \ln \dot{\epsilon}^*] \quad (4.11)$$

where:  $\sigma^*$  is the normalized equivalent stress defined as  $\sigma^* = \sigma/f'_c$ ,  $D$  is a damage parameter,  $P$  is the hydrostatic pressure,  $P^* = P/f'_c$  is the normalized pressure, and  $A$ ,  $B$ ,  $N$  and  $C$  are material constants. A depiction of the model is presented in Figure 4-4. The tensile portion of the model is defined by  $T^* = T/f'_c$ , where  $T^*$  is the normalized maximum tensile hydrostatic pressure and  $T$  is the maximum hydrostatic pressure the material can withstand. The material constant  $S_{MAX}$  is the normalized maximum strength that can be developed.  $S_{MAX}$  essentially defines a von-Mises yield surface. The HJC model and similar formulations have

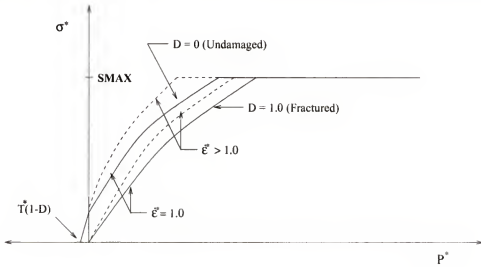


Figure 4-4: Holmquist-Johnson-Cook Model

been implemented into a number of continuum mechanics codes including EPIC and CTH and utilized successfully for a broad range of penetration calculations [93, 94, 95, 96, 97]. As can be seen in Figure 4-4 the model does not account for increased material strength at elevated pressures.

The early 1960's mark the development of the first 3-D elastic/viscoplastic equations by Perzyna [98] and Cristescu [99]. Following Perzyna [98], the structure and basic assumptions involved in the formulation of an elastic/viscoplastic type constitutive equation is presented. The formulation is similar to that of plasticity. Decoupling between elastic and viscoplastic effects is assumed such that:

$$\dot{\varepsilon}_{ij} = \dot{\varepsilon}_{ij}^E + \dot{\varepsilon}_{ij}^{vp} \quad (4.12)$$

where  $\varepsilon_{ij}^E$  is the elastic component and  $\varepsilon_{ij}^{vp}$  is the permanent (irreversible) part of the strain. The existence of a yield function which depends on the stress state and on the accumulated viscoplastic deformation is postulated:

$$F(\sigma_{ij}, \varepsilon_{kl}^{vp}) = \frac{f(\sigma_{ij}, \varepsilon_{kl}^{vp})}{k} - 1 \quad (4.13)$$

where  $f$  and  $k$  are scalar valued functions. The yield value,  $k$ , depends on the history of strain. The elasticity domain is defined as:  $F \leq 0$  or  $f \leq k$ . The problem of activation of viscoplastic flow is much simpler than in plasticity since any state outside of the elastic domain is viscoplastic and the viscoplastic strain increment depends only on the current values of the stress and hardening and not on the stress increment. No consistency condition needs to be reinforced. In the case of associated viscoplasticity, the flow rule is thus given by:

$$\dot{\varepsilon}^v_p = \mu \langle \Phi(F) \rangle \frac{\partial f}{\partial \sigma} \quad (4.14)$$

where  $\mu$  is the fluidity or viscosity parameter,  $\Phi$  is a monotonic function and the symbols,  $\langle \rangle$ , represent the so called Macaulay bracket, used to denote the positive part of a function (i.e.  $\langle A \rangle = (1/2)(A + |A|)$ ).

In the case of non-associated viscoplasticity it is assumed that the potential from which the viscoplastic strain rate is derived does not coincide with the yield function. Generally, the modeling strategy used is to consider that the expressions

of the yield and viscoplastic potentials are the same as the quasi-static (inviscid) expressions. For example, in Simo et al. [83] associated flow viscoplastic model for concrete, the expressions of the constitutive functions coincide with the expressions of the inviscid cap-model. This model is reportedly easy to implement and provides more accurate results than the inviscid form. The associated flow assumption is however responsible for non-representative compressive and dilatant behavior predictions.

In contrast to this approach, Cristescu [7, 8] proposed to determine for a given material the specific expressions of the constitutive functions based on data corresponding to several strain rates. The general form of the viscoplastic constitutive formulation proposed by Cristescu is:

$$\dot{\varepsilon}_{ij} = \frac{\dot{\sigma}_{ij}}{2G} + \left( \frac{1}{3K} - \frac{1}{2G} \right) \dot{p} \delta_{ij} + k_T \left\langle 1 - \frac{W(t)}{H(\sigma_{nn})} \right\rangle \frac{\partial F}{\partial \sigma_{ij}} \quad (4.15)$$

where:

$W \equiv$ Irreversible Stress Work	$K \equiv$ Bulk Modulus
$F \equiv$ Viscoplastic Potential	$G \equiv$ Shear Modulus
$H \equiv$ Yield Function	$\varepsilon_{ij} \equiv$ Strain Tensor
$k_T \equiv$ Viscosity Coefficient	$\sigma_{ij} \equiv$ Stress Tensor
$p \equiv$ mean normal stress	$\delta_{ij} \equiv$ Kronecker Delta
$\langle A \rangle \equiv \frac{1}{2} (A +  A )$	

No a priori assumptions concerning the specific mathematical expressions of the yield function and viscoplastic potential are made. The formulation does not assume a decoupling between shear and volumetric effects and does not require a separate equation of state in order to handle the pressure volume relationship. Since geomaterials and cementitious materials may display both compressible and dilatant behavior, the concept of compressibility/dilatancy boundary is integrated in the Cristescu model. This allows one to describe both compressibility and dilatancy using a unique continuous yield function and viscoplastic potential,

respectively. This is a significant advantage over rate sensitive cap models (e.g. Simo et al.) since it captures in a continuous way the transition between the two regimes of behavior. The model has been implemented for a wide range of materials [7, 100, 101, 12]. The formulation also does not require a separate equation of state in order to handle the pressure volume relationship. It has however, not been utilized for standard high-strength concrete or applied to highly dynamic loading environments. Experimental data on some geomaterials and granular materials do not support the hypothesis concerning the existence of a viscoplastic potential. An alternative flow rule formulation was proposed by Cazacu et al. [9] using representation theorems for isotropic scalar valued tensor functions. The remainder of this chapter deals with the development of an elastic/viscoplastic model for WES5000 concrete. The elastic-viscoplastic formulation of Cristescu is chosen due to its apparent capability to capture the behavior of interest and the fact that there are no a priori limitations or restrictions regarding the yield functions. To better describe the peculiarities of the viscoplastic flow behavior of WES5000, the approach proposed by Cazacu et al. [9] was adopted.

### 4.3 Elastic-Viscoplastic Model Development

The general form of the elastic-viscoplastic constitutive equation proposed in the previous section is repeated below 4.15:

$$\dot{\varepsilon}_{ij} = \frac{\dot{\sigma}_{ij}}{2G} + \left( \frac{1}{3K} - \frac{1}{2G} \right) \dot{p} \delta_{ij} + k_T \left\langle 1 - \frac{W(t)}{H(\sigma_{mn})} \right\rangle \frac{\partial F}{\partial \sigma_{ij}} \quad (4.15)$$

If material displacements and rotations are assumed to be small, an additive decomposition of the rate of deformation into an elastic instantaneous part and an irreversible part can be made.

$$\dot{\varepsilon} = \dot{\varepsilon}^E + \dot{\varepsilon}^I \quad (4.16)$$



The reversible deformation rate is given by the generalized Hooke's law:

$$\dot{\epsilon}_{ij}^E = \frac{\dot{\sigma}_{ij}}{2G} + \left( \frac{1}{3K} - \frac{1}{2G} \right) \dot{p} \delta_{ij} \quad (4.17)$$

in which both  $K$  and  $G$  are variable. The irreversible deformation rate is:

$$\dot{\epsilon}_{ij}^I = k_T \left\langle 1 - \frac{W(t)}{H(\sigma_{mn})} \right\rangle \frac{\partial F}{\partial \sigma_{ij}} \quad (4.18)$$

where the irreversible stress work,  $W(t)$ , is calculated as:

$$W(t) = \int_0^t \sigma_{ij}(t) \dot{\epsilon}_{ij}^I(t) dt. \quad (4.19)$$

Recalling the definition of the Macaulay bracket from the preceding section, if the stress state is such that  $H(\sigma_{m,n}) \leq W(t)$ , then the material response is elastic. If  $H(\sigma_{m,n}) > W(t)$ , further irreversible deformation may occur. In this model, no a priori assumptions concerning the mathematical expressions of the viscoplastic potential,  $F$ , and yield function,  $H$  are made. These expressions are determined from data collected on a given geologic/cementitious material in Kármán type experiments or true triaxial tests.

The first step in the development of an elastic-viscoplastic model for a particular material is the evaluation of the elastic parameters (i.e.  $K$  and  $G$ ). The accurate determination of these moduli is critical. The importance for evaluation of the reversible deformation rate (Equation 4.17) is obvious. In addition, since  $\dot{\epsilon}^I = \dot{\epsilon} - \dot{\epsilon}^E$ , a correct estimation is crucial in the determination of every aspect of the model. These parameters can be determined based on triaxial or Kármán type experiments. The elastic parameters are evaluated from the slopes of unload-reload cycles of such an experiment. The bulk modulus,  $K$ , is the slope of the unload-reload portion of the volume strain vs. mean normal stress curve of either the hydrostatic or deviatoric part of the experiment. The Young's modulus,  $E$ , is taken from the slope of the axial stress vs. strain unload-reload cycle. The shear

modulus,  $G$ , may be calculated from the relationship:

$$G = \frac{3KE}{9K - E} \quad (4.20)$$

Thus, all the elastic parameters of the model can be derived from a series of carefully controlled hydrostatic and deviatoric creep tests.

#### 4.4 Elastic Parameter Evaluation

As was mentioned in Section 4.2 (Elastic-Viscoplastic Modeling), the Young's modulus,  $E$ , is determined from the slope of the axial strain vs. principal stress difference curve unload-reload cycles. Values for  $E$  from the different quasi-static experiments were previously presented in Section 2.15 as a function of mean normal stress in Figure 2-57. Visual inspection of the figure indicates a very clear and consistent trend in the data, with all the experiments in general agreement. According to elastic wave theory, the maximum value of  $E$  is given by:

$$E = \rho v_B^2 \quad (4.21)$$

where  $\rho$  is the material density and  $v_B$  is the axial bar velocity, or P-wave velocity, using the notation of Table 2-3. Using values of density and wave speed tabulated for WES5000 in Table 2-3, the maximum value for  $E$  should be on the order of 61000 MPa. The data in Figure 2-57 does indeed appear to be asymptotically approaching such a value. A decaying exponential function of the form:

$$E(p) = a - be^{-\frac{p}{c}}, \quad \text{with } a, b, c > 0 \quad (4.22)$$

was found to approximate the data quite well. Here,  $p$  is the mean normal stress, or pressure, which is defined as:

$$p \equiv \frac{tr\sigma}{3}, \quad (4.23)$$

while  $a$  represents the asymptotic limit towards which  $E$  tends as  $p \rightarrow \infty$ . For  $p = 0$ ,

$$E(0) = a - b, \quad (4.24)$$

so,  $b = E(\infty) - E(0)$ . Taking the derivative of Equation 4.22 with respect to  $p$  yields:

$$E'(p) = \frac{b}{c} e^{-\frac{p}{c}}. \quad (4.25)$$

For  $p = 0$ :

$$E'(0) = \frac{b}{c}. \quad (4.26)$$

Thus,  $c$  is directly related to the rate of increase of  $E$  with respect to  $p$ . Values for the parameters were found to be:  $a = 61000$  MPa,  $b = 18920$  MPa, and  $c = 329.065$  MPa. Comparison between theoretical and experimental variation of  $E$  with the mean normal stress,  $p$ , is presented in Figure 4–5, where the solid line represents the theoretical model results. The correlation between theoretical and experimental values for  $E$  is excellent.

Values for the bulk modulus were taken from the slope of the unload-reload cycles of the volume strain versus mean normal stress curves, for both the hydrostatic and deviatoric phases of the Kármán experiments as discussed in Section 2.14. Results of the data analysis for  $K$  were presented in Figure 2–58. Though the experimentally determined values for  $K$  are in good agreement (with the exception of the first experiment conducted at 300 MPa confining pressure), due to the uncertainty in estimating  $K$ , it was decided to take a mean value of  $\nu = 0.175$  for the Poisson ratio and calculate  $K$  from the elasticity relationship:

$$K = \frac{E}{3(1 - 2\nu)} \quad (4.27)$$

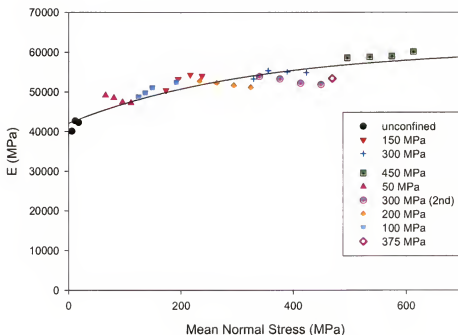


Figure 4-5: Young's modulus ( $E$ ) as a function of mean normal stress

Several other factors entered into the making of this decision. For the sake of simplicity in this first implementation of the model, it was seen as advisable to limit the number of coefficients involved in the model. Also, due to the overall higher level of confidence in the axial measurements, if possible it would be best to have  $E$  as the sole pressure dependent elastic function. The value selected for the mean Poisson's ratio is well within the range of values typically observed for concrete (see Neville [15]). Figure 4-6 presents the experimentally determined values for  $K$ , along with the function defined by Equation 4.27. The assumption of a constant Poisson's ratio was quite reasonable and resulted in a good match between the theoretical and experimental values.

The elastic-viscoplastic model as defined by Equation 4.15 does not explicitly use  $E$  in the formulation, rather the shear modulus ( $G$ ) is used. The shear modulus may be evaluated from the elasticity relationship:

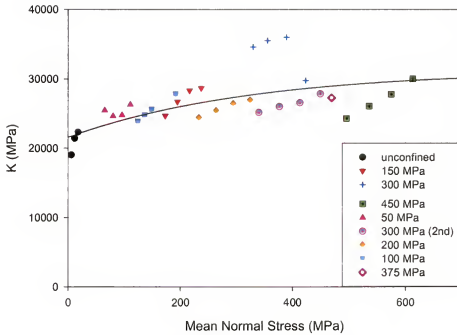


Figure 4-6: Bulk modulus ( $K$ ) as a function of mean normal stress

$$G = \frac{E}{2(1 + \nu)} \quad (4.28)$$

#### 4.5 Yield Function Evaluation

Recall that the irreversible deformation rate is given by:

$$\dot{\varepsilon}_{ij}^I = k_T \left\langle 1 - \frac{W(t)}{H(\sigma_{mn})} \right\rangle \frac{\partial F}{\partial \sigma_{ij}} \quad (4.29)$$

In the special case where the irreversible deformation rate approaches zero, Equation 4.29 becomes:

$$0 = k_T \left\langle 1 - \frac{W(t)}{H(\sigma_{mn})} \right\rangle \frac{\partial F}{\partial \sigma_{ij}} \quad (4.30)$$

Reducing further yields:

$$W(t) \leq H(\sigma_{mn}). \quad (4.31)$$

The corresponding stress state,  $\sigma_{mn}$ , belongs to the stabilization boundary. Such conditions, where the irreversible deformation rate approaches zero, occur in creep experiments. Thus, this boundary can be experimentally mapped out through a series of carefully controlled creep experiments. In a creep experiment, the stress state is kept constant for a certain interval while the strains are continuously measured. When the deformation over time practically stops, it can be assumed that a stabilized state has been reached. Figure 4-7 depicts how the stabilization boundary can be mapped out experimentally in a  $(\sigma, \varepsilon)$  plane. The stair-step line represents the loading and creep steps of such an experiment. In any given creep stage, the stress is held constant until the strain rate approaches zero. The stabilization boundary is defined by the stress-strain points taken at the end of each creep cycle.

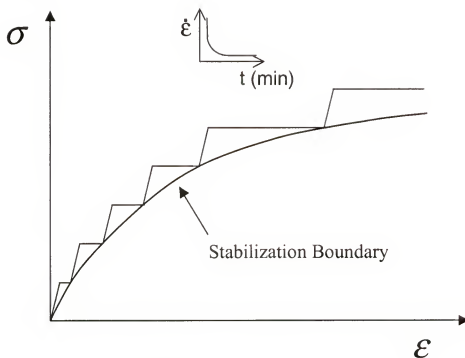


Figure 4-7: Stabilization boundary

The material being isotropic, the yield function,  $H$ , depends on  $\sigma_{ij}$  through it's invariants:

$$\mathbf{I}_1 \equiv (tr\sigma_{ij}), \quad (4.32)$$

$$\mathbf{J}_2 \equiv \frac{1}{2}(tr\sigma'_{ij})^2, \quad (4.33)$$

$$\mathbf{J}_3 \equiv \frac{1}{3}(tr\sigma'_{ij})^3, \quad (4.34)$$

where  $\mathbf{I}_1$  is the first stress invariant while  $\mathbf{J}_2$  and  $\mathbf{J}_3$  are the second and third invariants of the stress deviator. By definition,

$$p \equiv \frac{1}{3}(tr\sigma_{ij}) = \frac{1}{3}\mathbf{I}_1, \quad (4.35)$$

Let  $q$  be defined as:

$$q \equiv \sqrt{3}\mathbf{J}_2 = \sqrt{\frac{3}{2}\sigma'_{ij} : \sigma'_{ij}}, \quad (4.36)$$

For simplicity, let us assume that the influence of  $\mathbf{J}_3$  on  $H$  may be neglected, then  $H$  is a function of  $p$  and  $q$  only.

For the special case of a Kármán experiment,  $q$  reduces to the principal stress difference,  $q = \sigma_1 - \sigma_3$  and  $p = \frac{1}{3}(\sigma_1 + 2\sigma_2)$ . Let us assume that the yield function can be expressed as the sum of two terms:

$$H(p, q) = H_H(p) + H_D(p, q), \quad (4.37)$$

with

$$H_D(p, 0) = 0. \quad (4.38)$$

Hence,  $H_H$  and  $H_D$  are the hydrostatic and deviatoric contributions respectively.

Since under hydrostatic conditions, the yield function reduces to  $H_H(p)$ , it may be

determined directly from data obtained in the hydrostatic compression phase of the Kármán tests. Under hydrostatic loading,  $\sigma_{ij} = p\delta_{ij}$ , the irreversible stress work reduces to:

$$W(t) \equiv W_H(t) = \int_0^{t_H} p(t)\dot{\epsilon}_v^I(t)dt \quad (4.39)$$

Here,  $\dot{\epsilon}_v^I$  is the irreversible volume strain rate and  $t_H$  is the time corresponding to the end of the hydrostatic loading phase. Values for  $W(t)$  were calculated from the experimental data, and the points corresponding to the end of the creep cycles plotted as a function of mean normal stress. Results from the 150, 300, 450 and 500 MPa hydrostatic tests are presented in Figure 4–8.

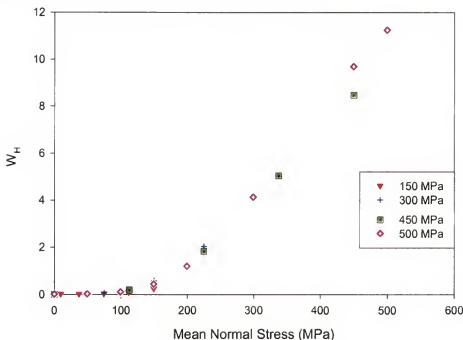


Figure 4–8: Irreversible hydrostatic work

The values for  $W_H$  are initially nearly zero, which is expected since the material is initially responding primarily elastically. At approximately 150 MPa mean normal stress, there is an upturn in the data after which the  $W_H$  increases almost linearly with increasing pressure. Eventually, as the pressure is continually increased, all of the microcracks and pores should close and the material will



achieve a fully compressed state and respond to increased hydrostatic loading as a perfectly elastic body. At this point, the curve should flatten out since with increasing pressure, further irreversible volumetric work will not be possible. This plateau obviously lies beyond the hydrostatic pressure limit of the equipment available for this modeling effort. In order to achieve higher pressure volumetric compression results, it may be necessary to utilize a uniaxial strain compression cell as described in Cristescu [8]. A cumulative symmetric double sigmoidal transition function was selected as providing the best match to the experimental data, as well as replicating the expected plateau for the fully compressed material behavior. The expression is shown below as Equation 4.40

$$H_H(p) = \frac{a_h}{2c_h} \left[ 2d_h \ln \left( \exp \left( \frac{2p + c_h}{2d_h} \right) + \exp \left( \frac{b_h}{d_h} \right) \right) - 2d_h \ln \left( \exp \left( \frac{p}{d_h} \right) + \exp \left( \frac{2b_h + c_h}{2d_h} \right) \right) + c_h \right] + e_h \quad (4.40)$$

where the coefficient “ $e_h$ ” assures zero intercept, “ $a_h$ ” defines the transition height, “ $b_h$ ” the transition center while the transition width is defined by the expression:

$$width = d_h \ln \left( 1 - \exp \left( \frac{3c_h}{4d_h} \right) \right) - d_h \ln \left( \exp \left( \frac{c_h}{4d_h} \right) - \exp \left( \frac{c_h}{4d_h} \right) \right) - d_h \ln \left( 1 - \exp \left( \frac{c_h}{4d_h} \right) \right) + d_h \ln \left( \exp \left( \frac{-c_h}{4d_h} \right) - \exp \left( \frac{c_h}{4d_h} \right) \right) \quad (4.41)$$

Figure 4-9 displays the experimental data along with the theoretical expression for  $H_H(p)$  evaluated using the parameter values:  $a_h = 12.602$  MPa,  $b_h = 364.272$  MPa,  $c_h = -364.935$  MPa,  $d_h = 30.696$  MPa, and  $e_h = 0.0028347$  MPa. These coefficients provided an excellent fit to the data with an  $r^2$  of 0.9998. The plateau level was selected rather arbitrarily by choosing what seemed a reasonable value and including a heavily weighted point of this value at 1 GPa mean normal stress. In order to fine tune the model, it would be highly desirable to acquire data at

confining pressures up to 1 GPa, and in close proximity to the two inflection points in the curve.

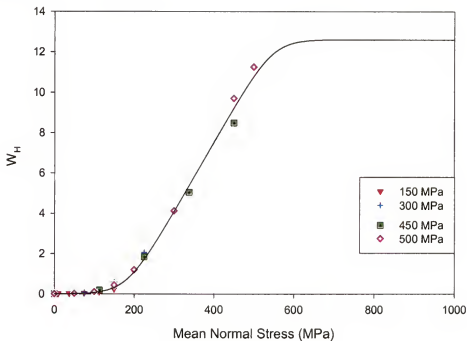


Figure 4-9: Hydrostatic yield function

In a similar manner, the deviatoric yield function ( $H_D$ ) is determined from the deviatoric phase of the Kármán experiments. In the deviatoric phase, the lateral confining pressure,  $\sigma_3$ , is held constant, while the axial stress,  $\sigma_1$ , is increased up to the point of material failure. The state of stress under these conditions is given in Equation 4.42.

$$\sigma_{ij}(t) = \begin{pmatrix} \sigma_1(t) & & \\ & \sigma_3 & \\ & & \sigma_3 \end{pmatrix}, \quad t \geq t_H \quad (4.42)$$

Under the experimental conditions, the irreversible stress work may be written:

$$W(t) \equiv W_D(t) = \int_{t_H}^t \sigma_3(t) \dot{\varepsilon}_v^I(t) dt + \int_{t_H}^t q(t) \dot{\varepsilon}_I^I(t) dt, \quad t \geq t_H. \quad (4.43)$$

$W_D$  was calculated for the deviatoric portions of each experiment. The values for  $W_D$  corresponding to the end of the creep cycles were then plotted as a function of  $q$  (see Figure 4–10). The result was a family of curves dependent on both  $q$  and the radial confining pressure  $\sigma_3$ . At any given confining pressure the data trend is the same: i.e. initially linear, eventually curving upward and asymptoting towards infinity as the specimen underwent failure. In order to capture this behavior, a function was selected which was a summation of linear, quadratic and exponential terms. Thus, for any given  $\sigma_3$ , the  $W_D$  vs.  $q$  curve was approximated with the function:

$$H_D(\sigma_3, q) = d_0q + d_1q^2 + d_2 \exp(d_3q^2) - d_2, \quad (4.44)$$

where  $d_i$  are the constants for a given test. The expression is shown to be a function of both  $\sigma_3$  and  $q$ , though only  $q$  is explicitly represented. The other term enters in that the 4 parameters from each of the curve fits, must now be expressed as a function of  $\sigma_3$ .

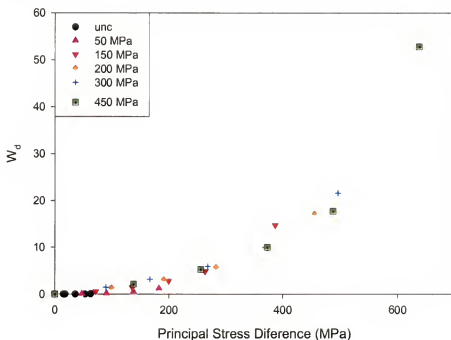


Figure 4–10: Deviatoric yield function

Next, each of the parameters ( $d_0$ ,  $d_1$ ,  $d_2$ , and  $d_3$ ) was plotted as a function of radial confining pressure. The following expressions were found to approximate the variation of these parameters as a function of confining pressure.

$$d_0(\sigma_3) = d_{0_a} \cdot (1 - \exp(d_{0_b}\sigma_3)) \quad (4.45)$$

$$d_1(\sigma_3) = d_{1_a} \cdot (1 - \exp(d_{1_b}\sigma_3)) \quad (4.46)$$

$$d_2(\sigma_3) = d_{2_a} + d_{2_b} \cdot (1 - \exp(d_{2_c}\sigma_3)) \quad (4.47)$$

$$d_3(\sigma_3) = \frac{d_{3_a}}{1 + d_{3_a} \cdot d_{3_b} \cdot \sigma_3} \quad (4.48)$$

Values for all the parameters given in Equations 4.45 through 4.48 are provided in Table 4-1.

Table 4-1: Parameter values for  $H_D$

$d_{0_a}$	$d_{0_b}$	$d_{1_a}$	$d_{1_b}$	$d_{2_a}$	$d_{2_b}$	$d_{2_c}$	$d_{3_a}$	$d_{3_b}$
0.0141	-0.007512	$4.08087 \cdot 10^{-5}$	-0.00489	$1.5935 \cdot 10^{-4}$	0.05640	-0.008213	0.00135	175.26

A comparison between the analytical model for the deviatoric yield function and the experimental results corresponding to 200 MPa confining pressure are presented in Figure 4-11. The 200 MPa experiment was not utilized in the determination of the the function, so it should provide an excellent test case. As can be seen, correlation between experiment and theory is excellent.

In order that the expression for  $H_D$  be as general as possible, it is desirable that it be expressed purely in terms of the stress invariants. Under the special conditions of the Kármán test,  $\sigma_3 = p - \frac{q}{3}$ . Thus in general terms, Equation 4.44 may be written:

$$H_D(p, q) = d_0 q + d_1 q^2 + d_2 \exp(d_3 q^2) - d_2. \quad (4.49)$$

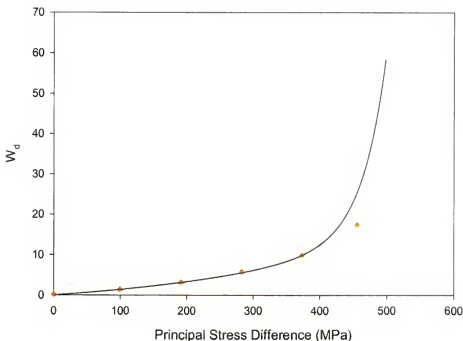


Figure 4-11: Deviatoric yield function compared to 200 MPa experiment

#### 4.6 Strain Rate Orientation Tensor

All elements of the model have now been formulated with the exception of the potential function,  $\frac{\partial F}{\partial \sigma_{ij}}$ . Determination of the viscoplastic potential function can be quite challenging and in some cases not possible. As an alternative, the concept of an irreversible strain rate orientation tensor was introduced by Cazacu [102]. Let us define  $N(\sigma_{ij})$  a tensorial function of the stress tensor which governs the orientation of the irreversible strain rate,  $\dot{\epsilon}_{ij}^I$ . For an isotropic material,  $N$  must satisfy the invariance requirement

$$N(Q\sigma_{ij}Q^T) = QN(\sigma_{ij})Q^T \quad (4.50)$$

where  $Q$  represents any orthogonal transformation. From classical results regarding the representation of isotropic tensor functions, it follows that  $N$  can be represented as,

$$N(\sigma_{ij}) = N_1 I + N_2 \sigma_{ij} + N_3 \sigma_{ij}^2 \quad (4.51)$$

where  $N_i$  are scalar-valued functions of the stress invariants. In order to reduce the complexity of the analysis, the simplifying assumption that the contributions of  $N_3$  and the third stress invariant are negligible is made. Thus, the expression for  $N$  reduces to:

$$N(\sigma_{ij}) = N_1(p, q)I + N_2(p, q)\frac{\sigma'_{ij}}{q}, \quad (4.52)$$

where  $I$  is the identity matrix (for more details, see [102]). The irreversible portion of the constitutive equation can now be written:

$$\dot{\varepsilon}_{ij}^I = k_T \left\langle 1 - \frac{W(t)}{H(\sigma_{ij})} \right\rangle \left\{ N_1(p, q)I + N_2(p, q)\frac{\sigma'_{ij}}{q} \right\} \quad (4.53)$$

For the special case of the triaxial Kármán experiment,  $\dot{\varepsilon}_2 = \dot{\varepsilon}_3$ . Writing out the individual terms of  $\dot{\varepsilon}_{ij}^I$  under these conditions yields:

$$\dot{\varepsilon}_1^I = k_T \left\langle 1 - \frac{W(t)}{H(\sigma_{ij})} \right\rangle \left\{ N_1(p, q) + \frac{2}{3}N_2(p, q) \right\} \quad (4.54)$$

$$\dot{\varepsilon}_3^I = k_T \left\langle 1 - \frac{W(t)}{H(\sigma_{ij})} \right\rangle \left\{ N_1(p, q) - \frac{1}{2}N_2(p, q) \right\}. \quad (4.55)$$

Combining Equations 4.54 and 4.55 in order to isolate the  $N_1$  and  $N_2$  terms yields:

$$\dot{\varepsilon}_v^I = 3k_T \left\langle 1 - \frac{W(t)}{H(\sigma_{ij})} \right\rangle \{N_1(p, q)\} \quad (4.56)$$

$$|\dot{\varepsilon}_1^I - \dot{\varepsilon}_3^I| = k_T \left\langle 1 - \frac{W(t)}{H(\sigma_{ij})} \right\rangle \{N_2(p, q)\}. \quad (4.57)$$

Rearranging Equations 4.56 and 4.57, expressions for  $k_T N_1$  and  $k_T N_2$  can be written strictly in terms that are either measurable, or previously determined in a

Kármán experiment.

$$k_T N_1(p, q) = \frac{\dot{\varepsilon}_v^I}{3 \left\langle 1 - \frac{W(t)}{H(\sigma_{ij})} \right\rangle} \quad (4.58)$$

$$k_T N_2(p, q) = \frac{|\dot{\varepsilon}_1^I - \dot{\varepsilon}_3^I|}{\left\langle 1 - \frac{W(t)}{H(\sigma_{ij})} \right\rangle} \quad (4.59)$$

The form of Equation 4.58 indicates that  $N_1$  controls the irreversible volumetric response, while  $N_2$  (Equation 4.59) will control the irreversible shear response. The  $k_i N_1$  term may be thought of as consisting of a hydrostatic and deviatoric part as indicated in Equation 4.60.

$$k_T N_1(p, q) = \phi(p) + \psi(p, q) \quad (4.60)$$

Equation 4.58 is utilized, along with data from the hydrostatic compression phase of the experiments to determine  $\phi(p)$ . Figure 4–12 presents results calculated from the experiments conducted at 50, 200, 375, and 500 MPa hydrostatic confinement. There is a high level of correlation between the three monotonically conducted experiments. The 500 MPa experiment was conducted with a number of creep cycles. Due to the nature of the expression, within the creep cycle, a numerical singularity would occur as the material approached creep stabilization (i.e.  $W(t) = H(\sigma_{ij})$ ). Thus the data presented for this experiment has had the creep and unload cycles removed. For each cycle, following an initial “ramp up”, the material appears to follow the same surface as the monotonic experiments. The data from the 375 MPa experiment increases monotonically, while for the final displayed cycle of the 500 MPa experiment, the data appears to level out. As was discussed in the derivation of the hydrostatic yield function,  $H_H$ , as the mean normal stress is increased, eventually the material will reach a fully compacted state where no further plastic deformation is possible. This state is indicated by the plateau on the

$H_H$  curve (Figure 4-9). In this fully compressed state  $\dot{\varepsilon}_v^I = 0$ , thus, the expression for  $\phi(p)$  should peak and then begin to fall returning to zero. Assuming the plateau for  $H_H$  was estimated correctly,  $\dot{\varepsilon}_v^I$  should achieve a value of zero at approximately 600 MPa and remain zero for  $p \geq 600 \text{ MPa}$ . Figure 4-13 displays the values of  $\dot{\varepsilon}_v^I(p)$  for the 375 MPa and 500 MPa hydrostatic compression experiments. Correlation between these two experiments is remarkably good. The value for  $\dot{\varepsilon}_v^I$  reaches a peak value at approximately 290 MPa, and begins to plateau for a period, and then fall. The agreement in  $\dot{\varepsilon}_v^I$  between the two experiments gives one confidence that the leveling of the  $\phi(p)$  results is real. It also lends confidence that the estimation of the plateau in  $H_H$  is reasonable, since the rate of volumetric compression has begun to slow approximately half way into the linear portion of the function. In order to mathematically model such behavior, it would likely be necessary to resort to a two part expression, one for increasing  $\phi(p)$  and one for decreasing values. Due to the lack of data, the shape of the descending function would be pure conjecture. Therefore, at this point, the decision was made to model the behavior with a single smooth continuous function which asymptotes to a constant value corresponding to the plateau indicated in the experimental data. A sigmoid function of the form:

$$\phi(p) = \phi_0 + \frac{\phi_1}{1 + \exp \left[ -\frac{p - \phi_2}{\phi_3} \right]} \quad (4.61)$$

was found to approximate the data well, where:  $\phi_0 = -7.163\text{e-}5$ ,  $\phi_1 = 0.008137$ ,  $\phi_2 = 295.866$ , and  $\phi_3 = 62.632$ . Only the data from the 375 MPa experiment and the 450 MPa cycle of the 500 MPa hydrostatic experiment were utilized to determine  $\phi_0$  to  $\phi_3$ . A comparison of the model results to the experimental data is given in Figure 4-14.

To determine  $\psi(p, q)$ , Equation 4.58 along with the data from the deviatoric shear portion of the experiments were used. Results for the 200 MPa experiment are presented in Figure 4-15. Once again, only the results from the monotonic



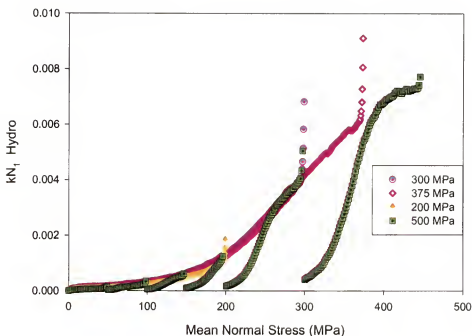


Figure 4-12: Strain rate orientation tensor -  $kN_1$  hydro

loading cycles are included. The first loading cycle shows a clear monotonically increasing trend in the data, however, on subsequent reload cycles, there does not appear to be sufficient spacing between the creep cycles for the specimen to ever reach the “surface” upon reloading. If it does reach the surface, it is only very shortly prior to initiation of the subsequent creep phase. On the final cycle, the material ramps up only slightly, then transitions to a negative slope, eventually becoming negative. Close inspection of the value for  $q$  at the point  $kN_1$  crosses the  $q$  axis indicated it corresponds to the transition from compressibility to dilatancy indicated in the volume strain curve (Figure 2-40). The data as presented does not appear to be adequate for selecting a suitable function representative of  $\psi(p, q)$ . What can be deduced from the trends in the data, and the characteristics of Equation 4.58 is that the function should initially increase with positive slope, reach a transition peak where the slope becomes negative, and then achieve negative value at a point corresponding to the compressibility-dilatancy boundary.

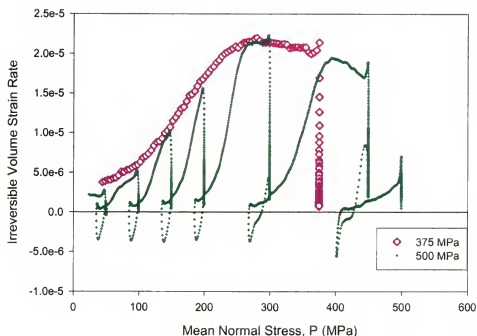


Figure 4-13: Irreversible volumetric strain rate

Finally,  $k_T N_2(q, p)$  was determined by utilizing Equation 4.59 along with data from the deviatoric shear experiments. Results for the 200 MPa analysis are presented in Figure 4-16. Once again, after the first loading cycle, the data on subsequent reload cycles does not clearly indicate a  $k_T N_2$  surface. It does appear however that a monotonically increasing function would adequately represent the material behavior.

Ideally, in order to adequately determine  $\psi(p, q)$ , several monotonic deviatoric experiments should have been included in the experimental matrix. Under the assumption that adequate information is available within the experimental data, a process was devised and utilized in an attempt to extract the information. The 375 MPa test was initially chosen for analysis since it only contained one creep-unload-reload cycle. The process began by first extracting all of the data rows containing the creep cycles from the data set. Ideally, a monotonic experiment conducted under load control would have a very nearly linear principal stress difference vs. time loading profile. Simply removing the creep-unload-reload cycles, yielded

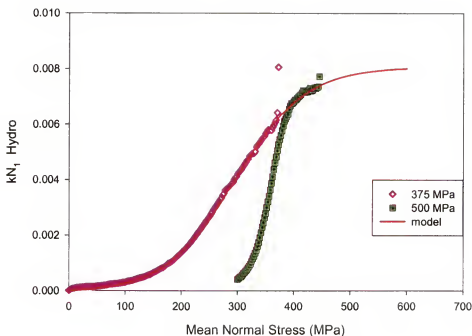


Figure 4-14: Comparison of data to model for kN1 hydro

two linear sections offset by time. A correction was made to the time column by subtracting out the time period over which the creep-unload-reload cycle was conducted from the second linear portion. This resulted in a very nearly linear data set (see Figure 4-17). This resultant data set was subsequently curve fit as a function of time. The fine line in Figure 4-17 represents the curve fit data.

Following this step, both the axial and radial strains were plotted as a function of time. Further data rows were subjectively removed in order to provide a smooth data set for curve fitting. The axial and radial strains were plotted as a function of time and a complete set of monotonic data was subsequently constructed. Figure 4-18 contains the results for the axial strain. Both the original data set, as well as the retained adjusted data are presented. The fine line represents the constructed monotonic axial strain as a function of constructed principal stress difference.

Using this adjusted data set, values for  $\psi(p, q)$  and  $k_T N_2$  were calculated. The results are presented in Figures 4-19 and 4-20. The new data set for  $\psi(p, q)$  captures the expected features including the expected peak and slope transition, with

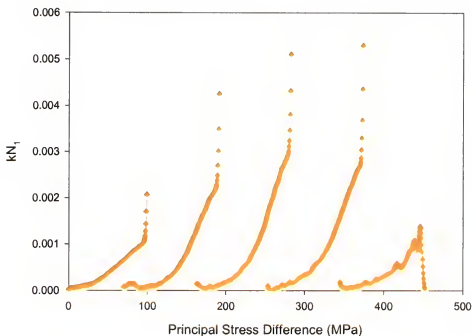


Figure 4-15: Strain rate orientation tensor -  $kN_1$  deviatoric, 200 MPa experiment

a sign change of  $\psi(p, q)$  from positive to negative corresponding the compressibility-dilatancy transition point. The  $k_T N_2$  results exhibit the monotonically increasing function predicted.

Finally, Figures 4-21 and 4-22 contain the results for  $\psi(p, q)$  and  $k_T N_2$  from the original and adjusted data sets. The results in both cases indicate that the adjusted data set accurately replicates the trends indicated in the original experimental data and is of suitable quality for function evaluation. This same data analysis technique was subsequently employed on all of the deviatoric shear experiments.

The results of the deviatoric  $\psi$  evaluations from all adjusted data sets are shown in Figure 4-23. Positive  $\psi$  corresponds to compressible response of the material, while negative  $\psi$  indicates dilatant behavior. The results indicate a family of curves with clear pressure dependency. Due to scaling, it is very difficult to see the the unconfined response in Figure 4-23. Figures 4-24 and 4-25 present the unconfined results in detail. From these two figures, it can be concluded that

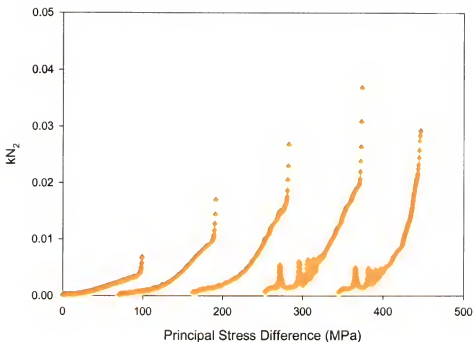


Figure 4-16: Strain rate orientation tensor - kN<sub>2</sub>, 200 MPa experiment

the unconfined compression test is largely a dilatant event with only very little early compressibility. The shape of the compressive portion of the curve from the 50 MPa experiment does not correlate well with the other experiments. There is insufficient data in this pressure regime to indicate whether this is truly indicative of the material behavior, or whether it is an experimental anomaly. Therefore, the decision was made not to utilize the compressive data from this experiment in the subsequent parameter fits. In all the experiments, there were three obvious phases consistently observed, a pre-peak compression phase, post-peak compression and a dilatant phase. It would be very difficult to derive a function capable of replicating this complex behavior, much less hope to determine the variation of the coefficients of such a function with mean pressure. Consequently, the decision was made to model each phase separately. There are three points which might be thought to bound the compressive domain, the origin, the location of the maximum value of  $\psi$ , and the compressibility-dilatancy boundary. Any function chosen to represent  $\psi$  must pass through these points. Let  $\beta$  be defined as the peak value of  $\psi$  for any

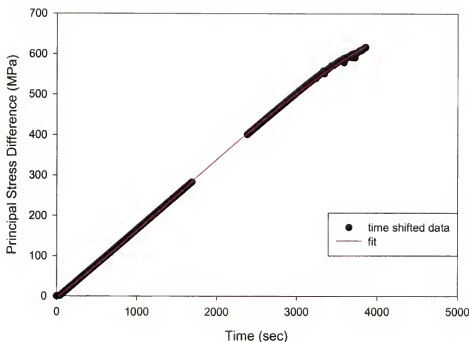


Figure 4-17: Time adjusted loading profile

given confining pressure. Figure 4-26 presents the values of  $\beta$  as a function of the confining pressure, denoted by  $\chi$ . A rational function of the form:

$$\beta(p, q) = \frac{(\beta_0 + \beta_1 \chi)}{(1 + \beta_2 \chi)} + \beta_3 \quad (4.62)$$

approximates well the variation of  $\beta$  with  $\chi$  for  $\beta_0 = 0.000002073$ ,  $\beta_1 = 0.0000335$ ,  $\beta_2 = 0.003967$ , and  $\beta_3 = 0.00000171$ . The solid line in Figure 4-26 represents the theoretical predictions obtained using Equation 4.62, whereas data from the different experiments are represented by symbols.

Let  $\gamma$  be defined as the value of  $q$  at which the peak value of  $\psi$  occurs for any given  $\chi$ . Figure 4-27 displays the values of  $\gamma$  as a function of  $\chi$  for the different Kármán experiments conducted. A simple expression of the form:

$$\gamma(p, q) = \gamma_0 \chi^{\gamma_1} + \gamma_2 \quad (4.63)$$

was found to approximate the data quite well. The solid line in Figure 4-27 indicates the theoretical results given by Equation 4.63. The numerical values of

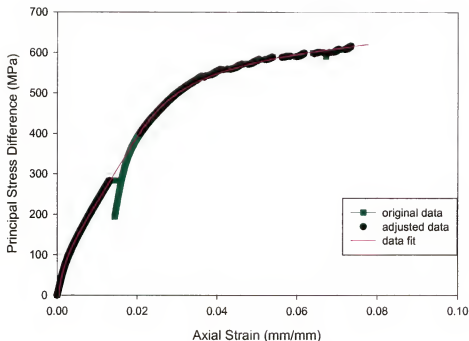


Figure 4-18: Adjusted axial strain results - 375 MPa experiment

the parameters for Equation 4.63 were found to be:  $\gamma_0 = 7.98$ ,  $\gamma_1 = 0.699$ , and  $\gamma_2 = 1.794$ .

The data defining the compressibility-dilatancy (C/D) boundary is presented in Figure 4-28. The data points were taken as the value of  $q$  at which  $\psi$  transitioned from positive to negative for a given value of  $\chi$ . An exponential expression of the form given in Equation 4.64 was found to approximate the data well.

$$\alpha(p, q) = \alpha_0 + \alpha_1 (1 - \exp[-\alpha_2 \chi]) \quad (4.64)$$

The solid line in Figure 4-28 represents the theoretical values of the C/D boundary. The numerical values of the coefficients involved in Equation 4.64 were found to be:  $\alpha_0 = 3.596$ ,  $\alpha_1 = 590.055$ , and  $\alpha_2 = 0.0070659$ .

A Gaussian expression of the form:

$$\psi_{C_1}(p, q) = \psi_0 + \psi_1 \exp \left[ -\frac{1}{2} \left( \frac{q - \psi_2}{\psi_3} \right)^2 \right] \quad (4.65)$$

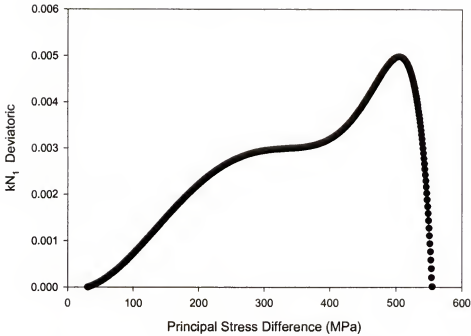


Figure 4-19: Strain rate orientation tensor - kN1, 375 MPa experiment

was chosen to approximate the pre-peak response of  $\psi$  and was found to match the experimental data well. The variable  $\psi_{C_1}$  is defined as the pre-peak behavior of  $\psi$ . The Gaussian is a symmetric-peak function where,  $\psi_0$  is a parameter controlling the functions  $y$  intercept,  $\psi_1$  is related to the amplitude of the function,  $\psi_2$  defines the location of the functions peak value, while the overall area is defined by  $\sqrt{2\pi}\psi_1\psi_3$ . The rational expression:

$$\psi_1(p, q) = \frac{(\psi_{1_a} + \psi_{1_b}\chi)}{(1 + \psi_{1_c}\chi)} + \psi_{1_d} \quad (4.66)$$

was chosen to approximate  $\psi_1$ . The numerical values of the parameters were determined to be:  $\psi_{1_a} = 0.00003392$ ,  $\psi_{1_b} = 0.00003598$ ,  $\psi_{1_c} = 0.003899$ , and  $\psi_{1_d} = 0.00000438$ . Note that

$$\psi_0(p, q) = \beta(p, q) - \psi_1(p, q) \quad (4.67)$$



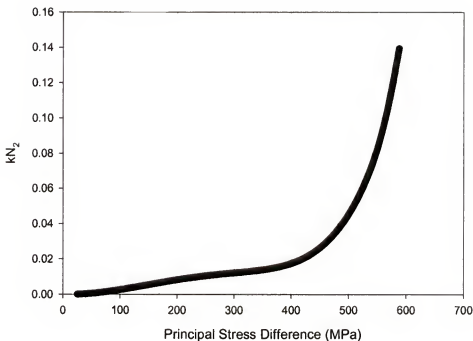


Figure 4-20: Strain rate orientation tensor - kN<sub>2</sub>, 375 MPa experiment

while

$$\psi_2(p, q) = \gamma(p, q) \quad (4.68)$$

. Thus, both functions  $\psi_0$  and  $\psi_2$  are fully determined without the introduction of any additional parameters. The final parameter,  $\psi_3$ , was modeled using the simple expression:

$$\psi_3(p, q) = \psi_{3a} \chi^{\psi_{3b}} + \psi_{3c}, \quad (4.69)$$

where  $\psi_{3a} = 1.95$ ,  $\psi_{3b} = 0.79$ , and  $\psi_{3c} = 13$ .

The post-peak response of  $\psi$  is given by Equation 4.70, the identical form of expression utilized for the pre-peak response (Equation 4.65). This had the effect of minimizing the number of new parameters required.

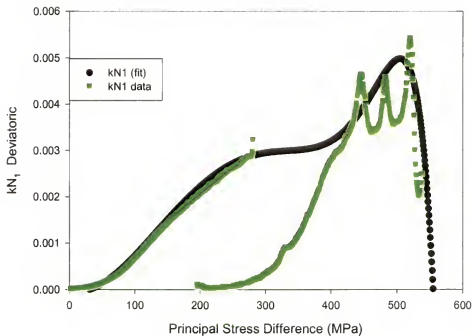


Figure 4-21: Comparison of analytical to experimental results - kN1, 375 MPa experiment

$$\psi_{C2}(p, q) = \psi_4 + \psi_5 \exp \left[ -\frac{1}{2} \left( \frac{q - \psi_6}{\psi_7} \right)^2 \right] \quad (4.70)$$

The variable  $\psi_{C2}$  is defined as the post-peak behavior of  $\psi$ , where

$$\psi_5(p, q) = \beta(p, q) \quad (4.71)$$

and

$$\psi_6(p, q) = \gamma(p, q). \quad (4.72)$$

Since  $\psi$  must cross the  $q$  axis at the point corresponding to the compressibility/dilatancy boundary, using Equations 4.70 to 4.72 it follows that  $\psi_4$ , is expressed as:

$$\psi_4(p, q) = \beta(p, q) - \frac{\beta(p, q)}{1 - \exp \left[ -\frac{1}{2} \left( \frac{\alpha(p, q) - \gamma(p, q)}{\psi_7} \right)^2 \right]} \quad (4.73)$$

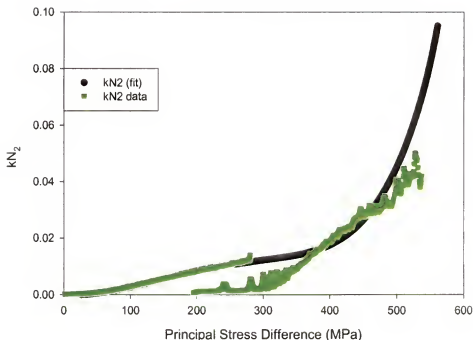


Figure 4-22: Comparison of analytical to experimental results - kN2, 375 MPa experiment

A constant value of  $\psi_7 = 5000$  MPa was determined to adequately represent all the data. Thus, the entire post-peak response was modeled with the introduction of only one additional parameter.

Now only the dilatant portion of  $\psi$  remains to be modeled. Looking again at Figure 4-23, there are only a limited number of experiments with valid dilatant  $\psi$  data. There is an obvious difference in behavior however at low and high pressures. Recall for a moment the volume strain curves from the deviatoric experiments of Chapter 2. Under uniaxial conditions and low confining pressures, WES5000 exhibited a gradual transition from compressibility to dilatancy, with a significant portion of the experiment conducted under dilatant conditions. At higher pressures (300 MPa and greater), the onset of dilatancy only occurred very near specimen failure. An analogous response is again apparent for the dilatant  $\psi$  behavior. In the unconfined experiment, the dilatant values of  $\psi$  display a gradual, monotonic negative trend with asymptotic behavior near failure (Figure 4-24). This initial

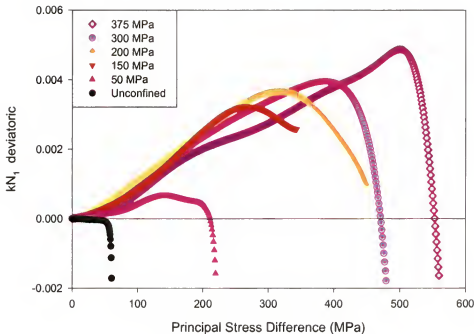


Figure 4-23: Strain rate orientation tensor -  $\psi$

monotonic behavior corresponds to the gradual dilatant deformation of the material. The higher pressure tests at 375 MPa and 450 MPa radial confinement displayed almost immediate asymptotic behavior, corresponding to the onset of dilatancy only very near failure. A function of the form:

$$\psi_D(p, q) = \frac{\psi_8 (q - \alpha(p, q))}{1 - \frac{q}{\psi_9}} \quad (4.74)$$

was chosen to model the behavior. The variable  $\psi_D$  is defined as the dilatant behavior of  $\psi$ . Parameter  $\psi_8$  acts to control the initial slope of the response, while  $\psi_9$  controls the asymptotic behavior. The simple linear expression:

$$\psi_8(p, q) = \psi_{8a}\chi + \psi_{8b} \quad (4.75)$$

was found to be adequate for modeling  $\psi_8$ , where  $\psi_{8a} = -1.1996e^{-7}$  and  $\psi_{8b} = -3.04e^{-7}$ . Parameter  $\psi_9$  was modeled using a rational function of the form:

$$\psi_9(p, q) = \frac{\psi_{9a} + \psi_{9b}\chi}{1 + \psi_{9c}\chi}. \quad (4.76)$$

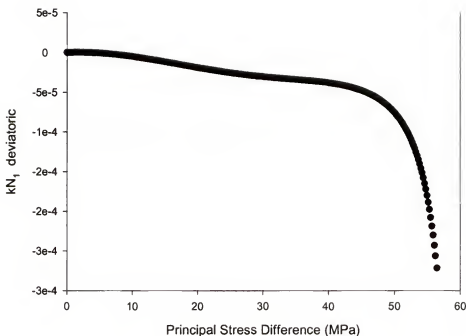


Figure 4-24: Strain rate orientation tensor -  $\psi$ , unconfined experiment

Close correlation to the experimental data was achieved using the values  $\psi_{g_a} = 60$ ,  $\psi_{g_b} = 4.3166578$ , and  $\psi_{g_c} = 0.004298336$ . All three phases of  $\psi$  have now been modeled. Comparisons of the theoretical results for  $\psi$  to the experimental data are presented in Figures 4-29 through 4-31. Figure 4-29 displays the compressive domain of  $\psi$  for the unconfined experiment. The theoretical and experimental results are seen to match almost exactly. Figure 4-30 shows the complete range of unconfined  $\psi$  results, both experimental and theoretical. The theoretical results again compare quite well, capturing both the quasi-linear and asymptotic behavior. Figure 4-31 presents the theoretical and experimental results for the 375 MPa radial confinement experiment. The overall shape of the 375 MPa  $\psi$  results, in particular the inflection occurring at  $\chi \approx 200$  MPa, is not considered to be truly indicative of material behavior. This is likely an artifact of the creep step present in the actual experiment. Still, the model adequately represents the material behavior, in particular the peak, slope transition and subsequent asymptotic dilatant response.

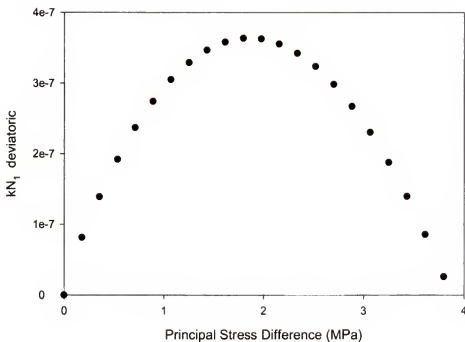


Figure 4-25: Strain rate orientation tensor -  $\psi$ , unconfined experiment low PSD range

The complete function for all three phases is presented below in Equation 4.77.

$$\begin{aligned}
 \psi(p, q) &= \psi_{C_1}, \quad q \leq \gamma(p, q) \\
 &= \psi_{C_2}, \quad \gamma(p, q) < q \leq \alpha(p, q) \\
 &= \psi_D, \quad \alpha(p, q) < q
 \end{aligned} \tag{4.77}$$

The  $kN_2$  term is the only constitutive function yet to be determined. Figure 4-32 displays the global  $kN_2$  at various confining pressures, while Figure 4-33 displays only the data for  $q \leq 300$  MPa. What is seen are a family of monotonically increasing curves with asymptotic behavior near failure. Closer inspection of Figure 4-33 shows that for lower levels of confinement (0 to 150 MPa) the slope of  $kN_2$  vs. PSD increases along with increasing confinement. Beyond confining levels of 150 MPa however, the slopes decrease with increasing confinement. The transition appears to take place for  $\chi \approx 200$  MPa. This corresponds closely with the inflection

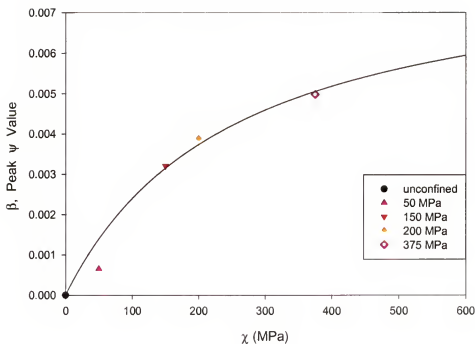


Figure 4-26: Peak  $\psi$  value as a function of  $\chi$

point in the hydrostatic yield function (Figure 4-9), thus what is seen is likely the result of the breaking of the cementation bonds in the concrete.

The low  $q$  range (pre-asymptote, quasi-linear) response was found to be adequately approximated with the function:

$$kN_2(p, q) = \xi_0 q^{1.5}. \quad (4.78)$$

The values of  $\xi_0$  were determined for the different confining conditions. The results are displayed as a function of confinement ( $\chi$ ) in Figure 4-34. The data trend indicates a positively sloped function which peaks in value at approximately  $\chi = 200$  MPa, then begins to decrease in value, and finally plateaus to a constant value. The plateau would correspond to the fully compacted state of the material. Once again, the behavior observed is very complex.

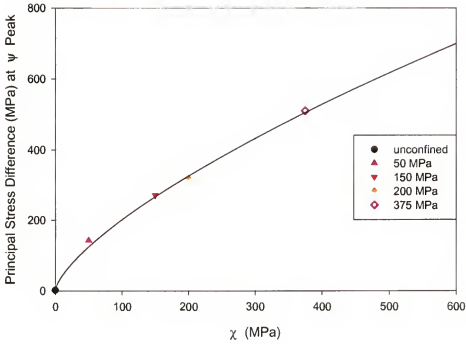


Figure 4-27: Principal stress difference at peak  $\psi$  as a function of  $\chi$

The pre-peak behavior could be modeled using a symmetric peak function such as a Lorentzian:

$$\xi_0^{(1)}(p, q) = \xi_{0a} + \frac{\xi_{0b}}{\left(1 + \left(\frac{\chi - \xi_{0c}}{\xi_{0d}}\right)^2\right)}, \quad (4.79)$$

where  $\xi_{0a}$  controls the  $y$  intercept of the function,  $\xi_{0b}$  determines the amplitude,  $\xi_{0c}$  the center, while the area is determined by  $\pi\xi_{0b}\xi_{0d}$ . The superscript (1) applied to the  $\xi_0$  variable is used here to designate the Lorentzian approximation to the data. The values for the parameters were determined to be:  $\xi_{0a} = -2.1396e^{-5}$ ,  $\xi_{0b} = 2.4650e^{-5}$ ,  $\xi_{0c} = 200$ , and  $\xi_{0d} = 641.5082$ .

Theoretical results are displayed in Figure 4-35 along with the experimental values. The theoretical model ( $\xi_0^{(1)}$ ) matches the pre-peak data quite well, and doesn't begin to deviate significantly until  $\chi = 375$  MPa. The  $\xi_0$  values have been extrapolated out to 1 GPa by assuming a constant value is achieved for  $\xi_0$  corresponding to the plateau in the hydrostatic yield function. Let  $\xi_0^{(2)}$  be defined



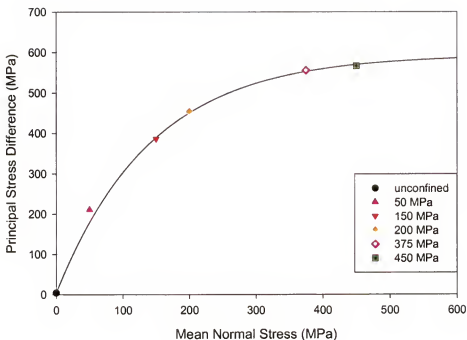


Figure 4-28: Compressibility - dilatancy boundary

as:

$$\xi_0^{(2)}(p, q) \equiv \xi_0^1 - \xi_0. \quad (4.80)$$

The resultant  $\xi_0^{(2)}$  data is plotted in Figure 4-36 along with the original  $\xi_0$  values.

The post-peak behavior of  $\xi_0^{(2)}$  displays monotonic behavior which is modeled quite well using a Pulse Cumulative function of the form:

$$\xi_0^{(2)}(p, q) = \xi_{0e} + \xi_{0f} \left( 1 - \exp \left[ - \frac{\chi - \xi_{0e} - \xi_{0h} \ln \left( 1 - \frac{\sqrt{2}}{2} \right) - \xi_{0g}}{\xi_{0h}} \right] \right)^2, \quad (4.81)$$

where  $\xi_{0e}$  controls the  $y$  intercept of the function,  $\xi_{0f}$  defines the transition height,  $\xi_{0g}$  defines the transition center, while the transition width is given by  $1.3169578969 \cdot \xi_{0h}$ . The function is subject to the constraint:

$$\xi_0^{(2)} = 0 \quad \text{for} \quad \chi < \xi_{0g} + \xi_{0h} \ln \left( 1 - \frac{\sqrt{2}}{2} \right) + \xi_{0e}. \quad (4.82)$$

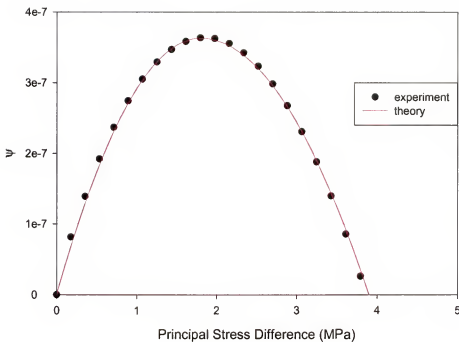


Figure 4-29: Theoretical  $\psi$  compared to unconfined experimental data, compressive domain

The values of the parameters in Equation 4.81 were determined to be:  $\xi_{0_e} = 3.6924e^{-9}$ ,  $\xi_{0_f} = -2.1373e^{-5}$ ,  $\xi_{0_g} = 612.7689$ , and  $\xi_{0_h} = 441.1152$ . Substituting these parameters into Equation 4.82 yields the constraint that  $\xi_0^{(2)} = 0$  for  $\chi < 271.10$ .

In order to implement this constraint, the concept of a unit step function shall be introduced. Let  $U[g]$  define a function of the argument  $g$  such that:

$$\begin{aligned} U[g] &= 1, \quad g \geq 0 \\ U[g] &= 0, \quad g < 0 \end{aligned} \quad (4.83)$$

Rearranging the terms in Equation 4.80 and incorporating the step function  $U$ , yields the expression:

$$\xi_0(p, q) = \xi_0^{(1)} - U \left[ \chi - \xi_{0_g} + \xi_{0_h} \ln \left( 1 - \frac{\sqrt{2}}{2} \right) + \xi_{0_e} \right] \cdot \xi_0^{(2)}. \quad (4.84)$$

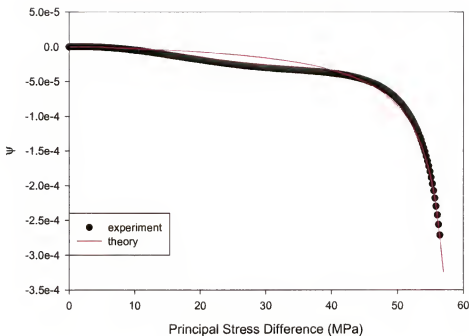


Figure 4-30: Theoretical  $\psi$  compared to unconfined experimental data

A comparison of the theoretical results yielded by Equation 4.84 to the experimental data is shown in Figure 4-37. In general, agreement between the two is excellent.

Now the asymptotic behavior of  $kN_2$  must be incorporated. The expression presented in Equation 4.85 was selected to model the experimental data.

$$kN_2(p, q) = \xi_0 q^{1.5} + \left(1 - \exp\left[-\frac{q - \xi_1}{\xi_3}\right]\right) U(q - \xi_1) \left(\frac{q - \xi_1}{1 - \frac{q}{\xi_2}}\right) \quad (4.85)$$

The  $\xi_0 q^{1.5}$  term is included to model the initial behavior previously discussed. The concept of the unit step function was again utilized to “turn on” the asymptotic behavior, therefore  $\xi_1$  determines the point at which the behavior is initiated, while parameter  $\xi_2$  determines the asymptote. The exponential term is introduced to smooth out the onset of the step function. Parameter  $\xi_3$  therefore controls the transition to asymptotic behavior. The obvious constraint is  $\xi_1 < \xi_2$ . A rational

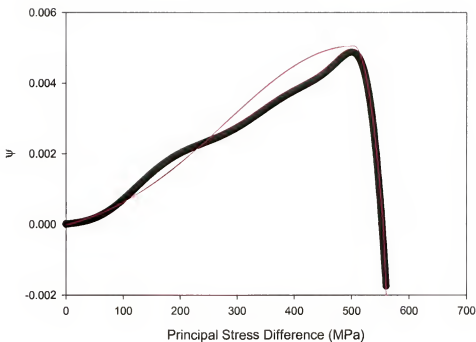


Figure 4-31: Theoretical  $\psi$  compared to 375 MPa experimental data

expression was again utilized to model the  $\xi_2$  response.

$$\xi_2(p, q) = \frac{(\xi_{2a} + \xi_{2b}\chi)}{(1 + \xi_{2c}\chi)} \quad (4.86)$$

The parameter values which yielded the best results are:  $\xi_{2a} = 61.6240$ ,  $\xi_{2b} = 2.8868$ , and  $\xi_{2c} = 0.0017699$ .

An Extreme Value Cumulative expression was chosen to model the  $\xi_1$  behavior. Given the limited data set available, it seemed to yield the best combination of accuracy, while achieving the constraint that  $\xi_1 < \xi_2$ .

$$\xi_1(p, q) = \xi_{1a} \exp \left[ -\exp \left[ -\frac{\chi - \xi_{1c} \ln(\ln(2)) - \xi_{1b}}{\xi_{1c}} \right] \right] \quad (4.87)$$

The parameters values for Equation 4.87 were evaluated as:  $\xi_{1a} = 414.1011$ ,  $\xi_{1b} = 67.8311$ , and  $\xi_{1c} = 61.0303$ . Figure 4-38 presents the theoretical results of  $\xi_1$  and  $\xi_2$ , as well as the respective experimental results. The  $\xi_1$  data indicates that the asymptote initiation point tends to level off for higher values of  $\chi$ .

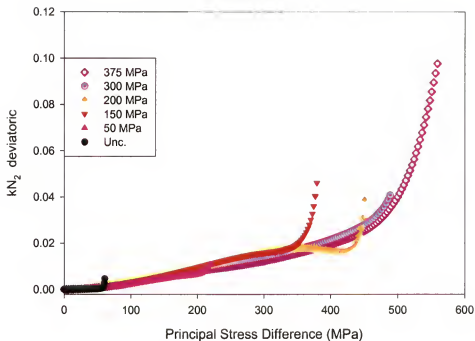


Figure 4-32: Strain rate orientation tensor -  $kN_2$

This is consistent with the results found for the C/D boundary behavior (see Figure 4-28). There is no experimental data at the lower confining pressures to determine whether the low- $\chi$  response is representative, however the results appear reasonable.

Finally, the findings for  $\xi_3$  again indicated the possibility of a “peak” type response similar to  $\xi_0$ . However, there was insufficient valid data to fully map out this behavior. Further study showed that the accuracy of results yielded by Equation 4.85 appeared to be rather insensitive to the value of  $\xi_2$  provided it was of the proper order of magnitude. An average value found from the  $\chi = 0, 150$  and 375 MPa results was consequently used ( $\xi_3 = 1881464$ ).

Figures 4-39, 4-40, and 4-41 present the  $kN_2$  experimental data along with the respective theoretical results. In each case, correlation between theory and experiment is excellent.

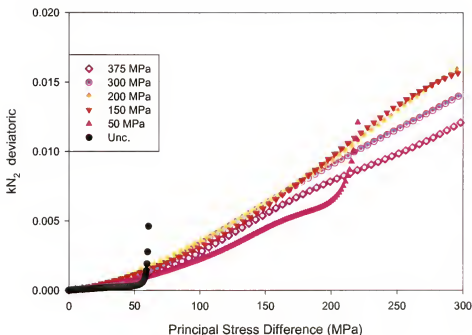


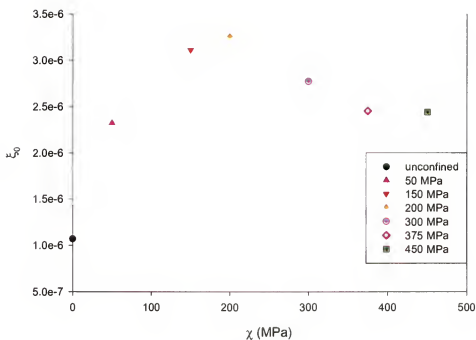
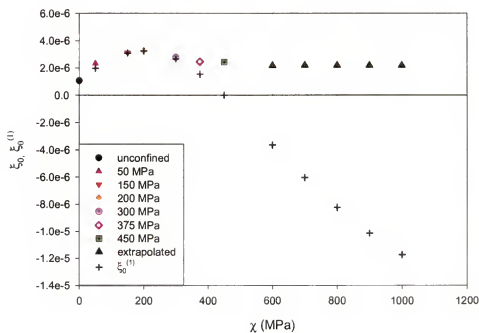
Figure 4-33: Strain rate orientation tensor -  $kN_2$ , low PSD range

#### 4.7 Comparison of Theoretical to Experimental Results

Analytic simulations were run for three different cases, uniaxial compression, monotonic hydrostatic compression up to 375 MPa mean normal stress, and a monotonic deviatoric case with 375 MPa confining pressure. For each case, comparisons are made to experimental data. Figure 4-42 presents both theoretical and experimental results for the uniaxial compression case. The model matches the data quite well and captures both the compressible and dilatant nature of the material as well as accurately predicting material failure.

Results for the 375 MPa hydrostatic compression case are presented in Figure 4-43. Correlation between experimental and analytic results is excellent, with the analytic results literally falling between the experimental axial and radial results.

Finally in the third case, the deviatoric analytic and experimental results are presented for 375 MPa confinement. Again, there is excellent agreement between theoretical and experimental axial, radial and volumetric strains. Compressibility, dilatancy and failure are all accurately simulated.

Figure 4-34: Parameter  $\xi_0$  as a function of  $\chi$ Figure 4-35: Parameters  $\xi_0$  and  $\xi_0^{(1)}$  as a function of  $\chi$

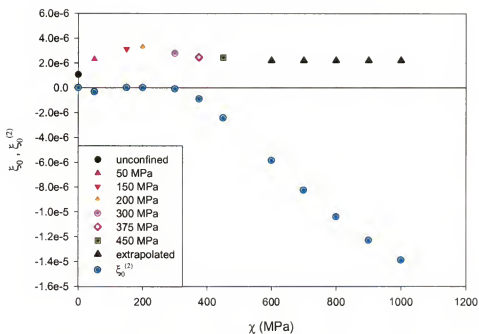


Figure 4-36: Parameters  $\xi_0$  and  $\xi_0^{(2)}$  as a function of  $\chi$

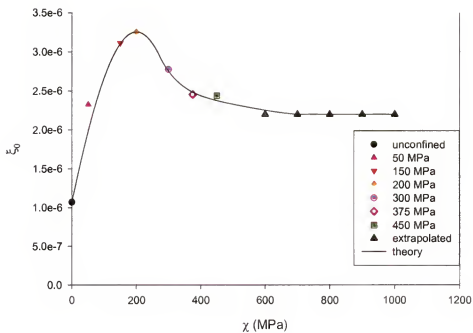


Figure 4-37: Theoretical  $\xi_0$  compared to experimental data



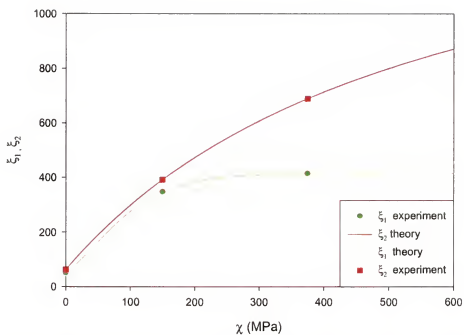


Figure 4-38: Parameters  $\xi_1$  and  $\xi_2$ , comparison of experimental and theoretical results

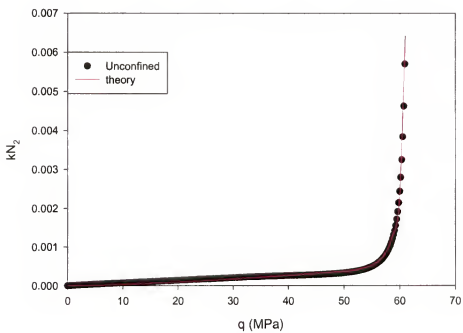


Figure 4-39: Experimental/theoretical comparison of  $kN_2$ ,  $\chi = 0$  MPa

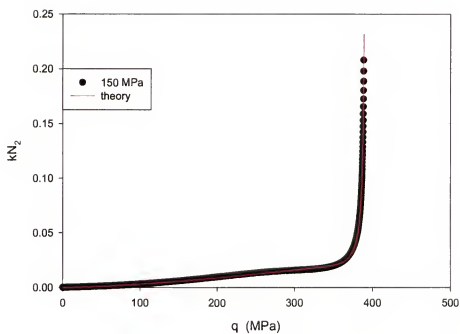


Figure 4-40: Experimental/theoretical comparison of  $kN_2$ ,  $\chi = 150$  MPa

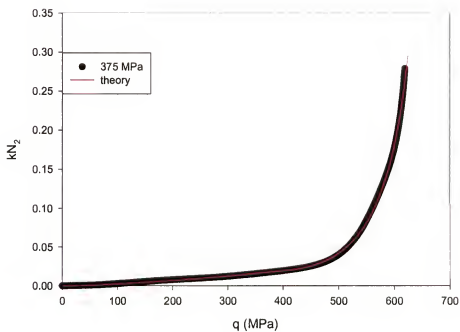


Figure 4-41: Experimental/theoretical comparison of  $kN_2$ ,  $\chi = 375$  MPa

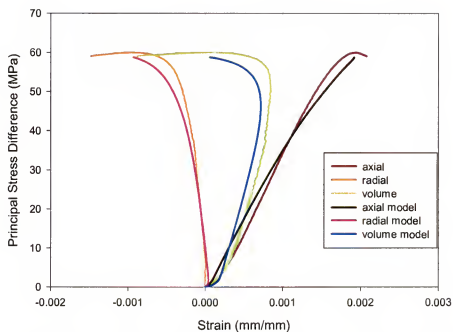


Figure 4-42: Experimental/theoretical comparison of uniaxial compression test

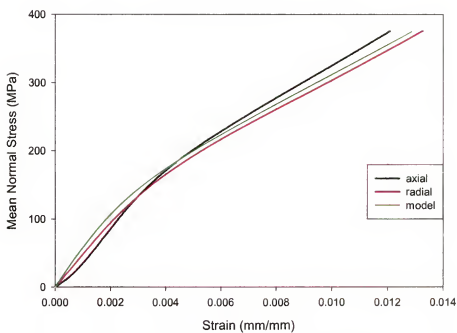


Figure 4-43: Experimental/theoretical comparison of 375 MPa hydrostatic compression test

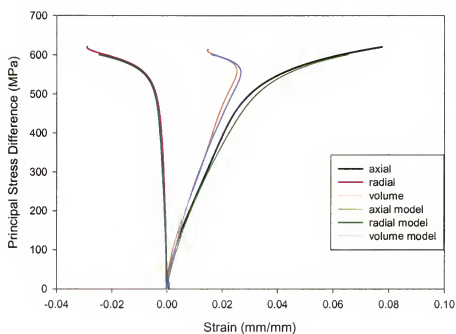


Figure 4-44: Experimental/theoretical comparison of 375 MPa deviatoric compression test

## CHAPTER 5 CONCLUSIONS

A database of mechanical response of mortar and concrete WES5000 was generated. The mortar studied contains masonry sand but no large aggregates. The mortar experimental effort consisted of a series of quasi-static and dynamic tests at several strain rates, under both unconfined and confined conditions. Confinement levels utilized were 1.72 MPa ,3.45 MPa , and 6.89 MPa. The quasi-static experiments were conducted at a strain rate of approximately  $10^{-6}/s$ . Same size mortar specimens were tested under both unconfined and confined conditions in the University of Florida 7.62 cm diameter split Hopkinson pressure bar (UFSHPB) at three different loading rates in the range 60/s to about 160/s. The range of strain rates was bound by the capacity of the UFSHPB gas gun firing chamber. The highest strain rates corresponded to a striker bar velocity of approximately 14 m/s obtained by use of the 0.762m striker bar and the chamber gun pressurized to 3.45 MPa. The lowest dynamic strain rates achieved corresponded to a chamber pressure of 1.39 MPa (striker velocity 7.75 m/s). Experiments at a mid-range velocity of 11 m/s, corresponded to 2.41 MPa firing pressure were also conducted. The data obtained in such tests are of fundamental interest since they allow the characterization of the combined effects of confining pressure and strain rate on the deformation and strength of the material. The confined dynamic tests showed similar stress-strain response as the quasi-static tests. Dilatancy has been observed at high levels of the principal stress difference for both dynamic and static conditions. The unconfined dynamic compressive strengths are approximately double that of the quasi-static compressive strengths.

Most of the specimens showed very little damage post test other than some chipping around the top edges, most likely due to localized tensile effects.

The concrete selected for this research, WES5000, was first formulated at the U.S. Army Corps of Engineer Research and Development Center Waterways Experiment Station (WES, hence WES500) as a standard test concrete for phenomenology studies. The mechanical response of WES5000 under a variety of loading conditions was investigated. Of particular interest was to establish the influence of pressure on strength, elastic properties, compressibility and dilatant behavior. A test matrix and test protocol for studying quasi-static triaxial compression behavior of WES5000 was proposed. A step-wise loading-creep-unload-reload procedure, which allowed accurate separation between elastic and viscous effects on the material behavior was followed.

Hydrostatic tests up to a pressure of 0.5 GPa allowed for the accurate determination of the dependence of the bulk modulus on pressure and the correct estimation the material's compaction properties when subjected to pressures in the range encountered in dynamic events. Under confined quasi-static conditions, the material exhibited hardening behavior up to failure. Both compressibility and dilatancy regimes of the volumetric behavior were observed, the dilatancy threshold being highly dependent on the level of confinement. For confining pressures above 50 MPa, transition from compressibility to dilatancy is apparent only close to failure. To quantify the influence of loading rate on the strength of WES5000, the dynamic strengths were normalized by the quasi-static strengths corresponding to the same level of confinement. The dynamic increase factor (DIF) was plotted as a function of the  $\log_{10}(\dot{\epsilon})$  (see Figure 3–63). It can be concluded that under unconfined conditions, WES5000 follow the same trends as mortar and those reported in the literature [40, 41, 42] for other cementitious materials. However, under confined conditions the DIF values for WES5000 are significantly lower. The WES5000

generally exhibited far more cracking under similar loading conditions than was observed in mortar. A new elastic/viscoplastic model that captures compressibility and dilatancy, as well as strain rate effects has been developed. As a general framework, the elastic-viscoplastic formulation of Cristescu was chosen due to its apparent capability to capture the behavior of interest and the fact that there are no a priori limitations or restrictions regarding the specific expressions of the yield function and viscoplastic potential. However, it was found that in order to capture the peculiarities of the volumetric response, namely the reduced dilatancy at very high pressure, the hypothesis of existence of a viscoplastic potential has to be abandoned. A new flow rule was proposed for WES5000. Comparison between the model predictions and data showed that the proposed model describes with very good accuracy the high-pressure behavior of concrete. An obvious recommendation for future work is the application of the model to describe high-velocity penetration into concrete.

## REFERENCES

- [1] J. A. Zukas, T. Nicholas, H. F. Swift, L. B. Greszczuk, and D. R. Curran. *Impact Dynamics*. Krieger Publishing, Malabar, FL, 1992.
- [2] J. S. Wilbeck. Classification of impact regimes. Technical Report SwRI Project 06-9304, South West Research Institute, San Antonio, TX, 1985.
- [3] D. R. Curran, L. Seaman, T. Cooper, and D. A. Shockey. Micromechanical model for comminution and granular flow of brittle material under high strain rate application to penetration of ceramic targets. *International Journal of Impact Engineering*, 13(1):53–83, 1993.
- [4] U. S. Lindholm. High strain rate testing. In R. F. Bunshah, editor, *Techniques in Metals Research*, volume 5. Interscience, New York, 1971.
- [5] T. von Kármán. Festigkeitsversuche unter allseitigem Druck. *Zeit Verein Deutscher Ing.*, 55:1749–1757, 1911.
- [6] J. Chinn and R. M. Zimmerman. Behavior of plain concrete under various high triaxial compression loading conditions. Technical Report WL-TR-64-163, Air Force Weapons Laboratory, August 1965.
- [7] N. D. Cristescu and U. Hunsche. *Time Effects in Rock Mechanics*. John Wiley & Sons, West Sussex, England, 1998.
- [8] N. Cristescu. *Rock Rheology*. Kluwer Academic Publishers, Dordrecht, The Netherlands, 1989.
- [9] O. Cazacu, J. Jin, and N. D. Cristescu. A new constitutive model for alumina powder compaction. *KONA*, 17(1), 1997.
- [10] D. J. Frew, J. D. Cargile, and J. Q. Ehrigott. Wes geodynamics and projectile penetration research facilities. In *Proceedings of the ASME Winter Annual Meeting*. ASME, 1993.
- [11] P. W. Bridgman. *Studies in Large Plastic Flow and Fracture*. McGraw-Hill Book Company, New York, 1952.
- [12] N. Cristescu. Nonassociated elastic/viscoplastic constitutive equations for sand. *International Journal of Plasticity*, 7:41–64, 1991.
- [13] B. Herring. The secrets of Roman concrete. *Constructor*, LXXXIV(9):13–16, September 2002.



- [14] D. Moore. *The Roman Pantheon: The Triumph of Concrete*. Office Outlet Publishing, Pinedale, WY, 1995.
- [15] A. M. Neville. *Properties of Concrete*. John Wiley & Sons, New York, 4 edition, 1996.
- [16] C. Wang and C. G. Salmon. *Reinforced Concrete Design*. Harper Collins, New York, 5 edition, 1992.
- [17] K. Mallory and A. Ottar. *The Architecture of War*. Pantheon Books, New York, 1973.
- [18] ASTM C 801-91. Standard test method for determining the mechanical properties of hardened concrete under triaxial loads. American Society For Testing & Materials, 1991.
- [19] J. D. Cargile. Development of a constitutive model for numerical simulation of projectile penetration into brittle geomaterials. Technical Report SL-99-11, US Army Corps of Engineers, Engineer Research and Development Center, Vicksburg MS, September 1999.
- [20] N. D. Cristescu and O. Cazacu. Experiments and modeling of virgin and damaged concrete and geomaterials. Technical Report AFRL-MN-EG-TR-2001-7108, US Air Force Research Laboratory, Munitions Directorate, Eglin AFB FL, October 2001.
- [21] B. Hopkinson. A method of measuring the pressure produced in the detonation of high explosives or by the impact of bullets. *Philosophical Transaction of the Royal Society of London: Series A*, 231:437–456, 1914.
- [22] E. D. Davies and S. C. Hunter. The dynamic compression testing of solids by the method of the split Hopkinson pressure bar. *Journal of the Mechanics and Physics of Solids*, 11:155–179, 1963.
- [23] J. E. Field, S. M. Walley, N. K. Bourne, and J. M. Huntley. Review of experimental techniques for high rate deformation studies. In *Proceedings of Acoustics and Vibration Asia*, pages 9–38, Singapore, 1998.
- [24] H. Kolsky. An investigation of the mechanical properties of materials at very high rates of loading. *Philosophical Transaction of the Royal Society of London: Series B*, 62:676–700, 1949.
- [25] C. A. Ross. Split-Hopkinson pressure bar tests. Technical Report ESL-TR-88-82, Air Force Engineering and Services Center, March 1989.
- [26] M. L. Hughes, J. W. Tedesco, and C. A. Ross. Numerical analysis of high strain rate splitting-tensile tests. *Computers & Structures*, 47(4/5):653–671, 1993.

- [27] J. W. Tedesco, C. A. Ross, and S. T. Kuennen. Experimental and numerical analysis of high strain rate splitting tensile tests. *ACI Materials Journal*, 90(2):162–169, March-April 1993.
- [28] C. A. Ross, S. T. Kuennen, and J. W. Tedesco. Experimental and numerical analysis of high strain-rate concrete tensile tests. In S. P. Shah, S. E. Swartz, and M. L. Wang, editors, *Micromechanics of Failure of Quasi-Brittle Materials*, pages 353–364. Elsevier Applied Science, London, 1990.
- [29] F. G. Díaz-Rubio, J. R. Pérez, and V. S. Gálvez. The spalling of long bars as a reliable method of measuring the dynamic tensile strength of ceramics. *International Journal of Impact Engineering*, 27:161–177, 2002.
- [30] J. Lankford, C. E. Anderson, Jr., A. J. Nagy, J. D. Walker, A. E. Nicholls, and R. A. Page. Inelastic response of confined aluminum oxide under dynamic loading conditions. *Journal of Materials Science*, 33(6):1619, March 1998.
- [31] J. D. Walker, A. Nagy, C. E. Anderson, Jr., J. Lankford, and A. E. Nicholls. Large confinement high strain rate test apparatus for ceramics. In L. E. Murr, K. P. Staudhammer, and M. A. Meyers, editors, *Metallurgical and Materials Applications of Shock-Wave and High-Strain-Rate Phenomena: Proceedings of the 1995 International Conference (EXPLOMET '95)*, pages 179–186. Elsevier Applied Science, 1995.
- [32] W. Chen and G. Ravichandran. An experimental technique for imposing dynamic multiaxial-compression with mechanical confinement. *Experimental Mechanics*, 36(2):155–158, June 1996.
- [33] B. Bhushan and W. E. Jahsman. Measurement of dynamic material behavior under nearly uniaxial strain conditions. *International Journal of Solids & Structures*, 14:739–753, 1978.
- [34] L. E. Malvern and D. A. Jenkins. Dynamic testing of laterally confined concrete. Technical Report ESL-TR-89-47, Air Force Engineering and Services Center, September 1990.
- [35] L. M. Barker and R. E. Hollenbach. Laser interferometer for measuring high velocities of any reflecting surface. *Journal of Applied Physics*, 42(11):4669–4675, 1972.
- [36] D. L. Grote, S. W. Park, and M. Zhou. Dynamic behavior of concrete at high strain rates and pressures: I. experimental characterization. *International Journal of Impact Engineering*, 25:869–886, 2001.
- [37] M. E. Kipp, D. E. Grady, and E. P. Chen. Strain rate dependent fracture initiation. *International Journal of Fracture*, 16:471–478, 1980.

- [38] G. T. Gray III. Classical split-Hopkinson pressure bar testing. In *ASM Handbook*, volume 8, Mechanical Testing and Evaluation, pages 462–473. American Society for Metals, 2000.
- [39] M. A. Kaiser. Advancements in the split hopkinson bar test. Master's thesis, Virginia Polytechnic Institute and State University, 1998.
- [40] C. A. Ross, D. M. Jerome, J. W. Tedesco, and M. L. Hughes. Moisture and strain rate effects on concrete. *ACI Materials Journal*, 93(3):293–300, May-June 1996.
- [41] L. E. Malvern, D. A. Jenkins, T. Tang, and C. A. Ross. Dynamic compressive testing of concrete. In *Proceedings of Second Symposium on the Interaction of Non-Nuclear Munitions with Structures*, pages 194–199, Panama City Beach, FL, April 1985.
- [42] M. J. Schmidt, O. Cazacu, C. A. Ross, and N. D. Cristescu. Dynamic behavior of mortar: experimental data and modeling. In *Proceedings of the 10th International Conference on Computer Methods and Advances in Geomechanics*, pages 271–276, Tucson, Arizona, January 2001.
- [43] L. E. Malvern, D. A. Jenkins, T. Tang, and S. McClure. Dynamic testing of laterally confined concrete. In S. P. Shah, S. E. Swartz, and M. L. Wang, editors, *Micromechanics of Failure of Quasi-Brittle Materials*. Elsevier Applied Science, 1990.
- [44] R. Courant. Variational methods for the solutions of problems of equilibrium and vibrations. *Bulletin of the American Mathematical Society*, 49:1–23, 1943.
- [45] M. J. Turner, R. W. Clough, H. C. Martin, and L. J. Topp. Stiffness and deflection analysis of complex structures. *Journal of Aeronautical Science*, 23:805–824, 1956.
- [46] R. W. Clough. The finite element method in plane stress analysis. In *2nd ASCE Conference on Electronic Computation*, Pittsburgh, Pa, September 1960.
- [47] D. Ngo and A. C. Scordelis. Finite element analysis of reinforced concrete beams. *Journal of the American Concrete Institute*, 64(3):152–163, March 1967.
- [48] W. F. Chen. *Plasticity in Reinforced Concrete*. McGraw-Hill, New York, 1982.
- [49] C. E. Anderson, Jr. An overview of the theory of hydrocodes. *International Journal of Impact Engineering*, 5:33–59, 1987.
- [50] T. Mori and K. Tanaka. Average stress in matrix and average elastic energy of materials with misfitting inclusions. *Acta Metallurgica*, 21:571–574, 1973.

- [51] S. Nemat-Nasser and M. Hori. *Micromechanics: Overall Properties of Heterogeneous Materials*. North-Holland, Amsterdam, 1993.
- [52] J. W. Ju and K. H. Tseng. A three-dimensional statistical micromechanical theory for brittle solids with interacting microcracks. *International Journal of Damage Mechanics*, 1:102–131, 1994.
- [53] Q. Xia. Numerical and experimental analysis of the dynamic behavior of concrete and mortar. Master's thesis, Georgia Institute of Technology, March 1998.
- [54] K. Thoma, W. Riedel, and S. Hiermaier. Mesomechanical modeling of concrete shock response experiments and linking to macromechanics by numerical analysis. In *Proceedings of ECCM-99, European Conference on Computational Mechanics*, Munich, Germany, 1999.
- [55] A. E. Green and P. M. Nagdhi. A dynamical theory of interacting continua. *International Journal of Engineering Science*, 3:231, 1965.
- [56] M. Ortiz. A constitutive theory for the inelastic behavior of concrete. *Mechanics of Materials*, 4:67–93, 1985.
- [57] G. N. Pande, G. Beer, and J. R. Williams. *Numerical Methods in Rock Mechanics*. John Wiley & Sons, West Sussex, England, 1990.
- [58] S. Hentz, L. Daudeville, and F. V. Donzé. Discrete element modelling of concrete and identification of the constitutive behaviour. In *Proceedings of the 15th ASCE Engineering Mechanics Conference*, New York, New York, June 2002.
- [59] F. Camborde, C. Mariotti, and F. V. Donzé. Numerical study of rock and concrete behaviour by discrete element modelling. *Computers and Geotechnics*, 27:225–247, 2000.
- [60] F. V. Donzé, S. A. Magnier, L. Daudeville, C. Mariotti, and L. Davenne. Study of the behavior of concrete at high strain rate compressions by a discrete element method. *ASCE Journal of Engineering Mechanics*, 125(10):1154–1163, 1999.
- [61] L. M. Kachanov. On the creep rupture time. *Izv. AN.SSSR, Otd. Tekhn. Nauk*, 8:26–31, 1958.
- [62] J. Lemaitre and J. L. Chaboche. Aspect phenomenologique de la rupture par endommagement. *J. de Mecanique Appliquee*, 2:317–365, 1978.
- [63] J. Lemaitre and J. L. Chaboche. Aspect phenomenologique de la rupture par endommagement. *J. de Mecanique Appliquee*, 2:317–365, 1978.

- [64] L. Davison and A. L. Stevens. Thermodynamic constitution of spalling elastic bodies. *J. Appl. Phys.*, 44:668–674, 1973.
- [65] D. Krajcinovic and G. U. Fonseka. The continuous damage theory of brittle materials. *J. Appl. Mech.*, 48:809–815, 1993.
- [66] R. Talreja. A continuum mechanics characterization of damage in composite materials. *Proc. R. Soc. London. A.*, 399:195–216, 1985.
- [67] A. A. Vakulenko and L. M. Kachanov. Continuum model of medium with cracks. *Mekhanika Tverdogo Tela*, 4:159–166, 1971.
- [68] A. Dragon and Z. Mroz. A continuum model for plastic brittle behavior of rock and concrete. *Int. J. Eng. Sci.*, 17:121–137, 1979.
- [69] M. Kachanov. Continuum model of medium with cracks. *J. Engng. Mech. Div.*, 106:1039–1051, 1980.
- [70] M. Kachanov. Effective elastic properties of cracked solids: critical reviews of some basic concepts. *Appl. Mech. Rev.*, 45:304–335, 1992.
- [71] J. P. Cordebois and F. Sidoroff. Endommagement anisotrope en elasticite et plasticite. *J. de Mecanique Theorique et Appliquee, Numero Special*, pages 45–60, 1982.
- [72] S. Murakami. Mechanical modeling of material damage. *J. Appl. Mech.*, 55:280–286, 1988.
- [73] S. Murakami and K. Kamiya. Constitutive and damage evolution equations of elastic-brittle materials based on irreversible thermodynamics. *Int. J. Mech. Sci.*, 4:473–486, 1997.
- [74] J. L. Chaboche. Le concept de contrainte effective applique a l'elasticite et a la viscoplasticite en presence d'un endommagement anisotrope. In J. P. Boehler, editor, *In Mechanical behavior of anisotropic solids, Proc. Euromech. Col. 115*, pages 737–760, The Netherlands, 1979. Martinus Nijhoff.
- [75] J. C. Simo and J. W. Ju. Strain and stress based continuum damage models-i. formulation. *Int. J. Solids. Structs.*, 821-840:821–840, 1987.
- [76] C. L. Chow and J. Wang. Ductile fracture characterization with an anisotropic continuum damage theory. *Engng. Fracture Mech.*, 30:547–563, 1988.
- [77] V. A. Lubarda and D. Krajcinovic. Damage tensor and crack density distribution. *Int. J. Solids. Structures*, 30:2859–2877, 1993.
- [78] D. Halm and A. Dragon. A model of anisotropic damage by mesocrack growth; unilateral effect. *Int. J. Damage Mech.*, 5:384–402, 1996.

- [79] L. M. Taylor, J. S. Kuszmaul, and E. P. Ghen. Damage accumulation due to microcracking in brittle rock under dynamic loading. In J. C. Cizek, editor, *In Response of geologic materials to blast loading and impact, ASCE/ASME Mechanics Conference*, pages 95–104, Albuquerque, NM, 1985.
- [80] D. E. Grady. The mechanics of fracture under high-rate stress loading. In Z. P. Bažant, editor, *In W. Prager Symposium on Mechanics of Geomaterials: Rocks, Concretes and Soils*, Albuquerque, NM, 1983.
- [81] D. A. Matuska, J. J. Osborn, and E. W. Piburn. *OTI-HULL Users Manual*. OTI, Shalimar FL, August 1991.
- [82] M. O. Faruque and C. J. Chang. A constitutive model for pressure sensitive materials with particular reference to plain concrete. *International Journal of Plasticity*, 6:29–43, 1990.
- [83] J. C. Simo, J.-W. Ju, K. S. Pister, and R. L. Taylor. Assessment of cap model: Consistent return algorithms and rate-dependent extension. *Journal of Engineering Mechanics*, 114(2):191–218, February 1988.
- [84] T. L. Warren, A. F. Fossum, and D. J. Frew. Penetration into low strength (23 MPa) concrete: Target characterization and simulations. *Mechanics of Materials*, to appear.
- [85] L. E. Schwer and Y. D. Murray. A three-invariant smooth cap model with mixed hardening. *International Journal for Numerical and Analytical Methods in Geomechanics*, 18:657–688, 1994.
- [86] E. C. Bingham. *Fluidity and Plasticity*. McGraw Hill, New York, 1922.
- [87] K. Hohenemser and W. Prager. *Z. Angew. Math. Mech.*, 12:215–226, 1932.
- [88] N. Cristescu and I. Suliciu. *Viscoplasticity*. Sijthoff & Noordhoff, The Netherlands, 1981.
- [89] L. E. Malvern. *Quart. Appl. Math.*, 8:405–411, 1951.
- [90] L. E. Malvern. *J. Appl. Mech.*, 18:203–208, 1951.
- [91] L. E. Malvern. The propagation of longitudinal waves of plastic deformation in a bar of material exhibiting a strain-rate effect. *Journal of Applied Mechanics*, pages 203–208, June 1951.
- [92] T. J. Holmquist, G. R. Johnson, and W. H. Cook. A computational constitutive model for concrete subjected to large strains, high strain rates, and high pressures. In *14th International Symposium on Ballistics*, September 1993.

- [93] G. R. Johnson and T. J. Holmquist. An improved computational constitutive model for brittle materials. In *High-Pressure Science and Technology – 1993: Proceedings of the Joint IARA/APS Conference*. AIP Press, 1994.
- [94] G. R. Johnson and T. J. Holmquist. A computational constitutive model for brittle materials subjected to large strains, high strain rates, and high pressures. In M. A. Meyers, et al., editor, *Shock Wave and High-Strain-Rate Phenomena in Materials*. Marcel Dekker, New York, 1992.
- [95] G. R. Johnson, R. A. Stryk, T. J. Holmquist, and S. R. Beissel. Numerical algorithms in a lagrangian hydrocode. Technical Report WL-TR-1997-7093, Wright Laboratory Armament Directorate, June 1997.
- [96] T. J. Holmquist, G. R. Johnson, D. E. Grady, C. M. Lopatin, and E. S. Hertel Jr. High strain rate properties and constitutive modeling of glass. In *15th International Symposium on Ballistics*, May 1995.
- [97] G. R. Johnson, S. R. Beissel, T. J. Holmquist, and D. J. Frew. Computed radial stresses in a concrete target penetrated by a steel projectile. In *Structures Under Shock and Impact*, Thessaloniki, Greece, June 1998.
- [98] P. Perzyna. Fundamental problems in viscoplasticity. *Advances in Applied Mechanics*, 9:243–377, 1966.
- [99] N. Cristescu. *Dynamic Plasticity*. North-Holland, Amsterdam, 1967.
- [100] D. Florea. Nonassociated elastic/viscoplastic model for bituminous concrete. *International Journal of Engineering Science*, 32(1):87–93, 1994.
- [101] D. Florea. Associated elastic/viscoplastic model for bituminous concrete. *International Journal of Engineering Science*, 32(1):79–86, 1994.
- [102] O. Cazacu. *Contribution à la modélisation elasto-viscoplastique d’un roche anisotrope*. PhD thesis, University of Science and Technology, Lille France, 1995.

## BIOGRAPHICAL SKETCH

Martin J. Schmidt was born on February 7 1960 in Oak Park Illinois, the son of a first generation American family. When he was four years old, his family moved to Aiken S.C. where he completed my secondary education, graduating from Aiken Senior High School in 1978. In May of 1983, he was graduated from Clemson University, Clemson, South Carolina with with the degree Bachelor of Science in Mechanical Engineering. While in college, he worked as a cooperative education student with the United States Department of Energy. Post graduation, he was employed by Daniel International from 1984 to 1985. He has been employed by the Air Force Research Laboratory since 1986. Martin Schmidt was graduated from the University of Florida with the degree of Master of Science in Mechanical Engineering in December of 1991. He was admitted as a doctoral candidate in the department of Mechanical and Aerospace Engineering in October of 1998.



I certify that I have read this study and that in my opinion it conforms to acceptable standards of scholarly presentation and is fully adequate, in scope and quality, as a dissertation for the degree of Doctor of Philosophy.



Nicolae Cristescu, Chair  
Graduate Research Professor of  
Mechanical and Aerospace Engineering

I certify that I have read this study and that in my opinion it conforms to acceptable standards of scholarly presentation and is fully adequate, in scope and quality, as a dissertation for the degree of Doctor of Philosophy.



Oana Cazacu, Cochair  
Assistant Professor of Mechanical and  
Aerospace Engineering

I certify that I have read this study and that in my opinion it conforms to acceptable standards of scholarly presentation and is fully adequate, in scope and quality, as a dissertation for the degree of Doctor of Philosophy.



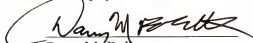
Edward K. Walsh  
Professor of Mechanical and Aerospace  
Engineering

I certify that I have read this study and that in my opinion it conforms to acceptable standards of scholarly presentation and is fully adequate, in scope and quality, as a dissertation for the degree of Doctor of Philosophy.




James E. Milton  
Professor Emeritus of Mechanical and  
Aerospace Engineering

I certify that I have read this study and that in my opinion it conforms to acceptable standards of scholarly presentation and is fully adequate, in scope and quality, as a dissertation for the degree of Doctor of Philosophy.



Davy M. Belk  
Assistant Professor of Mechanical and  
Aerospace Engineering

I certify that I have read this study and that in my opinion it conforms to acceptable standards of scholarly presentation and is fully adequate, in scope and quality, as a dissertation for the degree of Doctor of Philosophy.



Christopher S. Anderson, External  
Assistant Professor of Electrical and  
Computer Engineering

This dissertation was submitted to the Graduate Faculty of the College of Engineering and to the Graduate School and was accepted as partial fulfillment of the requirements for the of Doctor of Philosophy.

August 2003



Pramod P. Khargonekar  
Dean, College of Engineering

---

Winfred M. Phillips  
Dean, Graduate School